New Jersey Institute of Technology
Digital Commons @ NJIT

Theses | Electronic Theses and Dissertations

Spring 5-31-1997

Analysis and comparison of resistive, ferroelectric and pyroelectric uncooled bolometers for electronic imaging systems

Mo-Huang Li
New Jersey Institute of Technology

Follow this and additional works at: https://digitalcommons.njit.edu/theses

Part of the Electrical and Electronics Commons

Recommended Citation
Li, Mo-Huang, "Analysis and comparison of resistive, ferroelectric and pyroelectric uncooled bolometers for electronic imaging systems" (1997). *Theses*. 988.
https://digitalcommons.njit.edu/theses/988

This Thesis is brought to you for free and open access by the Electronic Theses and Dissertations at Digital Commons @ NJIT. It has been accepted for inclusion in Theses by an authorized administrator of Digital Commons @ NJIT. For more information, please contact digitalcommons@njit.edu.

Copyright Warning & Restrictions

The copyright law of the United States (Title 17, United States Code) governs the making of photocopies or other reproductions of copyrighted material.

Under certain conditions specified in the law, libraries and archives are authorized to furnish a photocopy or other reproduction. One of these specified conditions is that the photocopy or reproduction is not to be "used for any purpose other than private study, scholarship, or research." If a, user makes a request for, or later uses, a photocopy or reproduction for purposes in excess of "fair use" that user may be liable for copyright infringement,

This institution reserves the right to refuse to accept a copying order if, in its judgment, fulfillment of the order would involve violation of copyright law.

Please Note: The author retains the copyright while the New Jersey Institute of Technology reserves the right to distribute this thesis or dissertation

Printing note: If you do not wish to print this page, then select "Pages from: first page # to: last page #" on the print dialog screen

NJIT
New Jersey's Science & Technology University

The Van Houten library has removed some of the personal information and all signatures from the approval page and biographical sketches of theses and dissertations in order to protect the identity of NJIT graduates and faculty.

ABSTRACT

ANALYSIS AND COMPARISON OF RESISTIVE, FERROELECTRIC AND PYROELECTRIC UNCOOLED BOLOMETERS FOR ELECTRONIC IMAGING SYSTEMS

by
Mo-Huang Li

The performance parameters (responsivity (R_V), detectivity (D*), total noise and response time) of resistive, pyroelectric and ferroelectric bolometer detectors are dependent on a large number of key variables including chopping frequency, the input impedance and voltage noise of the readout circuitry, the structure dependent parameters (particularly thermal conductance and thermal capacitance), and material properties such as dielectric constant, pyroelectric coefficient, loss tangent and thin film thickness. The interrelationship between the key variables and their influence on performance is often complex and not easily discerned for the three major types of thermal detectors: resistive, pyroelectric and ferroelectric bolometers.

In this thesis research, the dependence of R_V , D* and total noise on these key parameters were analyzed and written as equations from which computer calculations could easily be made. The analyzed results were used to compare the performance of the three types of sensors for present-day structure and material characteristics and also for material characteristics and structures that might be developed in the future.

ANALYSIS AND COMPARISON OF RESISTIVE, FERROELECTRIC AND PYROELECTRIC UNCOOLED BOLOMETERS FOR ELECTRONIC IMAGING SYSTEMS

by
Mo-Huang Li

A Thesis
Submitted to the Faculty of
New Jersey Institute of Technology
in Partial Fulfilment of the Requirements for the Degree of
Master of Science in Electrical Engineering

Department of Electrical and Computer Engineering

May 1997

Blank Page

APPROVAL PAGE

ANALYSIS AND COMPARISON OF RESISTIVE, FERROELECTRIC AND PYROELECTRIC UNCOOLED BOLOMETERS FOR ELECTRONIC IMAGING SYSTEMS

by
Mo-Huang Li

Dr. Roy H. Cornely, Thesis Advisor — Date
Professor of Electrical and Computer Engineering, NJIT

Dr. Haim Grebel, Committee Member — Date
Professor of Electrical and Computer Engineering, NJIT

Dr. Constantine N. Manikopoulos, Committee Member — Date
Associate Professor of Electrical and Computer Engineering, NJIT

BIOGRAPHICAL SKETCH

Author: Mo-Huang Li

Degree: Master of Science

Date: May, 1997

Undergraduate and Graduate Eduaction:

- Master of Science in Electrical Engineering,
  New Jersey Institute of Technology, Newark, NJ, 1997

- Bachelor of Science in Electrical Engineering,
  National Sun Yet-sen University, Kaohsiung, Taiwan, 1991

Major: Electrical Engineering

Dedicated to my mom, my dad,
and my family

ACKNOWLEDGMENT

I would like to express my deepest appreciation to my advisor, Dr. Roy H. Cornely, for his guidance, constant support and encouragement throughout the two years of my Master studies. I am very happy to become one of his Master students.

Special thanks are given to Dr. Haim Grebel and Dr. Constantine N. Manikopoulos for actively participating in my committee. Also I am grateful to express my appreciation to Dr. William N. Carr for his useful courses on VLSI design and Microsensors and Microactuators which were very useful helpful in doing my research

TABLE OF CONTENTS

Chapter **Page**

1 INTRODUCTION.....1

1.1 Objectives and Organization of the Thesis.....1

1.2 Comparison of Potential Applications for Photon and Thermal Detector.....2

1.3 Basic Operational Principles of Uncooled (Thermal) Infrared Arrays.....6

2 INTRODUCTION TO FUNDATIONALS.....7

2.1 Thermal Radiation.....7

2.2..Noise.....9

2.2.1 Equivalent Noise Bandwidth.....10

2.2.2 Type of Noise.....12

2.3 Figures of Merit.....14

3 REVIEW OF THE THEORY AND PERFORMANCE OF RESISTIVE BOLOMETER UNCOOLED FOCAL PLANE ARRAYS.....20

3.1 Heat Balance Equations.....20

3.2 The Thermal Isolation Structure for a Bolometer Focal Plane Arrays.....26

3.3 The Readout Integrated Circuit (ROIC).....33

3.4 The Bolometer Material.....48

3.5 Monolithic Resistive Bolometer Arrays Developed by Honeywell.....53

3.6 Monolithic Resistive Bolometer Arrays Developed by Defense Science and Technology Organization.....57

4 REVIEW OF THE THEORY AND PERFORMANCE OF PYROELECTRIC AND FERROELECTRIC UNCOOLED FOCAL PLANE ARRAYS.....59

TABLE OF CONTENTS
(Continued)

Chapter Page

4.1 Pyroelectric Response.....59

4.2 Hybrid and Monolithic Thermal Structures.....64

4.3 Low Noise Readout Design and Circuitry.....67

4.4 Pyroelectric Materials.....76

4.5 Hybrid Ferroelectric Arrays Developed by Texas Instruments.....82

4.6 Hybrid Pyroelectric Arrays Developed in United Kingdom.....90

4.7 Monolithic Thin Film Pyroelectric Arrays Developed at University of Minnesota.....92

5 REVIEW OF THE THEORY AND PERFORMANCE OF THERMOELECTRIC UNCOOLED FOCAL PLANE ARRAYS.....97

5.1 Seeback Effect.....97

5.2 Materials.....101

5.3 Thermopile Arrays.....101

5.3.1 Thermopile Array Developed by University of Michigan.....105

5.3.2 Thermopile Array Developed by Honeywell.....107

5.3.3 Thermopile Array Developed by Japan Defense Agency.....107

6 THE PERFORMANCE OF BOLOMETER, PYROELECTRIC AND FERROELECTRIC DETECTORS.....109

6.1 The Performance of Bolometer Detector.....109

6.2 The Performance of Pyroelectric and Ferroelectric Detectors.....119

TABLE OF CONTENTS
(Continued)

Chapter **Page**

6.3 Comparison of the Future Performance of Bolometer, Pyroelectric and Ferroelectric Detectors........144

6.4 Future Directions........147

APPENDIX A TEMPERATURE FLUCTUATION NOISE........148

APPENDIX B *NETD* FOR TEMPERATURE FLUCTUATION NOISE AND BACKGROUND FLUCTUATION NOISE LIMITED........152

REFERENCES........155

LIST OF TABLES

Table — Page

1.1 Comparison of IR imagers....4

1.2 Generic Staring-FPA Parameters....5

2.1 Figures of Merit used to describe the performance of a detector....18

3.1 Properties and detectivity measured for semiconductor film bolometers operating in a vacuum....53

3.2 A summary of the parameters of Honeywell's microbolometer arrays....56

3.3 Expected performance and characteristics of a 256*256 sensor array....58

4.1A Properties and figure of merits of normal materials for imaging applications....79

4.1B Acronyms and Chemical Formulas....80

4.2 Phase transition materials $(T \cong T_t)$....81

4.3 Material parameters of sol-gel thin films prepared at University of Minnesota....95

4.4 Smmary of measured pyroelectric integrated detector performance....96

6.1 Detector and material properties for a bolometer detector....111

6.2 Detector and Material properties for pyroelectric and ferroelectric detectors....121

LIST OF FIGURES

Figure | Page

1.1 An illustration of the increasing size of detector arrays with time ... 5

2.1 Plank's spectral radiant emission versus wavelength ... 8

2.2 Atmospheric transmittance over a 1km path length ... 9

2.3 Definition of Target Modulation ... 17

2.4 Modulation transfer function ... 18

3.1 A dc voltage bias bolometer detector circuit ... 20

3.2 Constant dc current bias circuit ... 25

3.3 Schematic diagram of a microbridge thermal structure ... 27

3.4 The Honeywell's microbolometer cell and FPA ... 29

3.5 A sandwich-gap type microbridge structure designed by DSTO ... 30

3.6 Infrared absorption structure for thin film detectors ... 31

3.7 Measured (solid lines) and modeled (dashed lines) performance of an a-Si bolometerdeveloped by DSTO ... 32

3.8 Noise equivalent circuit of Fig. 3.1 ... 33

3.9 The equivalent circuit of Fig. 3.8 ... 35

3.10 A noise model of amplifiers ... 38

3.11 Noise voltage and current for typical low-noise BJTs, JFETs, and MOSFETs ... 40

3.12 Guide for selection of input stage ... 40

3.13 Numerical calculations of noise voltage and normalized detectivity ... 44

3.14 TCR vs VO_x resistivity for vanadium oxide thin film developed by Honeywell ... 49

TABLE OF FIGURES
(Continued)

Figure		Page
3.15	Activation energy analysis for a 500 Angstrom VO_x film of Honeywell	49
3.16	Electrical properties of VO_2 films deposited on Corning 7059 glass	50
3.17	Noise spectra of a-Si:H produced by (a) PECVD and (b) sputter deposition, plus the base Johnson noise. Developed by DSTO	52
3.18	The chopperless operation concept provides a 2* $NETD$ improvement	54
3.19	The block diagram of Honeywell's uncooled IR imager	55
4.1	Schematic diagram of a pyroelectric element subject to a small temperature change	60
4.2	Equivalent circuit of a pyroelectric element	60
4.3	Frequency variation of voltage responsivity	63
4.4	The ferroelectric hybrid array and its use in an IR sensor head	65
4.5	Low thermal conductance structure for a hybrid array element	65
4.6	A pyroelectric detector circuit	67
4.7	The noise equivalent circuit of Fig. 4.6	68
4.8	Equivalent noise voltage of Fig. 4.7	68
4.9	Noise sources for a $(BaSr)TiO_3$ ferroelectric element and their frequency dependence	74
4.10	Chopped radiation and detector element temperature	75
4.11	Field image difference processing digital filter	76
4.12	Operating modes for ferroelectric materials as infrared detectors	77

TABLE OF FIGURES
(Continued)

Figure **Page**

4.13 Polarization and permittivity as a function of temperature....83

4.14 Dielectric constant and Loss tangent for BST....84

4.15 Figure of merits F_V and F_D for BST....85

4.16 Schematic view of detector pixel structure....86

4.17 Photograph of uncooled focal plane array, showing the BST peeled back from the ROIC....86

4.18 Schematic diagram of the ROIC pixel unit cell....88

4.19 Readout IC array implementation of the unit cells....88

4.20 UFPA system functional block diagram....89

4.21 The pixel circuit and line filter designed by the terms in UK....92

4.22 Basic micromachined device structure with thermal isolation bridge, pyroelectric thin film, and preamplifier cell....93

4.23 Basic process flow for vertically-integrated pyroelectric detectors....94

5.1 The Seeback effect....97

5.2 Schematic of a cantilever beam structure thermopile.... 98

5.3 Measured Seeback coefficient vs. volume resistivity at T=300K....103

5.4 Measured Seeback coefficient vs. temperature for polysilicon....103

5.5 Effects of temperature and dopant concentrations on the Fermi energy of semiconductor material....104

5.6 Pixel structure....106

TABLE OF FIGURES
(Continued)

Figure		Page
5.7	Thermoelectric pixel structure	107
6.1	Calculated noise voltage and D^*, $R_m = R_L = 1M\Omega$	112
6.2	The noise voltages and D^* vs. thermal conductance at a chopping frequency of 60 Hz with $R_m = R_L = 1M\Omega$ and $C_{th} = 2*10^{-9}(J/^0K)$	114
6.3	D^* vs. thermal conductance at chopping frequencies of 30, 60, 120 and 240Hz, with $R_m = R_L = 1M\Omega$ and $C_{th} = 2*10^{-9}(J/^0K)$	115
6.4	Total noise voltage and D^* for $K_{th} = 2*10^{-7}$ W/K and $K_{th} = 2*10^{-6}$ W/K, with $C_{th} = 2*10^{-9}(J/^0K)$ and $R_m = R_L = 1M\Omega$	116
6.5	Calculated noise voltages and D^* when pulse bias was used and $R_m = R_L = 10K\Omega$	117
6.6	E_n and I_n of a 2N4250 transistor with different collector currents	118
6.7	Total noise voltage, R_V and D^* of a pyroelectric detector with bias resistance $R_L = 10^9\Omega$, $10^{10}\Omega$ and $10^{11}\Omega$	125
6.8	Total noise voltage, R_V and D^* for a ferroelectric detector with bias resistance $R_L = 10^9\Omega$, $10^{10}\Omega$ and $10^{11}\Omega$	126
6.9	Total noise voltage, Johnson noise and dielectric loss noise for a pyroelectric detector with bias resistance $R_L = 10^9\Omega$, $10^{10}\Omega$ and $10^{11}\Omega$	127
6.10	Total noise voltage, Johnson noise and dielectric loss noise for a ferroelectric detector with bias resistance $R_L = 10^9\Omega$, $10^{10}\Omega$ and $10^{11}\Omega$	128
6.11	Calculated noise voltages and D^* for a pyroelectric detector with $R_L = 10^{11}\Omega$ and $\tan\delta = 2*10^{-2}$	130
6.12	Calculated noise voltages and D^* for a ferroelectric detector with $R_L = 10^{11}\Omega$ and $\tan\delta = 2*10^{-3}$	131

TABLE OF FIGURES
(Continued)

Figure **Page**

6.13 Calculated noise voltages and D^* for a pyroelectric detector with $R_L = 10^{11}\Omega$ and $\tan\delta = 2*10^{-3}$ 132

6.14 Calculated noise voltages and D^* for a ferroelectric detector with $R_L = 10^{11}\Omega$, $Z_a = 7.59*10^{-8}(V)$ and $\tan\delta = 1*10^{-3}$ 133

6.15 The total noise and D^* vs. thermal conductance for a pyroelectric detector at a frequency of 60Hz with $R_L = 10^{11}\Omega$ and $\tan\delta = 2*10^{-3}$ 135

6.16 Total noise voltage and D^* vs. thermal conductance for a ferroelectric detector at a frequency of 60Hz with $R_L = 10^{11}\Omega$, $Z_a = 7.59*10^{-8}(V)$ and $\tan\delta = 1*10^{-3}$ 136

6.17 The D^* vs. thermal conductance for both detectors at frequencies 30, 60 and 120Hz 137

6.18 D^* vs. thin film thickness for a pyroelectric and ferroelecric detectors at a chopping frequency 60 Hz with $R_L = 10^9\Omega$, $10^{10}\Omega$ and $10^{11}\Omega$ 139

6.19 D^* vs. dielectric constant for a pyroelectric and ferroelecric detectors at a chopping frequency 60 Hz 142

6.20 The noise voltages and D^* vs. pyroelectric coefficient for a pyroelectric detector at a chopping frequency 60 Hz with $R_L = 10^{11}\Omega$ and $\tan\delta = 2*10^{-3}$ ...143

6.21 The noise voltages and D^* vs. pyroelectric coefficient for a ferroelectric detector at a chopping frequency 60 Hz with $R_L = 10^{11}\Omega$, $Z_a = 7.59*10^{-8}(V)$ and $\tan\delta = 1*10^{-3}$ 144

6.22 Comparison of the D^* and total noise voltages for bolometer, pyroelectric and ferroelectric detectors 146

CHAPTER 1

INTRODUCTION

1.1 Objectives and Organization of the Thesis

The objectives of this thesis were

a) To review and compare the different uncooled infrared technologies, their strengths and weaknesses.

b) To present the technologies in a concise tutorial manner for further development.

c) To understand and explain the demands that each material and device approach puts on the electronic circuitry that must interface the detected signals with the electronic and systems that will use the information.

d) To understand the potential performance of the technologies in the future. The performance of detectors are analyzed based on the theoretical equations, derived in the previous chapters and ultimate performance based on reasonable but speculative expectation of improvements in ferroelectric and pyroelectric materials. This thesis is aimed at offering an incentive for searching for materials and/or fabrication technologies.

The thesis is organized as follows.

Chapter 2 introduces the fundamentals of infrared systems-thermal radiation theory, noise sources and the several figures of merit used for characterization of the performance of uncooled infrared detectors.

Chapter 3 reviews the recent developments of resistive bolometer focal plane arrays. The basic equations for describing the responsivity are derived. The required

material properties and thermally isolated structures for high performance are described. The resistive bolometer focal plane arrays developed by Honeywell and DSTO (Defense Science and Technology Organization of Australia) are reviewed.

Chapter 4 reviews the developments of pyroelectric and ferroelectric focal plane arrays. The equations for describing the responsivity are derived. The various pyroelectric and ferroelectric materials developed for infrared detectors are also reported. The pyroelectric and ferroelectric FPAs developed by Texas Instruments, United Kingdom and University of Minnesota are reviewed.

Chapter 5 reviews the development of thermoelectric array. The equations for describing the responsivity are derived. The developed materials for thermoelectric infrared detectors are reported. The thermopile arrays developed by University of Michigan, Honeywell and Japan Defense Agency are reviewed.

Chapter 6 analyzes the performance of the detectors based on the theoretical equations, derived in the previous chapters. The three different types of infrared detectors are compared and the potential performance of the uncooled infrared technologies in the future are discussed.

1.2 Comparison of Potential Applications for Photon and Thermal Detectors

Two fundamental types of infrared detectors available today are photon detectors and thermal detectors. In photon detectors, the radiation is absorbed by the material, resulting in a direct modification of its electrical properties. Because the photon detectors are based on bandgap carrier generation, their responsivities are strongly dependent on wavelength. To suppress thermal excitation of free carriers due to the ambient temperature, photon

detectors are often cooled to temperatures well below 300K. In thermal detectors, the radiation is absorbed by the material, generating phonons and causing heating of the lattice. This change in the lattice temperature is then converted into a change in the electrical properties of the structure. In contrast to photon detectors, the responsivity of thermal detectors is independent of wavelength. Thermal detectors do not require cooling to exhibit adequate sensitivity. The trade-off, however, is that their photoresponse is relatively slow compared with that of most photon detectors, which have a response of microsecond or less at their operating temperature. The response time of thermal detectors is the inverse of the rate at which they lose heat to their surroundings. Thus, the response time of thermal detectors is the ratio of their heat capacity to the thermal conductance of their total heat loss mechanism. Typical response times of sensitive thermal detectors are milliseconds or more. The responsivities of present-day thermal detectors ($D^* \sim 10^9 cm.Hz^{1/2} / W$) are considerably lower than photon detectors ($D^* \sim 10^{12} cm.Hz^{1/2} / W$ for HgCdTe, 8-14um at temperature 77K) and the response times of thermal detectors are considerably slower than photon detectors; however, in applications where high sensivities and high speed are not of primary important, thermal detectors have a number of advantages including broad spectral response, low cost, ease of operating and insensitivity to ambient temperature. A comparison of IR imagers made of photon and thermal IR sensors is given in Table 1.1[1]. Present-day IR imagers use cryogenic coolers, complex IR optics, and expensive IR sensors materials. Typical cost of around $100,000 restrict their application to military. The thermal (uncooled) IR imagers without cryogenic cooling, complex IR optics and made with a micromachining process make the uncooled focal plane array inexpensive to produce. The successful development

of uncooled IR imaging system means that IR imagers no longer need to be restricted by cost to high-value military applications. Low-cost IR imaging systems will also become available for commercial applications.

Table 1.1 Comparison of IR imagers

Comparison Of IR imagers			
Feature	Cryogenic scanned imagers	Cryogenic staring imagers	Uncooled silicon microbolometer imagers
Approximate system cost	$100,000 (military-volume production)	$100,000 (military-volume production)	$1000 (high-volume production)
Typical focal plane temperature	100K	100K	Room temperature
IR sensor material	HgCdTe, InSb	HgCdTe, InSb, PtSi, GaAs/AlGaAs	Micromachined silicon
Typical NEDT	$0.1^0 C$	$0.01^0 C$	$0.05^0 C$
Applications	Military and specialized industrial applications	Military and specialized industrial applications	Widespread applications for military, commerce, research, industry, etc

*NETD: Noise Equivalent Temperature Difference

The chronological development of various FPA technologies is compared in Fig. 1.1. The basic parameters associated with today's solid-state FPAs are shown in Table 1.2. From Fig. 1.1 and Table 1.2, it can be seen that uncooled infrared focal plane arrays are potential technologies for long wavelength infrared applications. Because long-wavelength HgCdTe and IrSi FPAs must operate at very low temperature to minimize dark current, and extreme purity of materials and accuracy of process control are needed for acceptable levels of FPA yield and uniformity, the manufacturing cost for these technologies is much greater than for thermal detectors.

Some reported applications using uncooled infrared array are driver's aid [4,5], air conditioners [6,7], contactless temperature measure [8-10], surveillance [11-14] and military [15-17].

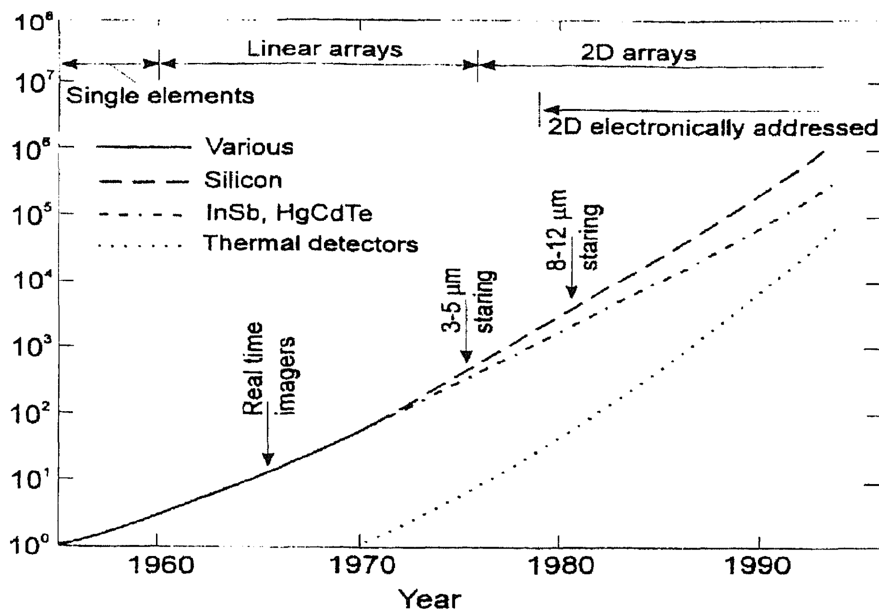

Fig. 1.1 An illustration of the increasing size of detector arrays with time. The line labelled silicon refers to both Schottky barriers and extrinsic silicon. The line labelled InSb and HgCdTe refers to both monolithic and hybrid technologies. The line labelled thermal detectors refers to both pyroelectric and bolometer detectors. (From [2])

Table 1.2 Generic Staring-FPA Parameters (From [3])

Spectral band	Detector Type	FPA Type	Typical FPA Sizes	Pixel Sizes (um)	Temporal Noise Floor (rms-Elect/Pix)	Non-uniformity (%)	Operating Temp. (K)
UV	Si	CCD	400*400	10 to 30	1 to 5	1	260 to 300
Visible	Si	CCD (Single)	488*640 2000*2000	10 to 30	1 to 5	1	260 to 300
		CCD (Buttable)	400*400	10 to 30	1 to 5	1	260 to 300
MWIR (3-5um)	InSb	Hybrid	256*256	40 to 60	80 to 500	4	55 to 80
	HgCdTe	Hybrid	256*256	40 to 60	100 to 1,000	5	60 to 120
	PtSi	Hybrid	512*512	20 to 40	80 to 500	2	55 to 80
	PtSi	CCD (Single)	488*640 400*400	20 to 40	20 to 100	0.25	55 to 80
		CCD (Buttable)	400*400	20 to 40	20 to 100	0.25	55 to 80
LWIR (8-12um)	HgCdTe	Hybrid	256*256	40 to 60	300 to 3,000	20	40 to 80
	IrSi,GeSi-Heteroj'n	CCD (Single)	244*320 400*400	20 to 40	20 to 100	1	30 to 60
		CCD (Buttable)	400*400	20 to 40	20 to 100	1	30 to 60
	Bol, BST	Monolithic, Hybrid	245*328 240*336	50	30,000	20	300

1.3 Basic Operational Principles of Uncooled (Thermal) Infrared Arrays

The uncooled infrared array technology approaches include: the resistive bolometer (temperature coefficient of resistance), the pyroelectric and ferroelectric detectors (temperature coefficient of dielectric constant) and the thermocouple (Seeback effect).

Resistive bolometers are temperature sensitive resistors, made from either a metal, semiconductor or superconductor, where they operate at the normal-to-superconducting transition edge.

Pyroelectric detectors exhibit a polarization which depends on the time rate of change of the detector temperature. Thus, they can be used as temperature dependent capacitors. Ferroelectric detectors are similar to pyroelectric detectors, but an electric field applied across their capacitor structures to enhance the output signal. Because pyroelectric detectors and ferroelectric detectors response to the time rate of change of their temperature, they require the incident radiation to be temporally modulated or "chopped".

Thermoelectric detectors are junctions of dissimilar materials which exhibit the Seeback effect. They are radiation-sensitive thermocouples. When several junctions are connected in series to enhance the signal voltage, the device is termed a "thermopile". Thermoelectric detectors do not require an electrical bias.

CHAPTER 2

INTRODUCTION TO FUNDATIONALS

2.1 Thermal Radiation

A blackbody thermal object generates thermal electromagnetic radiation according to Planck's law[18]:

$$P(\lambda,T)=\frac{2\pi hc^2}{\lambda^5(e^{hc/\lambda k_B T}-1)} \qquad (Watts/cm^2.um) \tag{2.1}$$

where

$P(\lambda,T)$: Planck's law for radiant exitance from a blackbody emitter,

λ: emitted wavelength in micrometers (um),

T: absolute temperature of the blackbody in Kelvins (Deg K),

h: Planck's constant,

c: speed of light,

k_B: Boltzmann's constant.

Fig. 2.1 shows the spectral radiant emission verse wavelength for several temperatures. The total emission in all wavelengths can be obtained by integrating Eq. 2.1 over all wavelengths.

$$P(T)=\int_0^\infty P(\lambda,T)d\lambda=\frac{2\pi^5 k_B^4 T^4}{15h^3c^2}=\sigma T^4 \tag{2.2}$$

where σ =Stefan-Boltzmann's constant $(5.67 * 10^{-12}\ Watts/cm^2.K^4)$.

Eq. 2.2, the Stefan-Boltzmann law, indicates that at room temperature(~300K), a $1cm^2$ blackbody emits about $50mW$ over all wavelengths. However, nearly all the radiation wavelengths are in the infrared range (0.7um to 1mm); therefore, the thermal

emission of room-temperature objects can only be imaged by using infrared detection equipment.

Wien's displacement law gives a relation between temperature and the wavelength peak of the Planck function. This relation is obtained by setting the wavelength derivative of Eq. 2.1 to zero,

$$\frac{\partial P(\lambda,T)}{\partial \lambda}=0 \tag{2.3}$$

and solving for the value of λT which maximizes $P(\lambda,T)$

$$\lambda_{max}T = 2898 \ \ (um.K) \tag{2.4}$$

Therefore, at room temperature (~300K), the wavelength peak of the Planck function is about 9.66um.

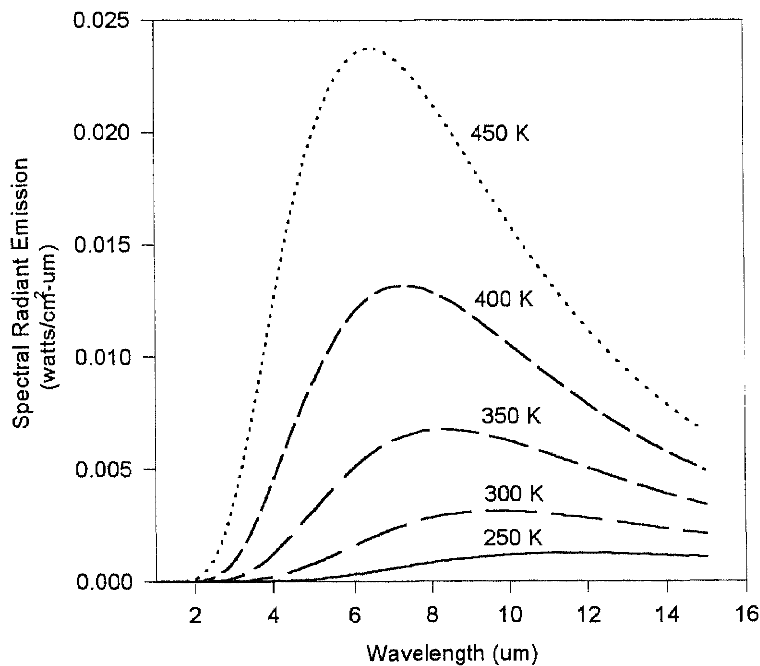

Fig. 2.1 Plank's spectral radiant emission versus wavelength.

Fig. 2.2 shows a transmittance spectra of atmosphere. The transmittance spectra of atmosphere depends strongly on the atmospheric constituents and environmental conditions. This figure shows the atmosphere has two windows between 3-5um and 8-14um. So, conventional IR imaging systems are designed to work within these two windows. For uncooled IR imaging systems, the wavelength region of choice is 8 to 12um, where room-temperature objects have their peak emission and the atmosphere has good transmission.

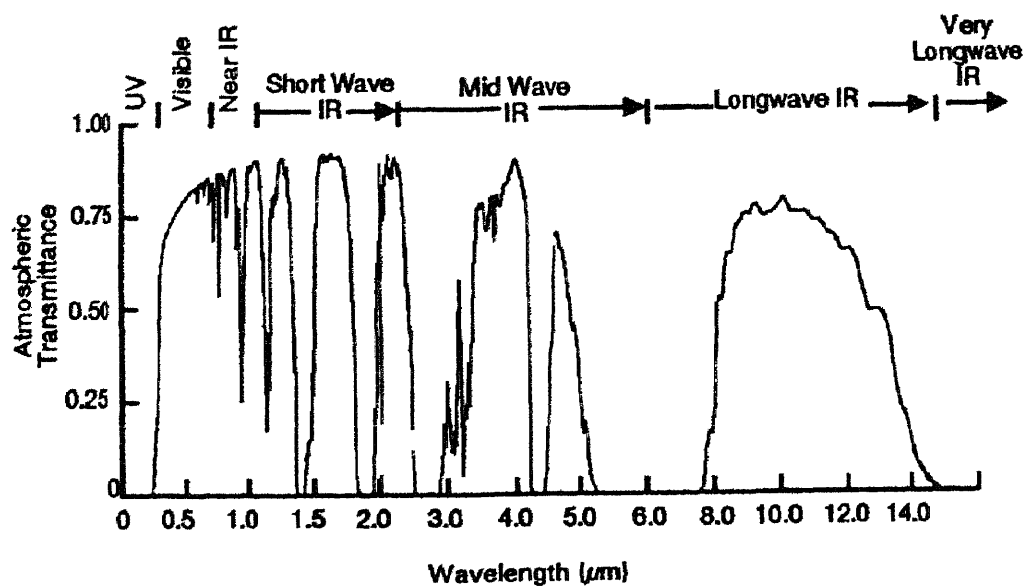

Fig. 2.2 Atmospheric transmittance over a 1km path length. (From [19])

2.2 Noise

Noise is a random variation or spontaneous fluctuation that results from the physics of devices and materials. If two or more independent noise sources are present in a circuit, their net effect is found by adding their mean-square values. Since mean-square values are proportional to power, this is equivalent to stating that noise powers are additive but not noise voltages or currents. Hence, the total noise V_{rms} from m sources is

$$V_{rms} = \left[\sum_{n=1}^{m} V_n^2 \right]^{1/2} \tag{2.5}$$

2.2.1 Equivalent Noise Bandwidth[20]

Noise bandwidth is not the same as the commonly used -3dB bandwidth. There is one definition of bandwidth for signals and another for noise. The bandwidth of an amplifier is classically defined as the frequency span between half-power points, the points on the frequency axis where the signal transmission has been reduced by 3dB from the central or midrange reference value. The noise bandwidth, Δf, is the frequency span of a rectangularly shaped power gain curve equal in area to the area of the actual power gain versus frequency curve. Noise bandwidth is the area under the power curve, the integral of power gain versus frequency, divided by the peak amplitude of the curve. This can be stated in equation form as

$$\Delta f = \frac{1}{G_0} \int_0^\infty G(f)df \tag{2.6}$$

where $G(f)$ is the power gain as a function of frequency and G_0 is the peak power gain. Since the power gain is proportional to the voltage gain squared, the equivalent noise bandwidth can also be written as

$$\Delta f = \frac{1}{A_{vo}^2} \int_0^\infty |A_v(f)|^2 df \tag{2.7}$$

where A_{vo} is the peak magnitude of the voltage gain and $|A_v(f)|^2$ is the square of the magnitude of the voltage gain over frequency.

Consider an example of a first-order low-pass filter whose signal transmission varies with frequency according to

$$A_v(f) = \frac{1}{1+\frac{jf}{f_2}} \tag{2.8}$$

where f_2 is the conventional -3dB cutoff frequency and the low-frequency and midband voltage gain has been normalized to unity. The noise bandwidth, Δf, calculated using Eq. 2.7 would be

$$\Delta f = 1.571 f_2 \tag{2.9}$$

The noise bandwidth is 57% larger than the conventional -3dB bandwidth for the first-order low-pass filter.

The term spectral density is used to describe the noise content in a $1\,Hz$ unit of bandwidth. It has units of $Volts^2$ per hertz and generally varies with frequency. If the spectral density of a noise source is not a frequency function, then it is called white-noise. The thermal (Johnson) noise is an example; its spectral density is

$$\frac{4k_B T R_d \Delta f}{\Delta f} = 4k_B T R_d \quad (V^2 / Hz) \tag{2.10}$$

Spectral density is a narrow band noise and generally varies with frequency. In order to obtain the total wide band noise, the spectral density function must be integrated over the frequency band of interest. Because the total noise is dependent on the measured system, the noise voltage and noise current are often expressed by their root spectral density with the units of $V / Hz^{1/2}$ and $A / Hz^{1/2}$.

2.2.2 Type of Noise

The various types of noise associated with IR thermal detectors are

1. Johnson noise or thermal noise:

This noise is caused by the random thermal motion of the charge carriers in a conductor. In every conductor or resistor at a temperature above absolute zero, the electrons are in random motion, and their motion is dependent on temperature. Since each electron carries a charge of $1.602 * 10^{-19} C$, there are many little current surges as electrons randomly move about in the material. Although the average current in the conductor resulting from these movements is zero, instantaneously there is a current fluctuation that gives rise to a voltage across the terminals of the detectors. The Johnson noise voltage V_j is

$$V_j = (4k_B T R_d \Delta f)^{1/2} \quad (V) \tag{2.11}$$

where

V_j: rms value of Johnson noise voltage,

k_B: Boltzmann's constant,

T: absolute temperature of the detector,

R_d: electrical resistance of the detector,

Δf : the equivalent noise bandwidth of a measuring system.

2. 1/f power law noise:

The cause for this noise is still not well known, but is often attributed to trapping of charge at surface states. The empirical expression for the noise voltage is

$$V_{1/f} = const.\frac{I^b R_d}{f^\beta} \quad (V / Hz^{1/2}) \tag{2.12}$$

where

b: a coefficient whose value is about one(b~1),

β: a coefficient whose value is about one-half(β~1/2),

I : the current through the pixel,

R_d : electrical resistance,

f : frequency.

1/f power law noise is difficult to understand theoretically because the parameters b and β are very much dependent upon material preparation and processing including contacts and surfaces.

3. Temperature fluctuation noise and background fluctuation noise:

A thermal detector in contact with its environment by conduction and radiation exhibits random fluctuations in temperature, known as temperature noise, because of the statistical nature of the heat interchange with its surroundings. The temperature fluctuation noise is the temperature fluctuation within the pixel(detector element) caused by conductive exchange between the pixel and background or substrate; the background fluctuation noise is the temperature noise within the pixel caused by radiative exchange between the pixel and background or substrate. The mean square power fluctuations, $\overline{W(t)^2}$, is given by (see Appendix A for details)

$$\overline{W(t)^2} = 4k_B K_{th} T^2 \Delta f \tag{2.13}$$

4. Fixed pattern noise:

The responsivity variations of detectors at a staring array produce fixed pattern noise. Because of the variations of the material properties and preamplifier circuits at pixels, each detector/preamplifier combination will have a different gain and level offset. These variations produce fixed pattern noise (FPN). If large deviations in responsivity exist, the image may be unrecognizable. As a result, a electronic gain/level normalization or nonuniformity correction (NUC) is required.

2.3 Figures of Merit[24]

Several figures of merit are employed to characterize the performance of infrared focal plane arrays: responsivity; D^* (pronounced "dee-star"); response time; noise equivalent power; noise equivalent temperature difference ($NETD$) and modulation transfer function (MTF). They are as follows:

Responsivity:

The pixel output signal per Watt of incident radiant power falling on the pixel, expressed as volts/Watt. Table 2.1 defines all the parameters in the following equations.

$$R_V(T,f) = \frac{V_S}{\Phi A_{pixel}} = \frac{V_N D^*}{(A_{pixel}\Delta f)^{1/2}} \quad (V / Watt) \tag{2.14}$$

If V_N is expressed in spectral density in units of $V / Hz^{1/2}$, then

$$R_V(T,f) = \frac{V_S}{\Phi A_{pixel}} = \frac{V_N D^*}{A_{pixel}^{1/2}} \quad (V / Watt) \tag{2.14.a}$$

Specific detectivity D^*:

The pixel output signal-to-noise ratio per Watt of incident radiant power falling on the pixel, measure in a 1Hz bandwidth. The units are $cm.Hz^{1/2} / Watt$.

$$D^*(T,f) = \frac{(A_{pixel}\Delta f)^{1/2}}{NEP} = \frac{(A_{pixel}\Delta f)^{1/2} R_V(T,f)}{V_N} \quad (cm.Hz^{1/2} / Watt) \quad (2.15)$$

If V_N is expressed in spectral density units of $V / Hz^{1/2}$, then

$$D^*(T,f) = \frac{(A_{pixel}\Delta f)^{1/2}}{NEP} = \frac{A_{pixel}^{1/2} R_V(T,f)}{V_N} \quad (cm.Hz^{1/2} / Watt) \quad (2.15.a)$$

The responsivities of uncooled infrared detectors are independent of wavelength. In contrast to photon infrared detectors, their responsivities are strongly dependent on wavelength. Therefore, their responsivities and specific detectivities are expressed in $R_V(\lambda)$ and $D^*(\lambda)$.

Response time τ_{th}:

The time required for the pixel signal to decrease to 37% of its value after radiation is removed from the pixel. The unit is seconds.

$$\tau_{th} = C_{th} / K_{th} \quad (2.16)$$

Noise Equivalent Power:

Incident radiation power required to produce a unity ratio of rms signal to rms noise in the detector output. The unit is Watts.

$$NEP = \Phi A_{pixel} \left(\frac{V_N}{V_S}\right) = \frac{V_N}{R_V(T,f)} \quad (2.17)$$

Noise Equivalent Temperature Difference:

The change in temperature of a large blackbody in a scene being viewed by a thermal imaging system which would cause a change in the signal-to-noise ratio of unity in the output of a pixel upon which part of the blackbody is imaged[25]. The unit is degrees K.

$$NETD = \frac{4F^2 V_N}{A_{pixel}\tau_0 R_V(T,f)(\Delta P / \Delta T)_{\lambda 1-\lambda 2}} \tag{2.18}$$

where the temperature contrast $(\Delta P / \Delta T)_{\lambda 1-\lambda 2}$ is given as[21]

$$(\Delta P / \Delta T)_{\lambda 1-\lambda 2} = \int_{\lambda 1}^{\lambda 2} (\partial P(\lambda,T) / \partial T)\tau_a(\lambda)\tau_0(\lambda)s(\lambda)d\lambda \tag{2.19}$$

$P(\lambda,T)$: Planck's function,

$\tau_a(\lambda)$: transmittance of the atmosphere,

$\tau_0(\lambda)$: transmittance of the imaging system's optics,

$s(\lambda)$: spectral response of the sensor, including filters.

Assuming the blackbody temperature is 300K, and $\tau_a(\lambda)$, $\tau_0(\lambda)$ and $s(\lambda)$ are equal to 1, then

For λ=8 um to 14 um; $\Delta P / \Delta T = 2.624 * 10^{-4}$ $Watts / cm^2.K$

For λ=8 um to 12 um; $\Delta P / \Delta T = 1.972 * 10^{-4}$ $Watts / cm^2.K$

For λ=3 um to 5 um; $\Delta P / \Delta T = 2.105 * 10^{-5}$ $Watts / cm^2.K$

Modulation transfer function (MTF)[19, 26]:

An optical transfer function (OTF) is used to theoretically evaluate and optimize the spatial resolution of an imaging system. The optical transfer function (OTF) of an imaging system is similar to the frequency response of an electrical circuit (system). The MTF, modulation transfer function, is the magnitude response of an optical transfer function.

Modulation is the variation of a sinusoidal signal about its average value (Fig. 2.3). It can be considered as the AC amplitude divided by the DC level. The modulation is:

$$\text{Modulation} = \frac{V_{max} - V_{min}}{V_{max} + V_{min}} = \frac{AC}{DC} \tag{2.20}$$

V_{max} and V_{min} are the maximum and minimum signal level respectively. The modulation transfer function is the output modulation produced by the system divided by the input modulation at that frequency:

$$MTF = \frac{Output\ \ Modulation}{Input\ \ Modulation} \tag{2.21}$$

The concept is presented in Fig. 2.4. Three input and output signals are plotted in Figs. 2.4.a and 2.4.b and the MTF is shown in Fig. 2.4.c. As a ratio, the MTF is a relative

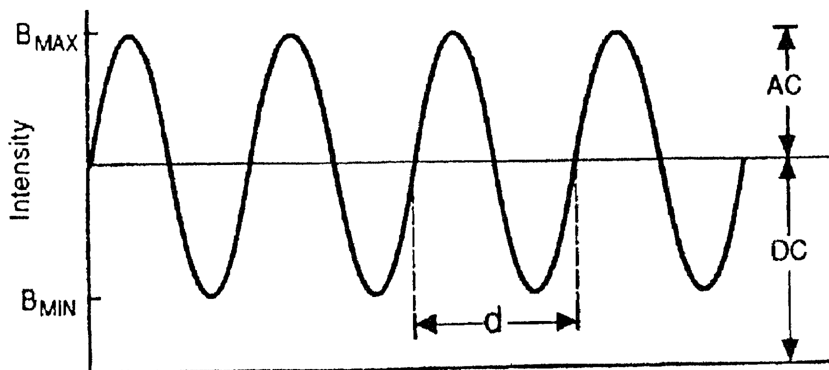

Fig. 2.3 Definition of Target Modulation. d is the extent of one cycle. For optical systems, d is measured in angular space and the spatial frequency is $f_x = 1/d$. For electronic circuitry , d is measured in time and the electrical frequency is $f_{HZ} = 1/d$. (From [19])

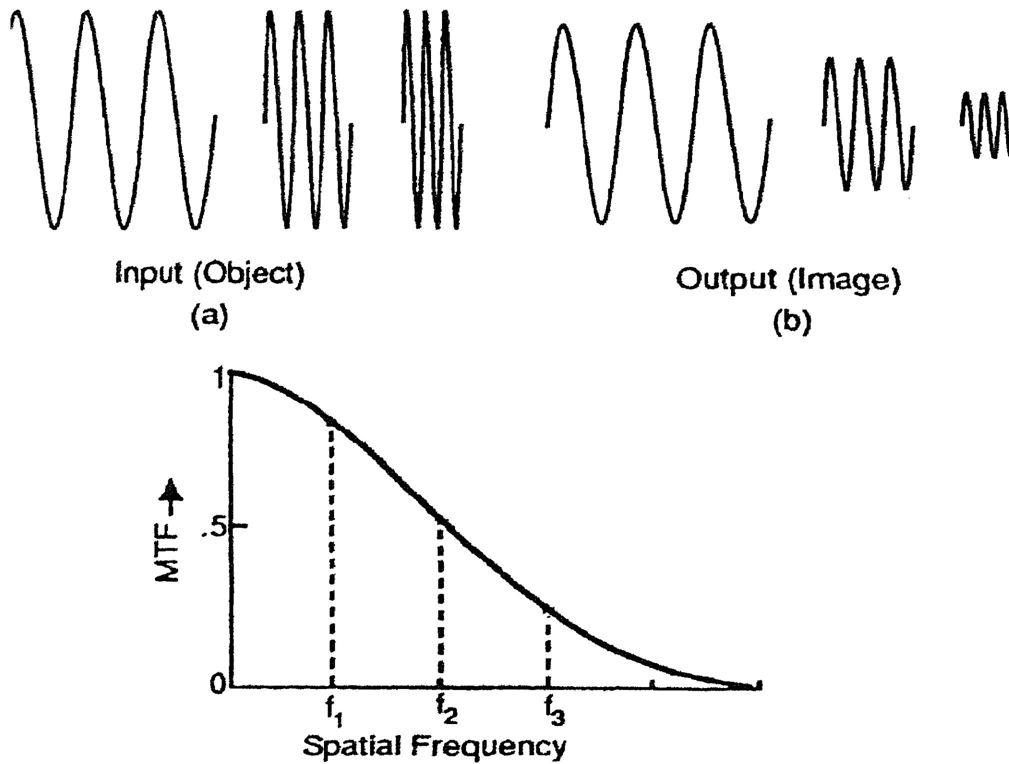

Fig. 2.4 Modulation transfer function. (a) input signal for three difference spatial frequencies, (b) output for the three frequencies, and (c) MTF is the ratio of output-to-input modulation. (From [19])

Table 2.1 Figures of Merit used to describe the performance of a detector.

Figure of Merit	Equation	Units
Responsivity	$R_V(T,f) = \frac{V_S}{\Phi A_{pixel}}$	*Volts / Watt*
Detectivity	$D^*(T,f) = \frac{(A_{pixel}\Delta f)^{1/2}}{NEP}$	$cm.Hz^{1/2}$ / *Watt*
Response time	$\tau_{th} = {C_{th}}/{K_{th}}$	sec*onds*
Noise Equivalent Power	$NEP = \Phi A_{pixel}(\frac{V_N}{V_S})$	*Watts*
Noise Equivalent Temperature Difference	$NETD = \frac{4F^2 V_N}{A_{pixel}\tau_0 R_V(T,f)(\Delta P / \Delta T)_{\lambda 1-\lambda 2}}$	Deg K
A_{pixel}: pixel area (cm^{-2}), V_N : rms noise voltage within system bandwidth,		

Φ : irradiance $(Watts.cm^{-2})$,
V_S : rms signal voltage within system bandwidth,
Δf : equivalent noise bandwidth (Hz),
K_{th} : thermal conductance $(Watt / K)$,
C_{th} : Heat capacity $(Joule / K)$,
F : f/no. of optics,
τ_0 : transmittance of imaging system's optics,
$R_V(T,f)$: responsivity to radiation from blackbody at temperature T,
$(\Delta P / \Delta T)_{\lambda 1-\lambda 2}$: temperature contrast.

The D^* and $NETD$ for a temperature fluctuation noise limited thermal detector are (see Appendix B for details)

$$D^*(T,f) = \left[\frac{\eta^2 A_{pixel}}{4k_B T^2 K_{th}} \right]^{1/2} \tag{2.22}$$

and,

$$NETD = \frac{8TF^2 (k_B \Delta f K_{th})^{1/2}}{\eta A_{pixel} \tau_0 (\Delta P / \Delta T)_{\lambda 1-\lambda 2}} \tag{2.23}$$

The D^* and $NETD$ for a background-noise limited thermal detector are

$$D^*(T,f) = [\eta / 8k_B \sigma (T_D^5 + T_B^5)]^{1/2} \tag{2.24}$$

and,

$$NETD = \frac{4F^2}{\tau_0 (\Delta P / \Delta T)_{\lambda 1-\lambda 2}} \left[\frac{8k_B \sigma \Delta f (T_D^5 + T_B^5)}{\eta A_{pixel}} \right]^{1/2} \tag{2.25}$$

This is the theoretical minimum $NETD$ when the background radiation noise is the dominant noise.

CHAPTER 3

REVIEW OF THE THEORY AND PERFORMANCE OF RESISTIVE BOLOMETER UNCOOLED FOCAL PLANE ARRAYS

3.1 Heat Balance Equations[18, 29-30]

The resistive bolometer effect is a change in the electrical resistance of the responsive element due to temperature changes produced by absorbed incident infrared radiation. Fig. 3.1 shows a dc voltage bias bolometer detector circuit that uses this effect.

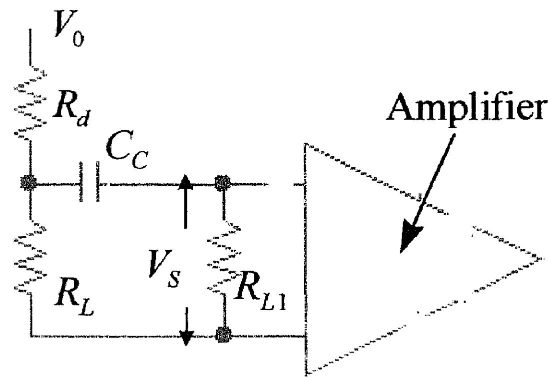

Fig. 3.1 A dc voltage bias bolometer detector circuit.

Consider the heat-equilibrium equation, which determines the temperature of the element.

$$C_{th}\frac{dT}{dt}+K_{th}(T-T_0)=\eta W(t)+i^2R_d \tag{3.1}$$

where

C_{th}: thermal capacitance of the bolometer element,

K_{th}: total thermal conductance from the element to substrate,

T_0: substrate temperature (assumed to be at room temperature),

T: bolometer temperature,

$W(t)$: incident infrared radiant power,

R_d: the resistance of the detector at temperature T,

i: the bias current in bolometer at temperature T,

η: absorbtivity of detector.

Note that both i and R_d depend upon T. If $W(t) = 0$, the time-independent temperature T_m of the bolometer is found from Eq. 3.1

$$K_{th}(T_m - T_0) = I_b^2 R_m \tag{3.2}$$

where T_m is the value of T as $W(t) = 0$, R_m is the value of R_d at temperature T_m and I_b is the value of i at temperature T_m. Presume the temperature coefficient of resistance (TCR), α, which is defined as

$$\alpha \equiv \frac{1}{R_d}\frac{dR_d}{dT}, \tag{3.3}$$

is constant over the range of fluctuations of T. Hence $\alpha(T - T_m)$ is small and a first order approximation is sufficiently accurate. Therefore

$$i^2 R_d = i^2 R_d\big|_{at^\circ T=T_m} + \left.{}^{d(i^2R_d)}\!\big/_{dT}\right|_{at^\circ T=T_m} * \Delta T;\quad \Delta T = T - T_m \tag{3.4}$$

and,

$$\begin{aligned}\left.{}^{d(i^2R_d)}\!\big/_{dT}\right|_{at^\circ T=T_m} &= \left.\frac{d}{dT}\left(\frac{V_0^2 R_d}{(R_L + R_d)^2}\right)\right|_{at^\circ T=T_m}\\ &= \left.\frac{(R_L - R_d)}{(R_L + R_d)^3} V_0^2 \frac{dR_d}{dT}\right|_{at^\circ T=T_m}\\ &= \frac{(R_L - R_m)}{(R_L + R_m)^3} V_0^2 \frac{dR_d}{dT}\end{aligned} \tag{3.5}$$

where V_0 is the bias voltage and R_L is the series load resistance.

Therefore, Eq. 3.4 becomes

$$\begin{aligned} i^2 R_d &= \frac{V_0^2 R_m}{(R_L + R_m)^2} + \frac{(R_L - R_m)}{(R_L + R_m)^3} V_0^2 \alpha R_m (T - T_m) \\ &= \frac{V_0^2 R_m}{(R_L + R_m)^2} \left[1 + \alpha (T - T_m) \frac{(R_L - R_m)}{(R_L + R_m)} \right] \end{aligned} \tag{3.6}$$

The heat-equilibrium equation thus becomes

$$C_{th} \frac{dT}{dt} + K_{th}(T - T_0) - \alpha (T - T_m) \frac{V_0^2 R_m}{(R_L + R_m)^2} \frac{R_L - R_m}{R_L + R_m} = \eta W(t) + \frac{V_0^2 R_m}{(R_L + R_m)^2} \tag{3.7}$$

Rearranging this equation yields

$$\begin{aligned} & C_{th} \frac{d(T - T_m)}{dt} + (T - T_m) \left[K_{th} - \alpha \frac{V_0^2 R_m}{(R_L + R_m)^2} \frac{R_L - R_m}{R_L + R_m} \right] \\ & = \eta W(t) + \frac{V_0^2 R_m}{(R_L + R_m)^2} - K_{th}(T_m - T_0) \end{aligned} \tag{3.8}$$

where the second two terms on the right side of the equation are large (the heating power due to the dc current and the cooling power by conduction through the leads) and substantially cancel, and the variables ($T - T_m$ and $W(t)$) are small.

The radiant power input is chopped to improve the signal-to-noise ratio; that is the input radiant power is a square wave. The differential Eq. 3.8 can be solved by Fourier series expansion of $T - T_m$ and $W(t)$ followed by equating the coefficients. That is, $W(t)$ is written in the form

$$W(t) = W_0 \left[\frac{1}{2} + \frac{2}{\pi} \sin(\omega t) + \frac{2}{3\pi} \sin(3\omega t) + \ldots \right] \tag{3.9}$$

and T in the form

$$T(t) = T_m + T_\omega \sin(\omega t - \psi_1) + T_{3\omega} \sin(3\omega t - \psi_3) + \ldots + T_n \sin(n\omega - \psi_n) \quad \ldots\ldots(3.10)$$

where ω is the angular chopping frequency of the incident radiant power. The zero order coefficients for Eq. 3.8 yield

$$0 = \eta W_0 \frac{1}{2} + \frac{V_0^2 R_m}{(R_L + R_m)^2} - (T_m - T_0) K_{th} \qquad (3.11)$$

The first order coefficients yield

$$T_\omega = \frac{\eta W_0 \frac{2}{\pi}}{\sqrt{\omega^2 C_{th}^2 + K_{eff}^2}} \qquad (3.12)$$

with

$$K_{eff} = \left[K_{th} - \alpha \frac{V_0^2 R_m}{(R_L + R_m)^2} \frac{R_L - R_m}{R_L + R_m} \right] \qquad (3.13)$$

and

$$\psi_1 = \arctan \frac{\omega C_{th}}{K_{eff}}$$

Note that neglecting ηW_0 in the zero order equation and inserting the result in Eq. 3.13 yields an expression which can be defined as an effective thermal conductance K_{eff}

$$K_{eff} = K_{th} \left[1 - \alpha (T_m - T_0) \frac{R_L - R_m}{R_L + R_m} \right] \qquad (3.14)$$

Also, for chopping angular frequencies greater than K_{eff}/C_{th} the amplitude of the fluctuations of T will decrease approximately inversely with ω. The second order coefficients (and all other even-order coefficients) vanish, and for higher odd-order coefficients $T_{n\omega}$ falls off like $1/n^2$ because

$$W_{n\omega} = W_0 \frac{2}{n\pi} \qquad (3.15)$$

and the derivative contributes another $1/n$. Thus T can be approximated by $T_m + T_\omega \sin(\omega t - \psi_1)$. This approximation, of course, is the exact solution for an input

$$W(t) = W_0\left[\frac{1}{2} + \frac{2}{\pi}\sin(\omega t)\right] \tag{3.16}$$

which are just the first two terms of the Fourier expansion of the square wave.

The output signal V_S due to an incident $W(t)$ is computed by inserting the resulting T, and thus R_d, into the expression for V_S, the ac voltage across R_L in Fig. 3.1.

$$V_S = V_0\left[\frac{R_L}{R_d + R_L} - \frac{R_L}{R_m + R_L}\right] \tag{3.17}$$

Consider a first order approximation,

$$\begin{aligned}\frac{R_L}{R_d + R_L} &= \left.\frac{R_L}{R_d + R_L}\right|_{at^\circ R_d = R_m} + \frac{d}{dT}\left.\left(\frac{R_L}{R_d + R_L}\right)\right|_{at^\circ R_d = R_m} * (T - T_m) \\ &= \frac{R_L}{R_m + R_L} - \frac{R_L R_m \alpha}{(R_m + R_L)^2} T_\omega \sin(\omega t - \psi_1)\end{aligned} \tag{3.18}$$

Therefore, the first order approximation of V_S is

$$V_S = -I_b R_m \alpha \frac{R_L}{R_L + R_m} T_\omega \sin(\omega t - \psi_1) \tag{3.19}$$

where I_b is the dc bias current when $R_d = R_m$.

The output voltage of a detector array should be multiplied by a fill factor (F_A), because the incident power $W(t)$ is only absorbed in an effective area (A_{eff}) of a pixel with bolometer material. Therefore,

$$V_S = -I_b R_m \alpha F_A \frac{R_L}{R_L + R_m} T_\omega \sin(\omega t - \psi_1) \tag{3.19.a}$$

The voltage responsivity is

$$R_V = \left|\frac{V_S}{W(t)}\right| = \frac{R_L}{R_L + R_m} * \frac{I_b \eta \alpha R_m F_A}{[K_{eff}^2 + \omega^2 C_{th}^2]^{1/2}} \quad (3.20)$$

When $R_L = R_m$, the responsivity R_V has a maximum value of

$$R_V = \frac{1}{2} * \frac{I_b \eta \alpha R_m F_A}{[K_{eff}^2 + \omega^2 C_{th}^2]^{1/2}} \quad (3.21)$$

and

$$K_{eff} = K_{th}.$$

Replacing I_b in Eq. 3.20 with $\left[(T_m - T_0)K_{th}\right]^{1/2}.R_m^{-1/2}$, the responsivity R_V becomes

$$R_V = \frac{R_L}{R_L + R_m} * \frac{\eta \alpha F_A}{K_{eff}[1 + 4\pi^2 f^2 \tau_{th}^2]^{1/2}} * (K_{th} R_m (T_m - T_0))^{1/2}; \quad \tau_{th} = C_{th} / K_{eff} \quad (3.22)$$

If $4\pi^2 f^2 \tau_{th}^2 << 1$, the low frequency responsivity becomes

$$R_V = \eta \alpha F_A \left(\frac{R_L}{R_L + R_m}\right) * \left(\frac{(K_{th} R_m (T_m - T_0))}{K_{eff}^2}\right)^{1/2} \quad (3.23)$$

If $4\pi^2 f^2 \tau_{th}^2 >> 1$, the high frequency responsivity would be

$$R_V = \eta \alpha F_A \left(\frac{R_L}{R_L + R_m}\right) * \left(\frac{(K_{th} R_m (T_m - T_0))}{\omega^2 C_{th}^2}\right)^{1/2} \quad (3.24)$$

Fig. 3.2 shows another kind of bias circuit, with a constant dc current source.

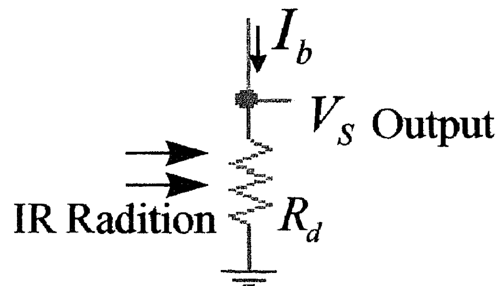

Fig. 3.2 Constant dc current bias circuit

Using the same approximation as previously used to solve Eq. 3.1, the effective thermal conductance, output voltage, and voltage responsivity would be

$$K_{eff} = [K_{th} - \alpha I_b^2 R_m)] = K_{th}[1 - \alpha(T_m - T)] \tag{3.25}$$

$$V_S = I_b R_m \alpha F_A T_\omega \sin(\omega t - \psi_1) \tag{3.26}$$

and

$$R_V = \frac{I_b \eta \alpha R_m F_A}{[K_{eff}^2 + \omega^2 C_{th}^2]^{1/2}} \tag{3.27}$$

The three main areas of bolometer focal plane array research are the thermal isolation structure, the readout integrated circuit, and the bolometer material. They are described in turn as follows.

3.2 The Thermal Isolation Structure for a Bolometer Focal Plane Arrays

The operating principle of a bolometer detector is that the incident infrared radiant power is absorbed by the detector element and converted to heat. This heat causes the temperature of the detector to change. The resistance of the bolometer material, which is a function of temperature, changes according to the detector temperature. From Eq. 3.20, the voltage responsivity is directly proportional to the effective thermal conductance K_{eff}. Minimizing K_{eff} through a good thermal isolation structure of the bolometer will generate high responsivity.

A schematic representation of a microbridge thermal structure to provide high thermal resistance is shown in Fig. 3.3.

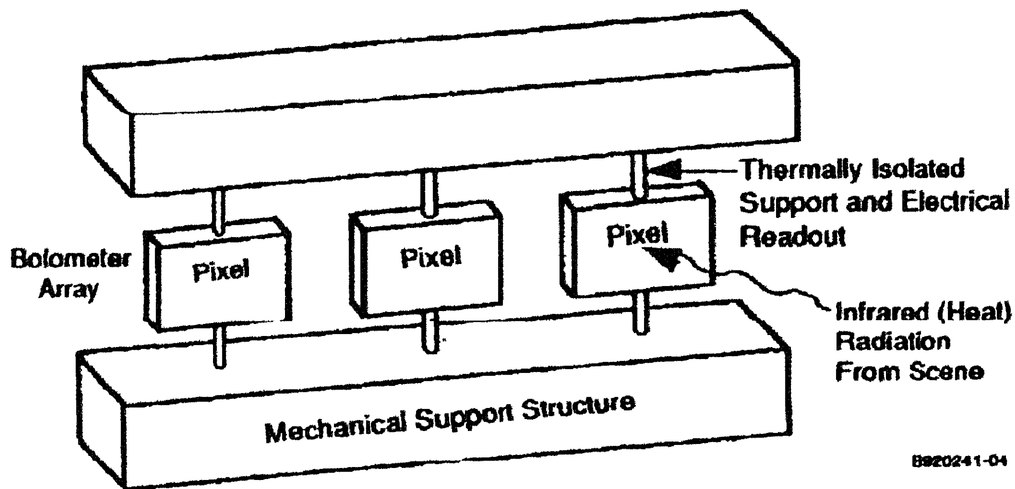

Fig. 3.3 Schematic diagram of a microbridge thermal structure.

The microbridge detector elements are supported on legs above the plane of the microcircuit (in the substrate). The legs are designed to provide the required high thermal resistance between the suspended plate and its surroundings, allowing the plate to response to incident IR radiation by being heated or cooled, and carry electrical conductors from the detector to microcircuit. The thermal response time of these structures can be adjusted by geometry and materials employed to provide an optimum value for TV-frame-rate imaging (33ms per frame). The thermal isolation structure should balance the conflicting requirements of minimizing thermal conductance and still providing sufficient mechanical strength and high fill factor. The detector also has to be designed with high absorption efficiency in the 8 to 12um wavelength range.

Two examples of such structures are discussed. They are being developed by Honeywell Corp. and Defense Science and Technology Organization of Australia (DSTO).

Fig. 3.4.a describes the microbolometer cell and the FPA designed by Honeywell. Optical and scanning electron microscope photographs of a microbolometer detector on CMOS integrated circuit substrates are shown in Fig. 3.4.b. The microbridge material is silicon nitride and a VO_x thin film with a resistivity of 0.1 ohm-cm and a TCR of 2%[32] is deposited on the top. The total thickness of the silicon nitride and VO_x thin film is typically 0.5um. The spacing between the microbridge and the substrate was selected to maximize the pixel absorption in the 8 to 12um wavelength range and is typically 2.5um. The underlying silicon contains monolithic readout electronics and an IR reflector designed to increase the IR absorption of the bolometer to about 80% of maximum efficiency while minimizing thermal capacitance. The relatively broad resonator response is designed for the 8 to 12um wavelength range.

Fig. 3.5.a shows a prototype sandwich-gap type microbridge structure designed earlier by DSTO. An electron micrograph of a DSTO's bolometer element is shown in Fig. 3.5.b. A corner of the detector magnified so as to illustrate the thin supports is shown in Fig. 3.5.c.

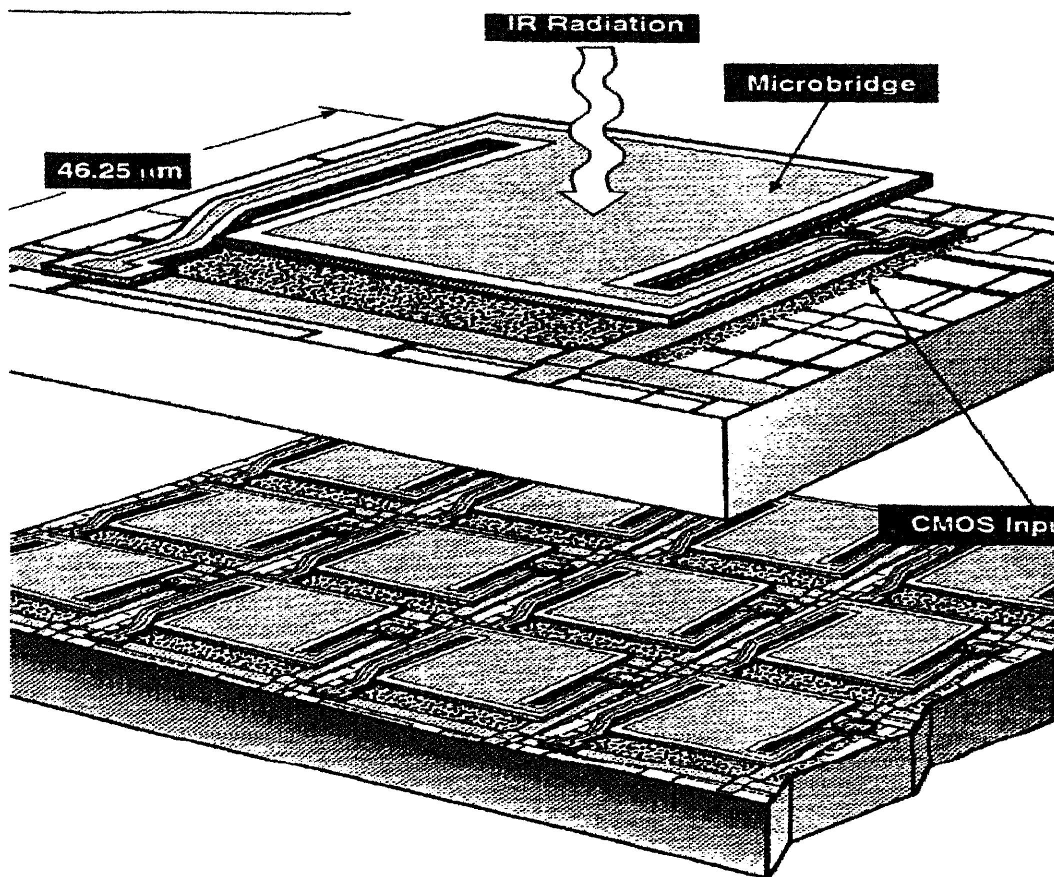

(a) The Honeywell's microbolometer cell and FPA.

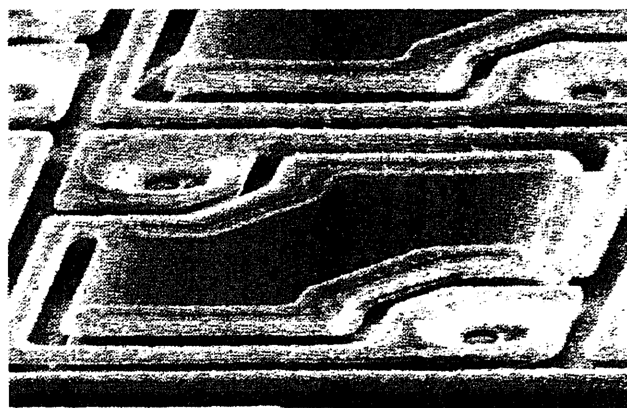

(b) scanning electron microscope photographs of a microblometer detector on CMOS integrated circuit substrates

Fig. 3.4 (a) The Honeywell's microbolometer cell and FPA. (b) scanning electron microscope photographs of a microblometer detector on CMOS integrated circuit substrates. (From [36])

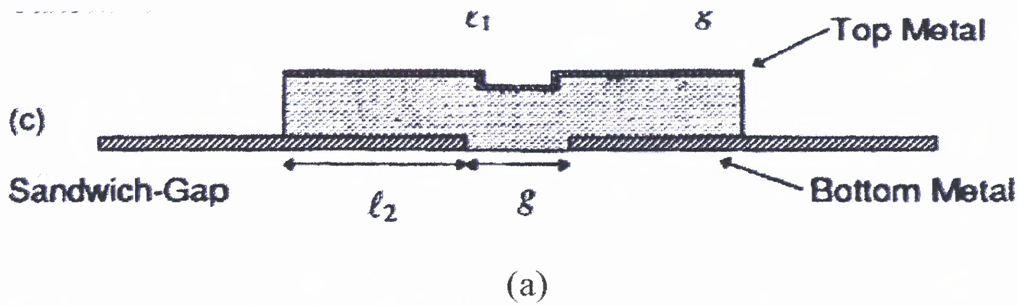

(a)

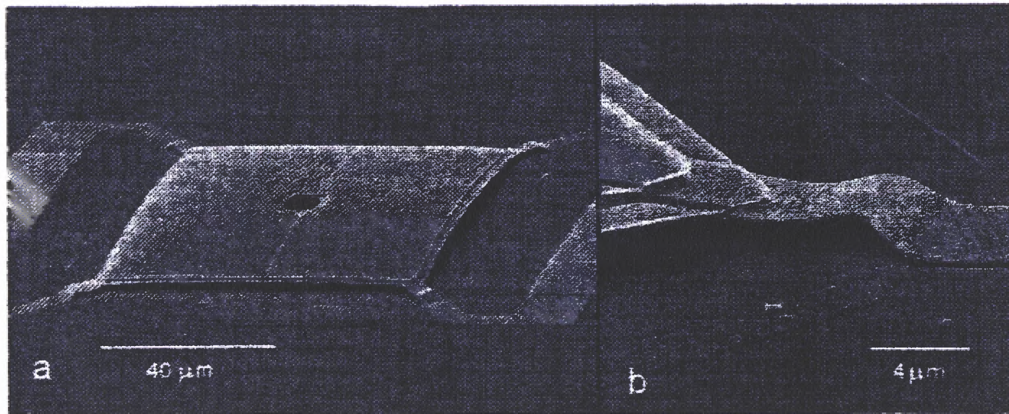

(b) and (c)

Fig. 3.5(a) A sandwich-gap type microbridge structure designed by DSTO. (b) SEM photographs of a semiconductor film bolometer element. (c) Enlargement of a corner of Fig. 3.5.b showing the bottom metal acting as a support for the thermally isolated detector. ((a) from [22]; (b) and (c) from [49])

The detector resistance of a sandwich-gap type is given by

$$R_e = \frac{2\rho dg}{w(2d^2 + \mathrm{lg})} \tag{3.28}$$

where ρ is the resistivity, g is the gap length, d is the thickness of the detector, w is the detector width, and l is the length of the bottom contact (see Fig. 3.5.a).

High efficiency IR absorption can be achieved by forming an optical cavity comprising a metal layer having a sheet resistance of 377 Ω per square[42] onto which radiation is incident, separated from a highly reflecting metal film by a quarter wave spacing of $\lambda_{\max} / 4n$, where $\lambda_{\max}$ is the wavelength of maximum absorption and n is the

refractive index of the spacer layer (Fig. 3.6[44]). This type of structure can yield 90% absorption integrated over the 8-13um waveband. However, the additional thin film components result in a significant increase in thermal capacitance, and hence slows the speed of response.

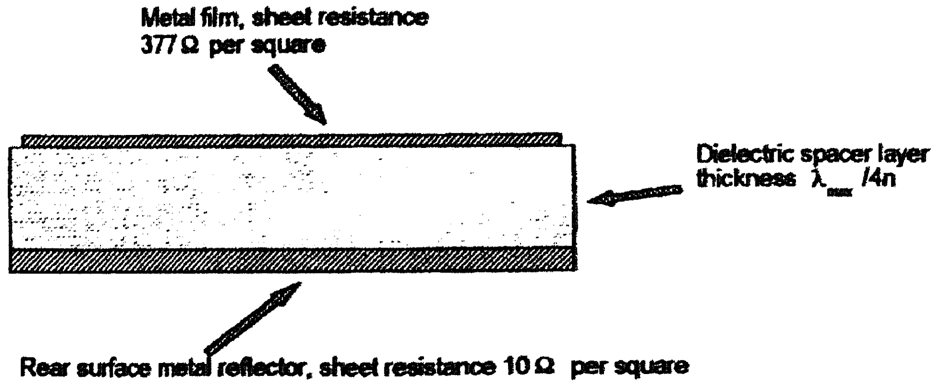

Fig. 3.6 Infrared absorption structure for thin film detectors. (From [44])

The thermal conductance K_{th} in Eq. 3.20 can be expressed as

$$K_{th} = K_r + K_p + K_g \tag{3.29}$$

where K_r is the conductance due to radiation exchange, given by

$$K_r = 4A_{eff}\eta\alpha T_0^3 \tag{3.30}$$

Eq. 3.30 is applicable to radiation from a single surface, as for the case of optical cavity designs. A_{eff} is the effective detector area of the detector, T_0 is the ambient background temperature (^0K), and σ is the Stefan-Boltzmann constant ($5.67*10^{-12}\ Watts/cm^2.K^4$).

K_p is the conductance due to thermal loss via the solid structure which connects the detector to substrate. To first approximation

$$K_p = \frac{KA_{th}}{L} \tag{3.31}$$

where K is the thermal conductivity of the thermal loss path, A_{th} is the average cross section area of the thermal loss path , and L is the length of the thermal loss path.

K_g is the conductance due to gaseous conductance loss. The analysis of gas-filled detector packages is complex. However, the gaseous conductance can not be neglected when a detector is not working in vacuum, especially when the K_p is very small. An example is shown in Fig. 3.7. In order to have the best possible performance, a bolometer array should be packaged in vacuum.

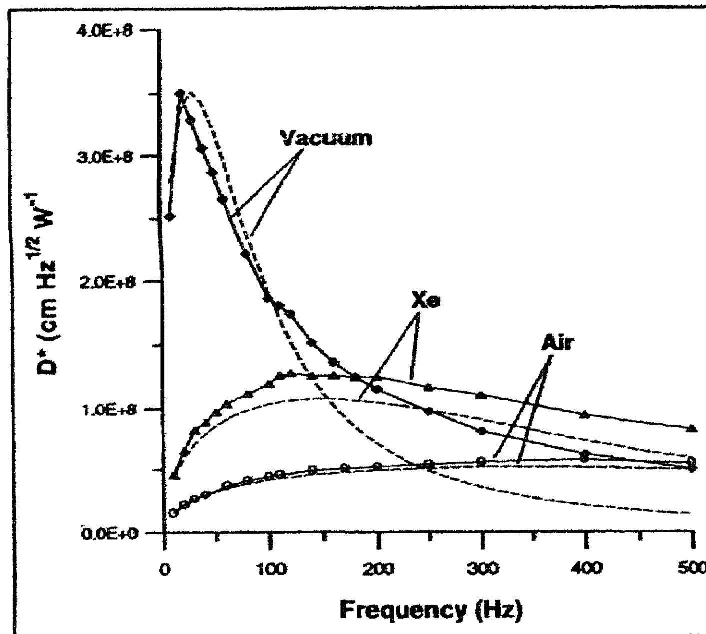

Fig. 3.7 Measured (solid lines) and modeled (dashed lines) performance of an a-Si bolometer developed by DSTO, as a function of frequency, for 70*70um detector packaged in (a) Vacuum, (b) Xe, and (c) Air (N_2). (From [49])

3.3 The Readout Integrated Circuit (ROIC)

The primary noise sources for a typical bolometer focal plane array are:

1. The fundamental or limiting thermal noise seen as temperature fluctuations in the detector.
2. The noise term associated with the bolometer material; that is the Johnson noise and excess noise.
3. The noise terms due to the silicon readout circuit. This is a matter of preamplifier and multiplexer design. An important feature is that this design will also determine the device noise bandwidth..
4. The fixed pattern noise (FPN) due to the pixel-to-pixel detector resistance variation. The noise due to the inaccurate timing of the pulse bias and the signal capturing when the pulse bias method is used.

These noise sources are discussed in turn as follows.

Consider the dc voltage bias bolometer detector circuit of Fig. 3.1, the noise equivalent circuit of Fig. 3.1 is shown in Fig. 3.8.

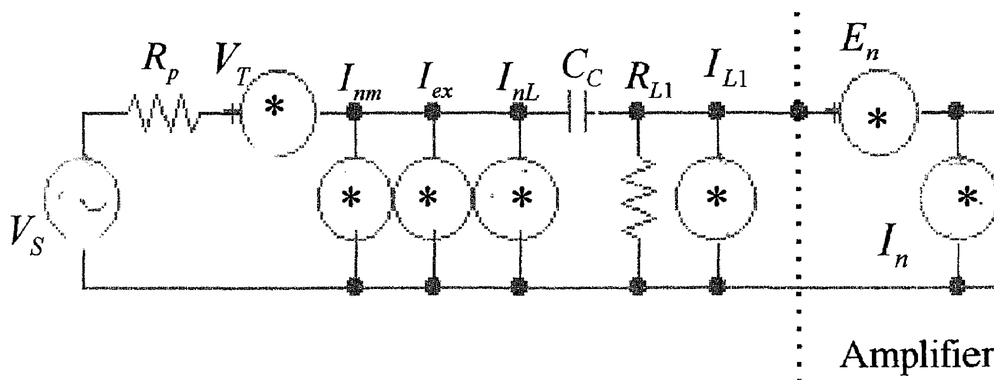

Fig. 3.8 Noise equivalent circuit of Fig. 3.1.

where

C_C : coupling capacitor,

R_{L1} : load resistance for amplifier input,

R_m : detector resistance,

R_L : load resistance for bias circuit,

V_S : signal voltage,

I_{nL} : Johnson noise current of R_L,

I_{nm} : Johnson noise current of R_m,

I_{ex} : excess noise current of R_m,

I_{L1} : Johnson noise current of R_{L1},

I_n : equivalent noise current of amplifier,

E_n : equivalent noise voltage of amplifier,

V_T : temperature fluctuation noise,

$R_p = R_m // R_L$.

The equivalent output noise voltage E_{So} would be

$$\begin{aligned} E_{So}^2 = E_n^2 + (I_n^2 + I_{L1}^2)\left|(R_p + \frac{1}{j\omega C_C}) // R_{L1}\right|^2 \\ + (I_{nL}^2 + I_{nm}^2 + I_{ex}^2) * \frac{R_p^2}{\left|R_p + \frac{1}{j\omega C_C}\right|^2} * \left|(R_p + \frac{1}{j\omega C_C}) // R_{L1}\right|^2 \\ + V_T^2 * \frac{1}{\left|R_p + \frac{1}{j\omega C_C}\right|^2} * \left|(R_p + \frac{1}{j\omega C_C}) // R_{L1}\right|^2 \end{aligned} \tag{3.32}$$

Transferring the equivalent output noise voltage E_{So} to the input, we get the equivalent input noise voltage E_{Si} as Fig. 3.9.

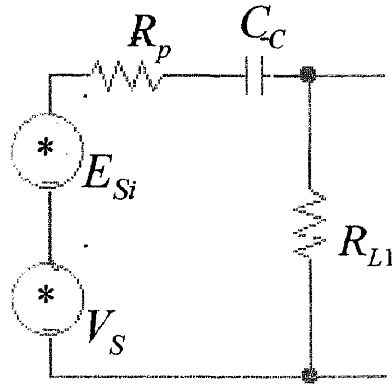

Fig. 3.9 The equivalent circuit of Fig. 3.8.

$$E_{Si}^2 = \frac{E_n^2}{\left|(R_p + \frac{1}{j\omega C_C}) // R_{L1}\right|^2} * \left|R_p + \frac{1}{j\omega C_C}\right|^2 + (I_{nL}^2 + L_{nm}^2 + I_{ex}^2) * R_p^2 + V_T^2 + (I_n^2 + I_{L1}^2) * \left|R_p + \frac{1}{j\omega C_C}\right|^2 \quad (3.33)$$

For $R_{L1} >> R_p$ and $R_p >> \frac{1}{\omega C_C}$, Eq. 3.33 becomes

$$E_{Si}^2 = E_n^2 + (I_{nL}^2 + L_{nm}^2 + I_{ex}^2 + I_n^2) * R_p^2 + V_T^2 \quad (3.34)$$

1. Temperature fluctuation noise

The rms value of the temperature fluctuation power spectrum , derived at appendix A, is

$$\Delta W_T = (4 k_B T^2 K_{th})^{1/2}$$

One-half this fluctuation is due to the fluctuating emission of radiation, and the other half is due to the fluctuating absorption. Therefore

$$\Delta W_T = (2 k_B K_{th} (T_0^2 + T_m^2))^{1/2} \tag{3.35}$$

The temperature noise voltage is calculated by treating ΔW_T in the same way as an incoming signal. Hence, the temperature fluctuation noise is

$$V_T = \left(\frac{2k_B K_{th} (T_0^2 + T_m^2)}{\eta^2} \right)^{1/2} * R_V \quad (V / Hz^{1/2}) \tag{3.36}$$

2. Johnson noise

From Eq. 3.34, the Johnson noise voltage of resistance R_m and R_L is

$$\begin{aligned} V_J &= \left(I_{nL}^2 + I_{nm}^2 \right)^{1/2} * R_p \\ &= \left[4k_B * \frac{R_L R_m}{(R_L + R_m)^2} * (T_0 R_m + T_m R_L) \right]^{1/2} \quad (V / Hz^{1/2}) \end{aligned} \tag{3.37}$$

where

$$I_{nL} = \left(\frac{4k_B T_0}{R_L} \right)^{1/2} \quad (A / Hz^{1/2}) \tag{3.38}$$

$$I_{nm} = \left(\frac{4k_B T_m}{R_m} \right)^{1/2} \quad (A / Hz^{1/2}) \tag{3.39}$$

The excess noise of R_m, V_{ex}, can contain various components such as 1/f noise $V_{1/f}$ and random telegraph switching (RTS) noise V_{RTS}. The 1/f noise and RTS noise component of the excess noise are given by the expressions[51]

$$V_{1/f} = const. \frac{I^b R_d}{(Nf)^{1/2}} \tag{3.40}$$

$$V_{RTS} = \left[\sum_{i=1}^{i=n} \frac{2(\Delta v_i)^2 \tau_i}{4 + (2\pi f \tau_i)^2} \right]^{1/2} \tag{3.41}$$

where $V_{1/f}$ and V_{RTS} are the respective noise voltage, b is approximately unity and N is the number of charge carrier. RTS noise is composed of a number (n) of switching processes where each switching process is due to a defect center and is characterized by an average switch-on/switch-off time τ_i and a measured voltage step change Δv_i for each. The excess noise is the dominant noise source in the a-Si microbolometer FPA developed by DSTO.

If the performance of the detector is limited by Johnson noise, the detectivity D^* is

$$D^* = \frac{\left(A_{pixel}\Delta f\right)^{1/2}}{NEP} = \frac{A_{pixel}^{1/2} R_V}{V_J} \tag{3.42}$$

where A_{pixel} is the pixel area of the detector, V_J is the Johnson noise voltage, and R_V is the voltage responsivity. Assuming the conductance is a constant over the operating temperature range, using Eqs. 3.20 and 3.37 to solve Eq. 3.42 for the detectivity gives

$$\begin{aligned} D^* &= F_A \eta I_b \left(\frac{A_{pixel}\alpha^2 R_m^2 R_L}{4k_B R_m (R_L T_m + R_m T_0)} \right)^{1/2} * \frac{1}{\left(K_{eff}^2 + \omega^2 C_{th}^2\right)^{1/2}} \\ &= F_A \eta \left(\frac{\alpha^2 R_L}{4k_B R_m \left(1 + \frac{R_L}{R_m}\right)(R_L T_m + R_m T_0)} \right)^{1/2} * \frac{A_{pixel}^{1/2} V_0}{\left(K_{eff}^2 + \omega^2 C_{th}^2\right)^{1/2}} \\ &= \left(\frac{\alpha}{R_m^{1/2}}\right) \left(\frac{A_{pixel} R_L}{4k_B \left(K_{eff}^2 + \omega^2 C_{th}^2\right)\left(1 + \frac{R_L}{R_m}\right)(R_L T_m + R_m T_0)} \right)^{1/2} F_A \eta V_0 \end{aligned} \tag{3.43}$$

The first term in Eq. 3.43 is defined as the figure of merit of the bolometric material under fixed voltage bias conditions when Johnson noise in the resistor is the dominant noise.

$$F_{bol} = \frac{\alpha}{R_m^{1/2}} \tag{3.44}$$

It is apparently that the development of new materials with high TCR and low resistance would improve bolometer performance.

3. Preamplifier noise[20]

A noise model for amplifier is shown in Fig. 3.10. Amplifier noise is represented completely by a zero impedance voltage generator E_n in series with the input port, an infinite impedance current generator I_n in parallel with the input, and by a complex correlation coefficient C (not shown). Each of these terms typically are frequency dependent.

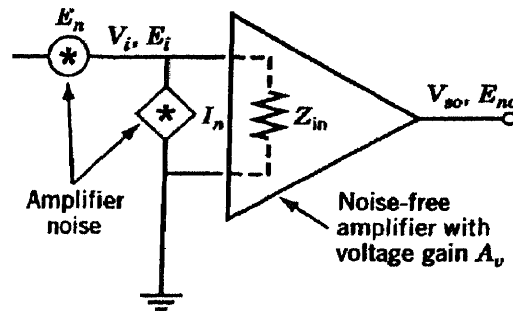

Fig. 3.10 A noise model of amplifiers. (From reference 20.)

The two noise sources of a MOSFET amplifier are current noise I_n and voltage noise E_n. They are given by [20]

$$I_n = \left(2qI_{GSS}\right)^{1/2} \quad (A / Hz^{1/2}) \tag{3.45}$$

and

$$E_n = \left(\frac{8k_B T}{3g_m} + \frac{K_F I_{Dq}^{AF}}{g_m^2 f C_{OX} L_{eff}^2} \right)^{1/2}$$

$$= \left(V_a^2 + \frac{Z_a^2}{f} \right)^{1/2} \quad (V / Hz^{1/2}) \tag{3.46}$$

where q is the electronic charge, I_{GSS} is the gate leakage current of a MOSFET, g_m is the transconductance of a MOSFET, C_{OX} is the gate oxide capacitance, L_{eff} is the effective channel length, K_F is the flicker noise coefficient, A_F is a constant, I_{DQ} is the quiescent drain current, and f is the frequency of operation.

The BJT amplifier noise sources I_n and E_n are represented by [20]

$$I_n = \left(2qI_B + \frac{2qf_L I_B^\gamma}{f} + 2qI_C \left(\frac{f}{f_T} \right)^2 \right)^{1/2} \quad (A / Hz^{1/2}) \tag{3.47}$$

and

$$E_n = \left(4k_B T r_x + 2qI_C r_e^2 + \frac{2qf_L I_B^\gamma r_x'^2}{f} + 2qI_C r_x^2 \left(\frac{f}{f_T} \right)^2 \right)^{1/2} \quad (V / Hz^{1/2}) \tag{3.48}$$

where q is the electronic charge, I_B is the base current, I_C is the collector current, f_L is a representation of the noise corner frequency, having values from 3.7 KHz to 7 MHz, f_T represents the frequency at which the common-emitter short-circuit current gain equals unity, r_x is the base spreading resistance, r_e is the Shockley emitter resistance, k_B is the Boltzmann's constant, r_x' is the $1/f$ base spreading resistance ($r_x' \approx r_x / 2$), and f is the frequency of operation. I_n and E_n are strongly dependent on collector current.

Noise current and voltage for typical low-noise transistor technologies in the common source (or common emitter) configuration are plotted in Fig. 3.11.

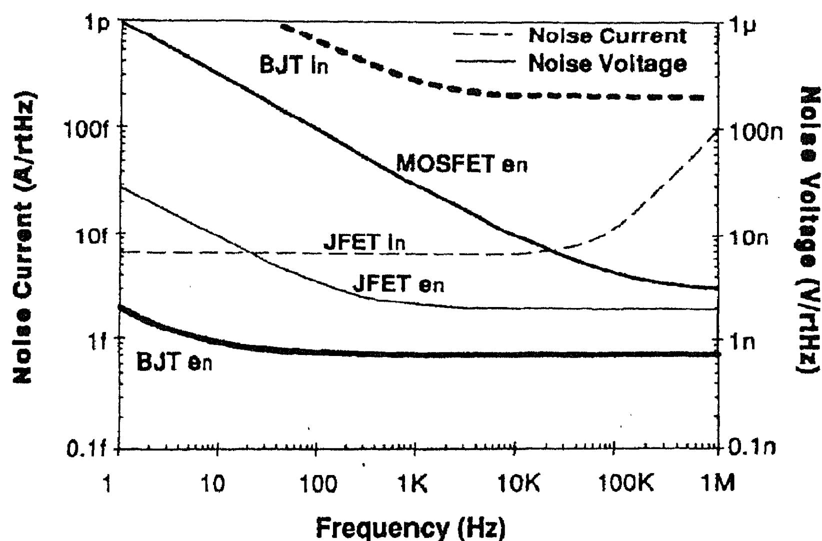

Fig. 3.11 Noise voltage and current for typical low-noise BJTs, JFETs, and MOSFETs. NOSFET noise current is negligible. (From [53])

The selection of an input stage of a preamplifier depends primarily on the signal source impedance and frequency range. It is difficult to say exactly where each type of device should be used. A general guide is shown in Fig. 3.12.

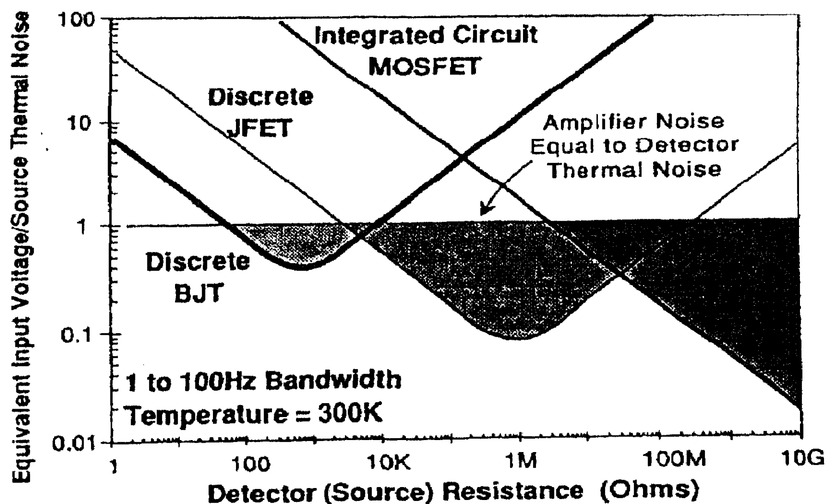

Fig. 3.12 Guide for selection of input stage. (From [53])

If the detector resistance is about $1M\Omega$, FETs are more desirable for the input stage because of their very low noise current I_n $(\sim 10\, fA / Hz^{1/2})$. A typical JFET has an E_n slightly larger than that of a bipolar transistor, but its I_n is significantly lower. If the detector resistance is about $10K\Omega$, as the bolometer resistance of Honeywell's FPA, bipolar transistors are more suitable input stage. In Honeywell's FPA, every pixel has a bipolar transistor under the suspended microbridge as shown in Fig. 3.4.

Two examples for calculated bolometer performances are now given based on the following reasonable assumptions.

Assuming

$K_{th} = 2.4 * 10^{-6} (W/^0K)$ (Thermal conductance),

$C_{th} = 2.5 * 10^{-9} (J/^0K)$ (Thermal capacitance),

$\eta = 0.8$ (Absorbtivity of detector),

$TCR = 2\%$ (Temperature of coefficient),

$A_{pixel} = 50 * 50 (um^2)$ (Pixel area),

$F_A = 0.5$ (Fill factor),

$V_0 = 5(V)$ (Bias voltage),

$T_0 = 300(^0K)$ (Substrate temperature).

and,

$\sigma = 5.67 * 10^{-12} (W / cm^2 K^4)$ (Stefan-Boltzmann constant),

$k_B = 1.38 * 10^{-23} (W.S/^0K)$ (Boltzmann's constant).

For example 1: $R_m = R_L = 1M\Omega$

The detector temperature (T_m), the temperature fluctuation noise voltage (V_T) and the Johnson noise voltage (V_J) calculated using Eqs. 3.2, 3.36 and 3.37 would be

$$\begin{aligned} T_m &= T_0 + \frac{1}{K_{th}} * \left(\frac{V_0}{R_L + R_m} \right)^2 * R_m \\ &= 302.6(^0K) \end{aligned} \tag{3.49}$$

$$\begin{aligned} V_T &= \left(\frac{2k_B K_{th} (T_0^2 + T_m^2)}{\eta^2} \right)^{1/2} * R_V \\ &= \frac{2.554 * 10^{-8}}{(1 + \omega^2 \tau^2)^{1/2}} \quad (V / Hz^{1/2}) \end{aligned} \tag{3.50}$$

$$\begin{aligned} V_J &= \left[4k_B * \frac{R_L R_m}{(R_L + R_m)^2} * (T_0 R_m + T_m R_L) \right]^{1/2} \\ &= 9.12 * 10^{-8} \quad (V / Hz^{1/2}) \end{aligned} \tag{3.51}$$

Since the detector resistance R_m is $1M\Omega$, from Fig. 3.12, an FET would be a suitable device for the preamplifier for this example. A low noise JFET 2N3821 could be chosen. Its equivalent noise current (I_n) is about $3\,fA / Hz^{1/2}$ for frequencies below 10KHz and its equivalent noise voltage (E_n) would be about $6nV / Hz^{1/2}$. The amplifier noise voltage (V_A) would be

$$\begin{aligned} V_A &= \left[I_n^2 R_p^2 + E_n^2 \right]^{1/2} \\ &= 6nV / Hz^{1/2} \end{aligned} \tag{3.52}$$

The power consumption per pixel is $6.25uW$. Assuming there are 256*256 pixels in a focal plane array, then the minimum power consumption is $0.4096\ Watts$. The numerical calculations of noise voltages and normalized detectivity are shown in Fig. 3.13.

Example 2: : $R_m = R_L = 10K\Omega$

The detector temperature (T_m) would be $T_m = 560.41(^0K)$ and the power consumption would be unreasonably high as 163.84 watts for 256*256 pixels, if dc bias was used.

Therefore, it would be advantages to use pulse biasing. For example, if the detector is biased by a voltage pulse with a pulse width 5us, the thermal time constant $\tau_{th} = \frac{C_{th}}{K_{th}}$, 1.04ms, would be much longer than the pulse width. Therefore, the detector temperature T_m would not rise significantly and can be shown using the linearly approximation below

$$\begin{aligned} T_m &= T_0 + \frac{1}{K_{th}} * \left(\frac{V_0}{R_L + R_m} \right)^2 * R_m * \frac{5us}{\tau_{th}} \\ &= 301.25(^0K) \end{aligned} \tag{3.53}$$

The Johnson noise voltage (V_J) for pulse bias would be

$$\begin{aligned} V_J &= \left[4k_B * \frac{R_L R_m}{(R_L + R_m)^2} * (T_0 R_m + T_m R_L) \right]^{1/2} \\ &= 9.12 * 10^{-9} \quad (V / Hz^{1/2}) \end{aligned} \tag{3.54}$$

The pulse bias Johnson noise voltage is also plotted in Fig. 3.13. According to Eqs. 3.50 to 3.52, the thermal noise is the dominant noise for $R_m = R_L = 1M\Omega$. The thermal noise can be reduced by using lower resistivity material, but the detector temperature and power consumption will increase as in example 2. Therefore, a pulse bias method is necessary for a microbolometer focal plane array.

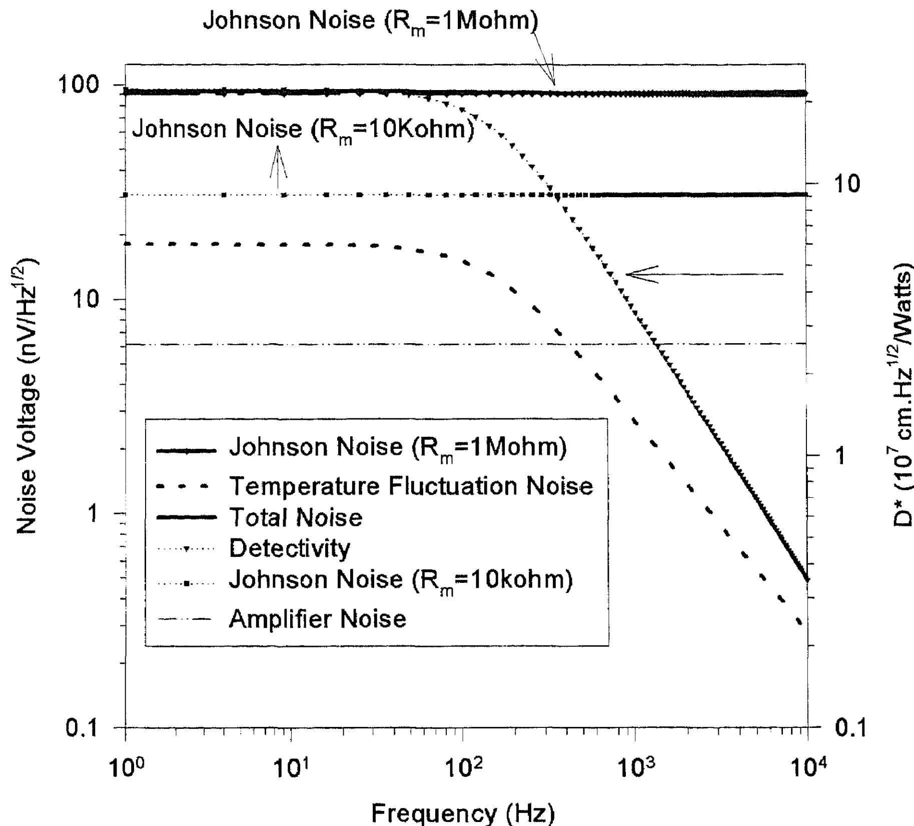

Fig. 3.13 Numerical calculations of noise voltage and normalized detectivity. The Johnson noise voltage for R_m =1Mohm and total noise voltage are superimposed in this figure.

The use of pulse bias allows a large number of detectors to be addressed at low average power consumption. Furthermore, since the pulse duration can be significantly smaller than the thermal time constant, the detector temperature does not reach the dc bias level, and a high voltage can be used with consequent increase in responsivity. However, the use of high voltage pulses causes a rapid temperature increase added to the temperature generated by incident power. If the time from the start of pulse bias to the actual sampling of detector temperature is not stable, a noise contribution will appear.

Accurate timing is therefore needed. However, another aspect becomes important in a columnwise parallel signal conditioning and A/D conversion architecture if the detector data are repeatedly sampled during a pulse bias period. In such a concept the sampled data change during the pulse bias time, since the detector is heated from near ambient temperature at the start of the pulse bias internal to a several degrees higher temperature at the end of the interval. This means that the input range of signal conditioning circuits must be large enough to handle not only the data and FPN signals, but also the ramp bias signal. Thereby, the demands on the dynamic range of the signal conditioning circuits increase and the temperature resolution specifications may be more difficult to meet. To avoid extra signal conditioning design challenges and poorer performance, compensation of the detector temperature rise must be made[48].

The expression for noise equivalent temperature noise $NETD$ [25] is

$$NETD = \frac{4F^2 \Delta f^{1/2}}{A_{pixel} \tau_0 D^* (\Delta P / \Delta T)_{\lambda 1 - \lambda 2}} \tag{3.55}$$

where F is the f/no of optics, A_{pixel} is the pixel area, D^* is detectivity, τ_0 is the transmittance of imaging system's optics, $(\Delta P / \Delta T)_{\lambda 1 - \lambda 2}$ is the temperature constant ($\sim 1.972 * 10^{-4} Watts / cm^2 K$ for $\lambda = 8$ to 12um), and Δf is the noise bandwidth.

The noise bandwidth in $NETD$ depends on the signal conditioning architecture. Three basic and alternative signal conditioning approaches can be recognized. The first is the serial ADC, involving X-Y multiplexing of sensor data to a single on-chip ADC. The second option is pixelwise A/D conversion with an ADC dedicated to every detector. The third approach is columnwise A/D conversion with a degree of signal conditioning parallelism lying between the first two concepts[46].

1. Pixelwise A/D conversion[46]

The pixelwise A/D conversion approach has an ADC next to every detector. The advantages are that no signal degradation occurs when digital data are read out of the detector array, and that the infrared radiation incident on the detector can be sensed and electrically integrated during the whole frame period. The digital readout and the relatively low bandwidth requirement of the ADC, set by the frame rate, indicate that this kind of structure can give the highest signal-to-noise ratio (SNR). On the other hand, this high performance is outweighed in practice by very stringent demands on size and power consumption for the ADC and signal conditioning circuits.

2. Serial A/D conversion[46]

For the serial ADC architecture the conditions are the opposite to the pixelwise A/D conversion. All available power and area can now be used for the single ADC, but the bandwidth is several thousand times higher, since only a short sampling time per detector element is available. For a 256*256 array and a frame rate of 50 frames/s, 3.3MHz conversion rate is required. The high bandwidth of this method implies that the spectral noise density of the detector element and signal conditioning circuits must be low if an acceptable SNR is to be achieved. Besides the problem of constructing a low-noise high-speed preamplifier and ADC, the detector resistance must be kept low to avoid excessive thermal (Johnson) noise. This will in turn lead to a rapid heating of the detector by the short current or voltage bias pulse required during selection. The rapid temperature increase adds to the signal temperature that is to be detected. If the time from the pulse bias start to sampling of detector temperature is not stable, the captured signal will differ

from sampling to sampling due to the temperature increase. For an acceptable low contribution of such noise, the timing accuracy of the pulse bias and the signal capturing, from selection to selection, must be less than of the order of 1ps. The large bandwidth in combination with long interconnections makes this method also sensitive to noise that is coupled to the selection network and ground references.

3. Columnwise A/D conversion[46]

The readout of the columnwise parallel sensor is a row-to-row principle, where a whole row is selected at a given time. The data of the selected row are columnwise and independently amplified and A/D converted during the time for the row selection. Before a new A/D conversion starts, the digitized data is columnwise read out in parallel into a row of digital registers, so that the previous data can be read out at the same time as the next row is selected during the next conversion. The power available per signal conditioning and ADC branch is the total power available divided by the number of sensor columns. This results in a reasonable power consumption limit on the ADCs. The conversion rate is the frame rate times the number of sensor rows. Compared to the serial concept there are a one level reduction of the analog multiplexing and a bandwidth reduction proportional to the number of sensor columns. This makes the concept considerably less sensitive to noise at the analog signal path. Also, the demand for timing accuracy of the pulse biasing is reduced by the number of sensor columns, since the heating of the detector is not so rapid.

3.4 The Bolometer Material

A key parameter characterizing the material for the bolometric detectors is their thermal coefficient of resistance (TCR). It is defined as

$$TCR = \frac{1}{R_d}\frac{dR_d}{dT} \tag{3.56}$$

where R_d is the material resistance and T is the temperature. According to Eq. 3.43, the array TCR needs to be as large as possible for a given pixel resistance for optimal performance.

There are mainly two different kinds of material presently used in bolometer FPAs. They are amorphous vanadium oxide thin film (VO_x)[32,38,39,52] and amorphous or microcrystalline phases of Si, Ge, and SiGe thin film [43,50,51].

Amorphous vanadium oxide was developed by Honeywell for their microbolometer FPA. It is deposited by an ion beam sputtering process where tight control of film oxygen content is maintained. The VO_x thin film material (in its semiconducting phase) with a resistivity of 0.1Ohm-cm has a TCR of 2%[32]. By changing the film oxygen stoichiometry, the resistivity and TCR can be changed[32, 38,39]. Fig. 3.13 shows a plot of film TCR vs. Film resistivity for 500 and 1000 Angstrom thick films developed by Honeywell. The temperature dependence of resistivity of a semiconductor material, such as VO_x in the semiconducting phase, can be expressed as

$$R_d(T) = R_0 \exp\left(E_A / k_B T \right) \tag{3.57}$$

where E_A is the activation energy, k_B is the Boltzmann constant, and R_0 is the resistance at $T \to \infty$. Combining Eqs. 3.56 and 3.57, one obtains

$$TCR = -\frac{E_A}{k_b T^2} \tag{3.58}$$

Therefore, the individual films of different resistances of Fig. 3.14 can be described by different activation energies over a 100C temperature range around room temperature. The activation energy, which can be derived from the slope of $\ln R_d$ vs 1/T line is shown for one 13.5 Kohms/square VO_x film deposited on Si_3N_4 in Fig. 3.15. The VO_x thin film developed by Honeywell is reported to have very low 1/f noise.

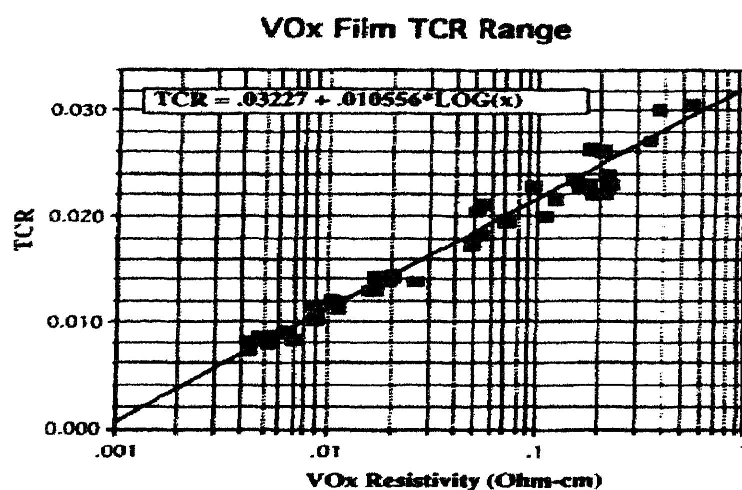

Fig. 3.14 TCR vs VO_x resistivity for vanadium oxide thin film developed by Honeywell. (From [32])

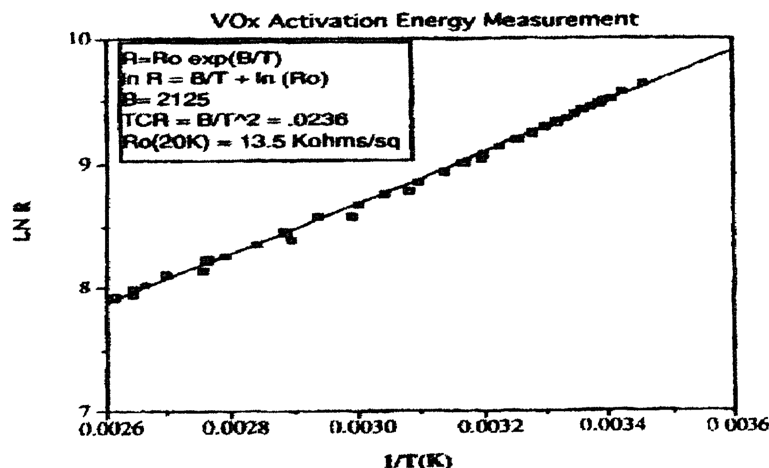

Fig. 3.15 Activation energy analysis for a 500 Angstrom VO_x film of Honeywell. (From [32])

Vanadium dioxide (VO_2) is a metal oxide material. It shows a temperature induced crystallographic transformation that is accompanied by a reversible semiconductor (low-temperature phase) to metal (high-temperature phase) phase transition with a significant change in electrical and optical properties. It's transition temperature is about 68^0C. The semiconductor phase of VO_2 is highly transparent in the 3 to 12um region of the spectrum. In the metallic phase, VO_2 is highly absorbing and reflecting. A plot of resistivity vs. temperature for a dc magnetron sputtered VO_2 on Corning 7059 glass without annealing is shown in Fig. 3.16.

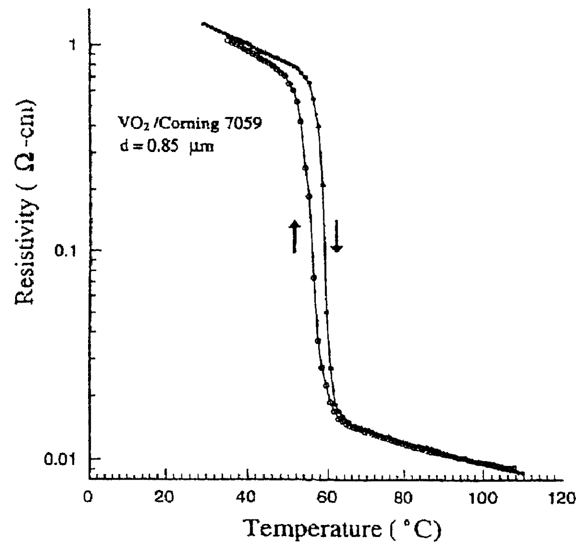

Fig. 3.16 Electrical properties of VO_2 films deposited on Corning 7059 glass. (From [39])

Bolometer material made of Si, Ge, and SiGe thin films in either the amorphous or microcrystalline phase have been studied by Defense Science and Technology Organization (DSTO) of Australia for FPA. These materials have several advantages, including[51]

- A high value for the temperature coefficient of resistance α and therefore a higher value for the responsivity R_V.
- The ability to form a thermally isolated optical cavity from these materials and therefore enhance the emissivity /absorbance of the infrared detecting bolometer.
- Their relatively mature materials growth technologies that are compatible with deposition on a substrate containing the VLSI signal processing functions.
- The ability to select a wide range of bolometer resistance through either the addition of hydrogen or the controlled doping of the material.

The first material studied by DSTO was amorphous silicon. Amorphous silicon possesses a number of properties that make it an attractive material. It has a high temperature coefficient of resistance, $1.8 < -\alpha < 5.5\%\ ^0K^{-1}$ [51], depending on the material growth techniques. Control of a-Si growth is also used to set its resistivity, which increases with increasing $|\alpha|$. The low processing temperature (< 673 K) of a-Si:H enables it to be deposited directly onto VLSI substrates without damage to the underlying circuits. However, the a-Si:H material prepared by DSTO unfortunately exhibits very high values of 1/f noise. Fig. 3.17 shows the measured noise spectra of PECVD deposited and a sputter deposited a-Si:H bolometer produced by DSTO.

The origin of the higher level of noise within PECVD a-SI:H material, as compared with sputtered a-SI:H of similar resistivity, is reportedly the higher hydrogen content within PECVD a-Si:H. In addition, the troublesome RTS noise is commonly found in PECVD material[51].

As a result of the generally higher noise levels within PECVD a-Si:H, work at DSTO was directed towards optimizing the performance of IR detectors based on sputter deposited a-Si:H and a-Si. The detectivity D^* for sputter deposited a-Si:H bolometers decreases as the hydrogen content is increased with the highest detectivity obtained for unhydrogenated material. The degradation in performance with hydrogen is due to several factors. These include the overall increase in material resistivity, and therefore an increase in both Johnson noise and 1/f noise, non-uniformities within the material, such as current filaments through the amorphous microstructure, and instabilities effect within the Si-H microstructure.

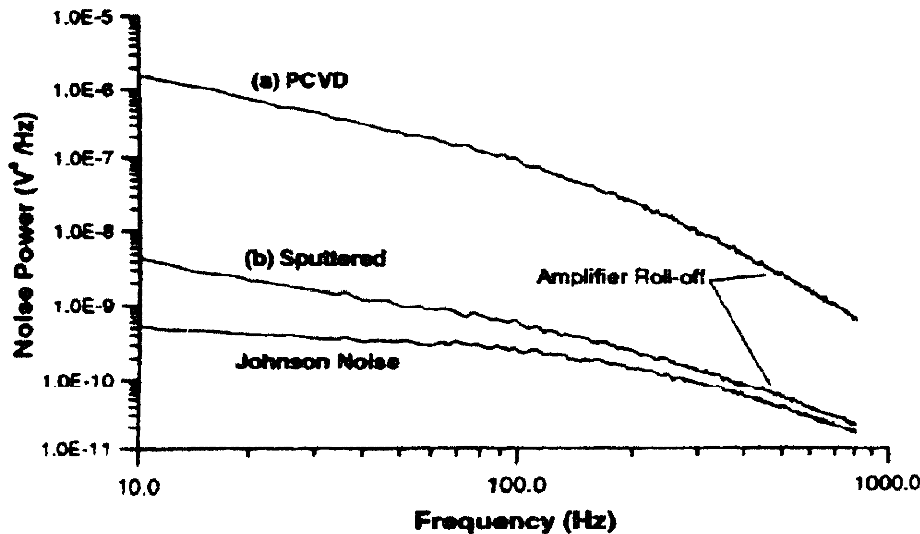

Fig. 3.17 Noise spectra of a-Si:H produced by (a) PECVD and (b) sputter deposition, plus the base Johnson noise. Developed by DSTO. (From [51])

According to Eq. 3.44, the material figure of merit F_{bol} is given by

$$F_{bol} = \frac{\alpha}{R_m^{1/2}}$$

The lower the resistance R_m, the lower the Johnson noise. Therefore, future bolometer materials will probably selected from materials with low resistivity and yet high E_A. Amorphous and microcrystalline phase of Ge, and SiGe thin film are studied DSTO. A result is shown in Table 3.1.

Table 3.1 Properties and detectivity measured for semiconductor film bolometers operating in a vacuum. The current is varied to maximize for detectivity.

Detector Material	Detector Size (um)	α $\%K^{-1}$	Resistance $(K\Omega)$	$D^*(cmHz^{1/2}W^{-1})$ @30 Hz	$D^*(cmHz^{1/2}W^{-1})$ @80 Hz
PECVD a-Si:H	40*40	-4.5	1550	$1.7*10^7$	$1.15*10^7$
Sputtered a-Si:H	40*40	-2.1	1740	$1.6*10^8$	$1.08*10^8$
Sputtered a-Si	70*70	-1.8	22	$3.2*10^8$	$2.2*10^8$
Sputtered a-Ge	70*70	-1.8	1.4	$4.7*10^8$	$3.2*10^8$

3.5 Monolithic Resistive Bolometer Arrays Developed by Honeywell[28,31-39]

The thermal isolation structure developed by Honeywell is shown in Fig. 3.4 of section 3.2. In the Honeywell structure, the optical resonator is optimized for high IR absorption by using an air gap between the suspended microbridge and substrate. The spacing between the microbridge and the substrate would be about 2.5um. In contrast, the optical resonator developed by DSTO uses an a-Si:H layer sandwiched between two metal layers.

The thermal sensing material of the Honeywell bolometer is a vanadium oxide thin film whose TCR varies by $\pm 0.1\%$ over an array[34]. The resistivity of the thin film over the same area varies by $\pm 1\%$. An important characteristic is that its 1/f noise contributes negligibly to the total noise at the operating current of 250uA[28].

The Honeywell's uncooled microbolometer FPA does not require a chopper which has the following significant advantages[17]:

- the mechanical chopper part is eliminated, increasing reliability and maintainability,
- the *NETD* is improved by a factor of 2,
- size, weight, and power consumption are reduced.

The sensor *NETD* is improved by a factor of 2 because: 1) the thermal radiation signal is not blocked on every other frame basis (see Fig. 3.18) giving a $\sqrt{2}$ improvement in responsivity; and 2) the sensor internal frame rate is also reduced by a factor of 2, to 30 Hz, giving an additional $\sqrt{2}$ improvement.

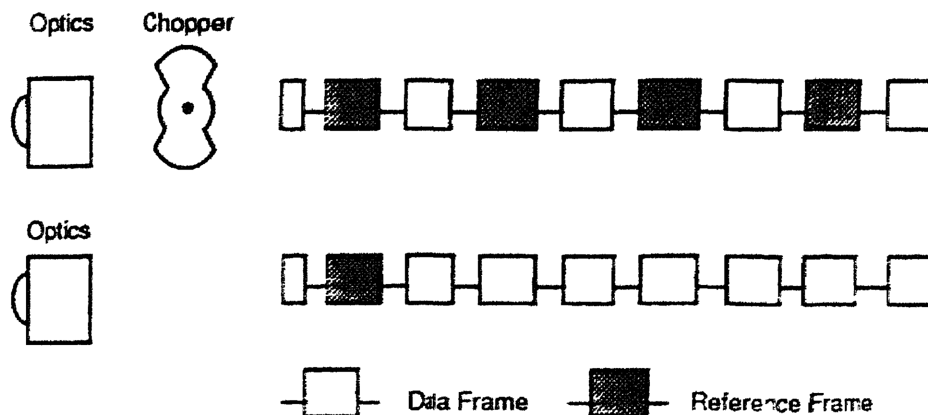

Fig. 3.18 The chopperless operation concept provides a 2* *NETD* improvement, as well as increased reliability, smaller size, less weight, and less power. (From [17])

Since an offset correction must still be performed to remove built-in "pedestal" signals due to pixel-to-pixel impedance non-uniformity, a reference scene is provided to enable pedestal subtraction. In a practical system, this reference scene would be obtained by blocking the radiation with an iris or lens cap, for example, for about 1 sec, while

capturing, averaging, and storing a reference frame in a frame memory. Once the average reference frame has been stored, the camera is then allowed to stare continuously at the scene without a chopper, and image frames are offset-corrected by subtraction from the stored reference frame.

The block diagram of a Honeywell uncooled IR imager is shown in Fig. 3.19. Bias supplies for the microbolometers are directed through decoding circuits under control of the array-scanning logic. The multiplexer on the array chip allows random addressing of each pixel in the array. The rows in the array are arranged into 16 row groups, with 15 rows in each group. The columns are organized into 24 column groups of 14 columns each for readout. Each column in a column group connects to one channel of output, and the camera reads out 14 channels at once. The array addresses one row and one column group at any given instant, then moves to the next column group on the same row. All pixels on the same row are read out before the pixels on the next row. At 30 frames a second, each pixel has a readout time of 5 us. A typical array consumes 40 mW during normal operation[28].

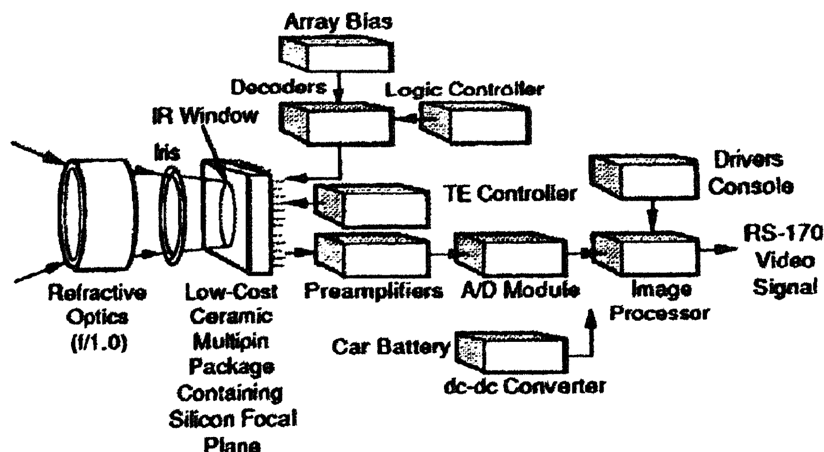

Fig. 3.19 The block diagram of Honeywell's uncooled IR imager. (From [28])

The summary of Honeywell's microbolometer arrays is [15]

- Unique thermal-isolation structure results in highest possible sensitivity for uncooled bolometric sensors
- Room temperature, 8-12 um operation
- Monolithic silicon process line
- Extremely rugged
- Chopperless operation
- No measurable crosstalk
- 240*336 pixel arrays, 2-mil pixel demonstrated
- Measured *NETD* 0.04K (f/1.0)

Table 3.2 A summary of the parameters of Honeywell's microbolometer arrays

Parameter	Typical	Anticipated Improvement	Latest Report[36]
Mass (silicon nitride)	$1*10^{-9}$ gm		
Thermal Mass	$1*10^{-9}$ J/C		$2*10^{-9}$ J/C
Thermal Conductance to Substrate	$1*10^{-7}$ W/C	$<1*10^{-7}$ W/C	$1.7*10^{-7}$ W/C
Thermal Response Time	10 ms		12ms
Operating Temperature	Room Temperature		
Vacuum	<100 mTorr		
Fill-Factor	50%	75-85%	48%
Shock Tolerance	>20,000 G		
Absorption(8-14 um band)	80%		80%
pixel Size	2*2 mil	1*1 to 3*3 mil	$46.25*46.25\,um^2$
bias Voltage	1.5 V		
Resistance	5 kΩ		15 kΩ
TCR	2%/C	2.5% to 3%/C	
Responsivity	70,000 V/W	250,000 V/W	
Noise	10uV rms	5 uV rms	
Sensitivity(NETD)	0.1C	0.015C	0.04K
Array Dimensions	240*336 Pixels	Larger	245*327
Dead Pixels	<25 per Array	0 per Array	
Uniformity	2% per Pixel		

3.6 Monolithic Resistive Bolometer Arrays Developed by Defense Science and Technology Organization [30, 40-50]

Very interesting uncooled thermal imager technology is now under development at the Defense Science and Technology Organization (DSTO) of Australia. The reports on this work have provided the author with a good background on the fundamentals of bolometer FPA. The origin of research conducted during the 1970s aimed at optimizing the performance of thin film bolometer detectors[43]. The first product of this research was a metal film bolometer (MFB) detector[40] with a typical D* of $1*10^8\ cm.Hz^{1/2}.W^{-1}$ and a time constant of 0.2 ms. DSTO is currently engaged in the preparation of experimental arrays for lightweight thermal imaging and integrating thin-film monolithic detector arrays with sub-micron CMOS signal conditioning and readout microelectronics[46-48]. The analog-to-digital conversion and some signal processing functions will be incorporated on the array chip or within the same package, and the remaining electronics will be in the form of application specific integrated circuits (ASICs) mounted with the array on a single circuit card.

The thermal isolation structure developed by DSTO is described in section 3.2 and shown in Fig. 3.5. The best total thermal conductance in vacuum reported for focal plane array is $4.8*10^{-7} Watts/K$ [50].

The thermal sensing material of DSTO's bolometer is described in material section. Particular attention is given to materials and material growth techniques that maximize the responsivity and minimize the electronic excess noise[51].

DSTO is now developing the analog-to-digital conversion and signal processing circuits for their FPA[46-50]. They are also studying new materials to reduce the 1/f noise

and Johnson noise[50]. Expected performance and characteristics of a 256*256 sensor array are shown in Table 3.3[46].

Table 3.3 Expected performance and characteristics of a 256*256 sensor array

On-Chip ADC Resolution	16 bit
Spatial Resolution	256*256
NETD	0.2K
Frame Rate	50 frames/s
Detector Size	40*40 um^2
Readout electronics Chip Area	10.2*2.3 mm^2
Power Consumption	0.17 W
Power supply voltage	5 V
VLSI Process	0.8 um Digital CMOS

CHAPTER 4

REVIEW OF THE THEORY AND PERFORMANCE OF PYROELECTRIC AND FERROELECTRIC UNCOOLED FOCAL PLANE ARRAYS

4.1 Pyroelectric Response

The pyroelectric effect is described by the

$$P_i = p_i \Delta T \tag{4.1}$$

where P_i, a vector, is the polarization change due to a change in temperature ΔT times the pyroelectric coefficient p_i. For infinitesimal changes in temperature, Eq. 4.1 can be written in the differential form

$$\frac{\partial P_i}{\partial T} = p_i \tag{4.2}$$

The effect of a temperature change on a pyroelectric material is to cause a displacement current i_P to flow in an external circuit (see Fig. 4.1), such that

$$i_P = A_{pixel} \cdot p' \cdot \frac{dT}{dt} \tag{4.3}$$

where A_{pixel} is the electrode area of the material, p' is the component of the pyroelectric coefficient normal to the electrodes and dT/dt is the rate of change of temperature with time.

The pyroelectric element can be represented by a current source, $A_{pixel} \cdot p' \cdot \frac{dT}{dt}$, driving a parallel element-load impedance as shown in Fig. 4.2. Let C_d and R_d be the capacitance and resistance of the pyroelectric element, and C_L and R_L be the load capacitance and resistance e.g. of the preamplifier). Thus, the parallel element-load

capacitance C_E and resistance R_E are, $C_E = C_d + C_L$, $R_E^{-1} = G_E = R_d^{-1} + R_L^{-1}$ where G_E is the electrical conductance. The admittance of the circuit is $Y = G_E + i\omega C_E$.

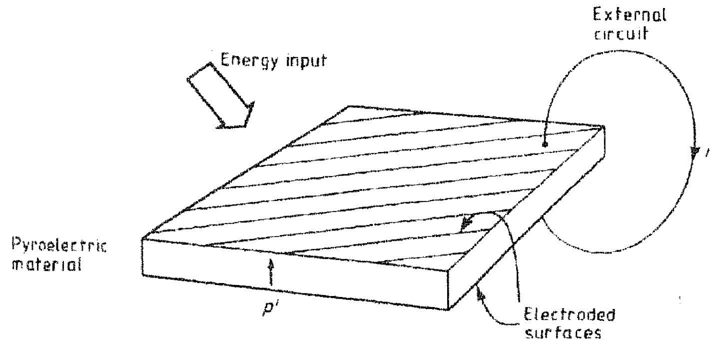

Fig. 4.1 Schematic diagram of a pyroelectric element subject to a small temperature change.

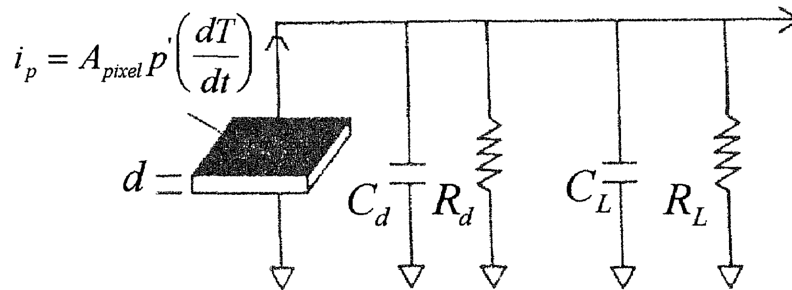

Fig. 4.2 Equivalent circuit of a pyroelectric element.

The temperature difference T between the detector element and its surroundings when illuminated by a flux of radiation with power $W(t)$ modulated at frequency ω such that $W(t) = W_0 e^{i\omega t}$ can be described by

$$\eta W(t) = \frac{C_{th} dT}{dt} + K_{th} T \tag{4.4}$$

where η is the fraction of incident power absorbed by the detector, C_{th} is the detector thermal capacitance, and K_{th} is the total thermal conductance to surroundings.

Eq. 4.4 has the solution

$$T(t) = \frac{\eta W(t)}{(K_{th} + j\omega C_{th})} \tag{4.5}$$

Thus, from Eq. 4.3, the pyroelectric current i_P is

$$i_P = A_{pixel} p' \left(\frac{dT}{dt} \right) = \frac{j\eta\omega p' A_{pixel} W(t)}{(K_{th} + j\omega C_{th})} \tag{4.6}$$

The current responsivity R_i is defined as the pyroelectric current per unit incident power, therefore

$$R_i = \left| \frac{i_P(t)}{W(t)} \right| = \frac{\eta\omega p' A_{pixel}}{(K_{th}^2 + \omega^2 C_{th}^2)^{1/2}} \tag{4.7}$$

At low frequencies ($\omega\tau_{th} << 1$), the current responsivity R_i is proportional to ω, being

$$R_i = \frac{\eta A_{pixel} p' \omega}{K_{th}} \tag{4.8}$$

For frequencies much higher than τ_{th}^{-1}, R_i is nearly constant, being

$$R_i = \frac{\eta A_{pixel} p'}{C_{th}} = \frac{\eta p'}{c'd} \tag{4.9}$$

where c' is the volume specific heat and d is the thickness.

The pyroelectric voltage (V_p) of the detector shown in Fig. 4.2 is simply derived from the pyroelectric current and the electrical admittance (Y) presented to i_p. Therefore,

$$V_p = \frac{i_p}{Y} = \frac{j\eta\omega p' A_{pixel} W(t)}{(K_{th} + j\omega C_{th})(G_E + j\omega C_E)} \tag{4.10}$$

and the voltage responsivity R_V is

$$R_V = \left|\frac{V_p}{W(t)}\right| = \frac{\eta\omega p' A_{pixel}}{K_{th} G_E (1+\omega^2\tau_{th}^2)^{1/2}(1+\omega^2\tau_E^2)^{1/2}} \tag{4.11}$$

where $\tau_{th} = \frac{C_{th}}{K_{th}}$ and $\tau_E = \frac{C_E}{G_E}$ are the thermal and electrical time constants respectively. The form of the voltage responsivity is shown in Fig. 4.3 for $\tau_E > \tau_{th}$. R_V is a maximum at $\omega = (\tau_E \tau_{th})^{-1/2}$ with

$$R_{V(\max)} = \frac{\eta p' A_{pixel}}{K_{th} G_E (\tau_{th} + \tau_E)} \tag{4.12}$$

At low frequency $(\omega\tau_{th} << 1)$, R_V is proportional to frequency. For high frequency $(\omega\tau_{th} >> 1; \omega\tau_E >> 1)$, R_V is given by

$$R_V = \frac{\eta p'}{c' d (C_d + C_L)\omega} \tag{4.13}$$

If the element capacitance, C_d, is large compared with C_L, then Eq. 4.13 reduces to

$$R_V = \frac{\eta p'}{c' \varepsilon_r \varepsilon_0 A_{pixel} \omega} \tag{4.14}$$

where ε_0 is the permittivity of free space and ε_r is the relative permittivity of the pyroelectric material. For such a detector, the response is proportional to a figure of merit F_V

$$F_V = \frac{p'}{c' \varepsilon_r \varepsilon_0} \tag{4.15}$$

If $C_L >> C_d$, then Eq. 4.13 reduces to

$$R_V = \frac{\eta p'}{c' d \omega C_L} \tag{4.16}$$

The voltage response is proportional to

$$F_i = \frac{p'}{c'} \tag{4.17}$$

which is a different material figure of merit.

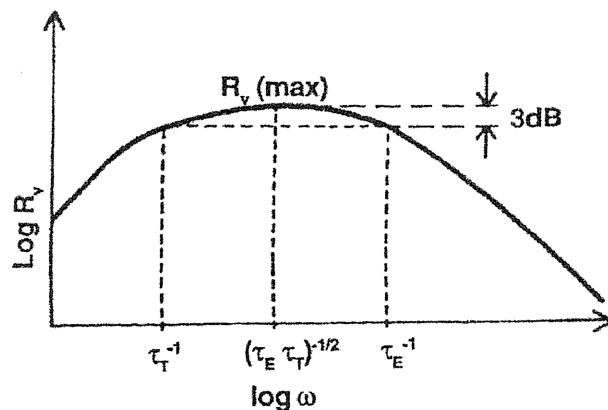

Fig. 4.3 Frequency variation of voltage responsivity.

For a focal plane array, the pixel area (A_{pixel}) in the above equations should be replaced by effective area (A_{eff}), which is the pixel area with pyroelectric material.

Any real device implementation includes circuit elements that introduce parasitic capacitance. This results in a responsivity attenuation factor of

$$A_s = \frac{C_d}{C_d + C_P} \tag{4.18}$$

where C_d is the detector capacitance and C_P is the parasitic capacitance. This effect is especially important when the parasitic capacitance is high, such as for arrays addressed by only a switch at each pixel site. The parasitic capacitance can be reduced by using a preamplifier or buffer at each pixel to decouple the detector capacitance from the large

address line parasitic capacitance. When the pixel area reduces, the effect becomes more serious.

The three main research areas of pyroelectric focal plane arrays are the hybrid or monolithic thermal structure, the design of the silicon readout integrated circuit, and the ferroelectric material. They are discussed in the following sections.

4.2 Hybrid and Monolithic Thermal Structures

Fig. 4.4 shows a 2-dimensional hybrid detector array together with the other components required for an imaging sensor. The focused radiation from the IR lens is first chopped and then falls on the hybrid device in the center of the diagram. The ferroelectric detector wafer at the left of the hybrid has an array of metallic electrodes deposited on its lower surface to define the detector elements. In the hybrid processing, the electrodes are bonded, by using solder bumps, to corresponding pads on the silicon multiplexer chip shown at the right of the hybrid. The chopped radiation produces alternate warming and cooling of the array and this results in alternate positive and negative signals.

Fig. 4.5 shows the structure of a single element and its neighbors. Element pitch is about 50um. The ferroelectric material is the wafer from the hot pressed ceramic block, polished to proper thickness. Radiation is incident from the top, and is absorbed in an impedance matched thin film structure, with a thin resistive (377Ω per square) metallic film, a $\lambda/4$ polymer layer and a $10-20\Omega$ per square metallic film as a back reflector which also provides the common electrical contact. Average absorption in the 8 to 14um band of over 90% can be achieved.

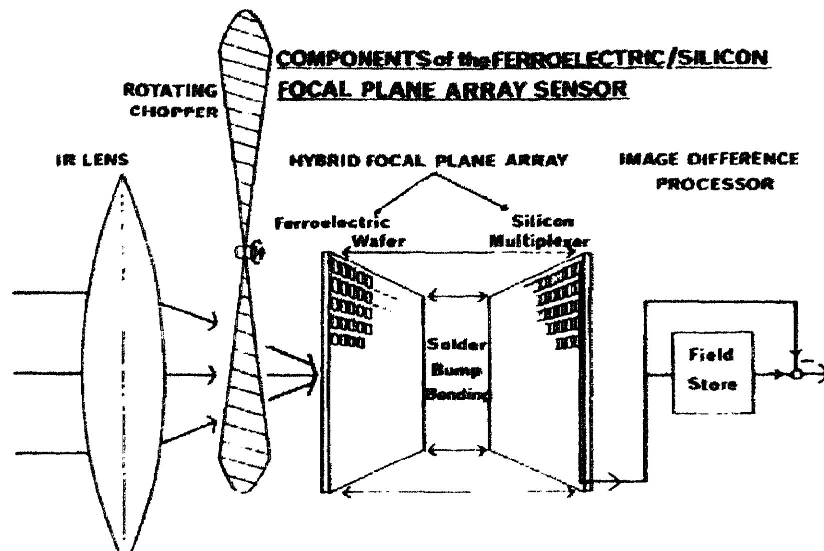

Fig. 4.4 The ferroelectric hybrid array and its use in an IR sensor head. (From [56])

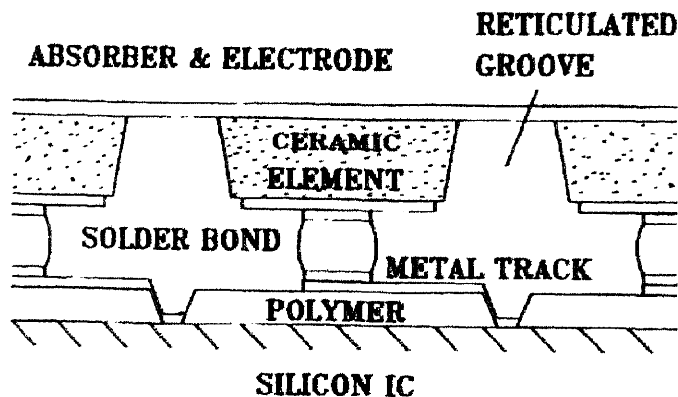

Fig. 4.5 Low thermal conductance structure for a hybrid array element. (From [56])

The geometry of the ferroelectric element illustrates the thermal design feature of isolation within the structure. Three measures are used: firstly the solder bond is kept to as small an area as possible, and secondly the bond is made to a thin interconnection track on a thick insulating polymide layer on the silicon IC. Thirdly, to isolate the individual

detector element from its neighbors, grooves or slots are milled into the ceramic wafer in a process knows as reticulation. Without this physical separation, heat would spread laterally between the elements reducing the image resolution.

The present successful ferroelectric arrays use a hybrid construction, but fully integrated technologies where the detector material is directly deposited on the silicon IC are also being researched. Potential advantages of integrated designs are [56]

- no detector wafer processing required,
- no solder bonding process required,
- no reticulation required,
- wafer scale processing for fully completed devices,
- increased performance from lower thermal conductance in micro-structures on the IC.

The first four offer reduced complexity in processing, i.e. higher yield, and lower cost, while the last has potential for marked improvements in sensitivity.

The two main aspects for integrated array research are directly deposited thin films of the detector material and thermally insulating micro-structures built on the silicon IC. The material performance will be discussed in the material section. The microbridge structure scheme is the same as the structure for microbolometer detector. The pyroelectric materials are deposited on the SiO_2 / Si_3N_4 microbridge which is supported over an air gap over the silicon substrate by legs which carry the electrical contacts to the top and bottom electrodes of the element.

4.3 Low Noise Readout Design and Circuitry

The primary noise sources for a typical pyroelectric focal plane array are listed below[57]

1. The fundamental or limiting thermal noise seen as temperature fluctuations in the detector.
2. The noise terms associated with the ferroelectric material, that is the dielectric loss and the spurious piezoelectric or microphony noise.
3. The noise terms due to the silicon readout circuit. The magnitude of these terms depend on the preamplifier and multiplexer designs. An important feature is that these designs will also determine the device noise bandwidth.
4. The spatial or fixed pattern noise: this depends on the ferroelectric material through the variation of the responsivity over the whole detector array, and also depends on the readout circuit through variation of voltage offsets and gain. The spatial noise variation can be very critical in large array performance, since it is often larger than the signal itself. To completely compensate for noise variation excessive demands would require the digital processing following the array. Therefore, most of the offset noise is removed using a chopper and an image difference process (IDP) which will be discussed in this section.

A pyroelectric detector circuit is shown in Fig. 4.6.

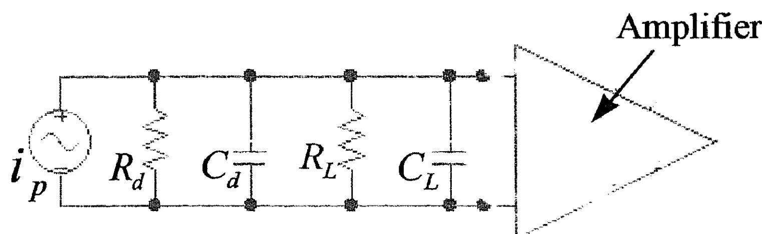

Fig 4.6 A pyroelectric detector circuit.

The noise equivalent circuit of Fig. 4.6 is shown in Fig. 4.7.

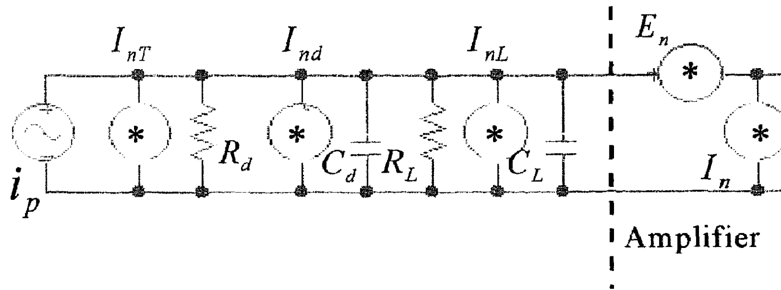

Fig. 4.7 The noise equivalent circuit of Fig. 4.6.

where

i_p: pyroelectric current,

I_{nT} : temperature fluctuation current,

R_d : resistance of a pyroelectric element,

I_{nd}: Johnson noise current of R_d,

C_d: capacitance of a pyroelectric element,

R_L : load resistance,

I_{nL}: Johnson noise current of R_L,

E_n : equivalent noise voltage of amplifier,

I_n : equivalent noise current of amplifier.

Fig. 4.8 shows the equivalent noise voltage of Fig. 4.7.

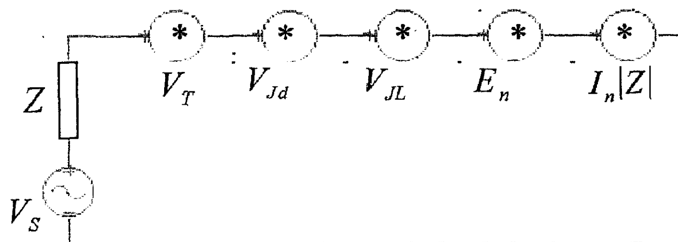

Fig. 4.8 Equivalent noise voltage of Fig. 4.7.

where

V_S : signal voltage,

V_T : temperature fluctuation noise voltage,

V_{Jd} : Johnson noise voltage of R_d,

V_{JL} : Johnson noise voltage of R_L,

$Z = (R_L // R_d // C_d // C_L)$.

The equivalent input noise voltage E_{Si} is

$$E_{Si} = \left(V_T^2 + V_{Jd}^2 + V_{JL}^2 + E_n^2 + I_n^2 |Z|^2\right)^{1/2} \tag{4.19}$$

1. Temperature fluctuation noise

The rms value of the temperature fluctuation spectrum, derived in appendix A, is

$$\Delta W_T = (4k_B T^2 K_{th})^{1/2} \quad (W / Hz^{1/2}) \tag{4.20}$$

The temperature noise voltage is calculated by treating ΔW_T in the same way as an incoming signal. Hence,

$$V_T = \left(\frac{R_V}{\eta}\right)(4k_B T^2 K_{th})^{1/2} \quad (V / Hz^{1/2}) \tag{4.21}$$

2. Johnson noise

The complex permittivity ε_C of a dielectric material is [58]

$$\begin{aligned} \varepsilon_C &= \varepsilon_0 \varepsilon_r + \frac{\sigma}{j\omega} \\ &= \varepsilon' - j\varepsilon'' \end{aligned} \tag{4.22}$$

where ε' is the dc permittivity of the dielectric material and σ is its ac conductivity. The ratio $\frac{\varepsilon''}{\varepsilon'}$ measures the magnitude of the conduction current relative to that of the displacement current. It is called a loss tangent, $\tan\delta$, because it is a measure of the ohmic loss in the medium.

$$\tan\delta = \frac{\varepsilon''}{\varepsilon'} = \frac{\sigma}{\omega\varepsilon_0\varepsilon_r} = \frac{R_d^{-1}}{\omega C_d} \tag{4.23}$$

Hence,

$$V_{Jd} = \left(\frac{4k_B T}{R_d}\right)^{1/2} * |Z|$$
$$= \frac{\left(4k_B T\omega C_d \tan\delta\right)^{1/2}}{\left(G_E^2 + \omega^2 C_E^2\right)^{1/2}} \quad (V / Hz^{1/2}) \tag{4.24}$$

and,

$$V_{JL} = \left(\frac{4k_B T}{R_L}\right)^{1/2} * |Z|$$
$$= \frac{\left(4k_B T\right)^{1/2}}{R_L^{1/2}\left(G_E^2 + \omega^2 C_E^2\right)^{1/2}} \quad (V / Hz^{1/2}) \tag{4.25}$$

If $R_d^{-1} << R_L^{-1}$, that is $\omega C_d \tan\delta << R_L^{-1}$ or $\omega << (R_L C_d \tan\delta)^{-1} = \omega_l$, then V_{JL} is the dominant Johnson noise, and

$$V_J = \left(V_{JL}^2 + V_{Jd}^2\right)^{1/2} \cong V_{JL}$$
$$\cong \left(\frac{4k_B T R_L}{1 + \omega^2\tau_E^2}\right)^{1/2} \quad (V / Hz^{1/2}) \tag{4.26}$$

This results in an ω^{-1} dependence of V_J at frequencies $\omega > \tau_E^{-1}$.

If $R_d^{-1} >> R_L^{-1}$, that is $\omega C_d \tan\delta >> R_L^{-1}$ or $\omega >> \omega_l$, the Johnson noise generated by the ac conductance of the detector element will dominate, so that

$$V_J \cong V_{Jd} \cong \left(\frac{4k_B T R_d}{1+\omega^2 \tau_E^2} \right)^{1/2}$$

$$\cong \left(\frac{4k_B T \tan\delta}{C_E \omega} \right)^{1/2} \text{ for } C_d >> C_L \qquad (4.27)$$

Johnson noise frequently dominates in pyroelectric detectors. The consequence of this is that at frequencies greater than τ_E^{-1} and ω_t, the specific detectivity D^* is (from Eqs. 4.14 and 4.27)

$$D^* = \frac{R_V A_{pixel}^{1/2}}{V_J} = \frac{\eta p'}{(4k_B T)^{1/2} d^{1/2} c'(\varepsilon_r \varepsilon_0 \tan\delta)^{1/2} \omega^{1/2}} \qquad (4.28)$$

Thus, to maximize the D^* in this region it is desirable to maximize F_D

$$F_D = \frac{p'}{c'(\varepsilon_r \varepsilon_0 \tan\delta)^{1/2}} \qquad (4.29)$$

which is regarded as the third figure of merit for pyroelectric materials. For frequencies below ω_t, or if one of the other noise sources is dominate, then maximizing F_V in Eq. 4.15 will maximize the detectivity.

3. Amplifier noise

The two noise sources of a MOSFET amplifier are current noise I_n and voltage noise E_n. They are given by [20]

$$I_n = \left(2qI_{GSS}\right)^{1/2} \ (A / Hz^{1/2}) \qquad (4.30)$$

and

$$E_n = \left(\frac{8k_B T}{3g_m} + \frac{K_F I_{Dq}^{AF}}{g_m^2 f C_{OX} L_{eff}^2} \right)^{1/2}$$

$$= \left(V_a^2 + \frac{Z_a^2}{f} \right)^{1/2} \quad (V / Hz^{1/2}) \tag{4.31}$$

where q is the electronic charge, I_{GSS} is the gate leakage current of a MOSFET, g_m is the transconductance of a MOSFET, C_{OX} is the gate oxide capacitance, L_{eff} is the effective channel length, K_F is the flicker noise coefficient, A_F is a constant, I_{DQ} is the quiescent drain current, and f is the frequency of operation.

From Eq. 4.19, the amplifier noise voltage V_A is

$$\begin{aligned} V_A &= \left(E_n^2 + I_n^2 |Z|^2 \right)^{1/2} \\ &= \left(E_n^2 + \frac{I_n^2 R_E^2}{1 + \omega^2 \tau_E^2} \right)^{1/2} \quad (V / Hz^{1/2}) \end{aligned} \tag{4.32}$$

The expressions for the individual noise sources are listed below:

Temperature fluctuation noise : $V_T = \left(\frac{R_V}{\eta} \right) (4 k_B T^2 K_{th})^{1/2} \quad (V / Hz^{1/2})$

Dielectric loss noise :

$$\begin{aligned} V_{Jd} &= \frac{\left(4 k_B T \omega C_d \tan \delta \right)^{1/2}}{\left(G_E^2 + \omega^2 C_E^2 \right)^{1/2}} \quad (V / Hz^{1/2}) \\ &\cong \left(\frac{4 k_B T \tan \delta}{C_E \omega} \right)^{1/2} \quad \text{if } \omega >> \omega_t \end{aligned}$$

Johnson noise of R_L :

$$\begin{aligned} V_{JL} &= \frac{\left(4 k_B T \right)^{1/2}}{R_L^{1/2} \left(G_E^2 + \omega^2 C_E^2 \right)^{1/2}} \quad (V / Hz^{1/2}) \\ &\cong \left(\frac{4 k_B T R_L}{1 + \omega^2 \tau_E^2} \right)^{1/2} \quad \text{if } \omega << \omega_t \end{aligned}$$

Amplifier voltage noise :

$$E_n = \left(V_a^2 + \frac{Z_a^2}{f} \right)^{1/2} \quad (V / Hz^{1/2})$$

Amplifier current noise: $$I_n|Z| = \left(\frac{2qI_{GSS}R_E^2}{1+\omega^2\tau_E^2} \right)^{1/2} \quad (V/Hz^{1/2})$$

Using the above derived equations, the frequency dependence of the various noise sources was calculated using the following reasonable values for a detector using the pyroelectric material, $(BaSr)TiO_3$.

Assuming

$K_{th} = 5*10^{-6}(W/^0K)$ (Thermal conductance),

$C_{th} = 7.5*10^{-8}(J/^0K)$ (Thermal capacitance),

$\eta = 0.8$ (Absorber efficiency),

$A_{eff} = 35*35(um^2)$ (Effective area),

$T = 300(^0K)$ (Substrate temperature),

$d = 25um$ (Pixel thickness),

$I_n = 1.8*10^{-16}(A/Hz^{1/2})$ (Amplifier current noise),

$V_a = 3.4*10^{-9}(V/Hz^{1/2})$,

$Z_a = 2.4*10^{-7}(V)$,

$k_B = 1.38*10^{-23}(W.S/^0K)$ (Boltzmann's constant)

$C_p = 3pF$.

$(BaSr)TiO_3$ material properties:

$\tan\delta = 4*10^{-3}$ (Loss $\tan\delta$),

$p' = 0.7uC/cm^2K$ (Pyroelectric coefficient),

$\varepsilon_r = 8000$ (Dielectric constant).

The results are given in Fig. 4.9. An important feature is that all the sources produce noise which decreases with frequency except the g_m noise V_a in E_n. The 1/f amplifier noise falls as its name implies, but the dielectric loss noise, the amplifier current noise and the thermal fluctuation noise all fall because they are shunted by the detector capacitance. The one noise that is not shunted and is therefore flat is g_m noise. A major advantage of the capacitative ferroelectric detectors is that the detector element acts as its own filter, and therefore, a low equivalent noise bandwidth can be achieved for these noise sources.

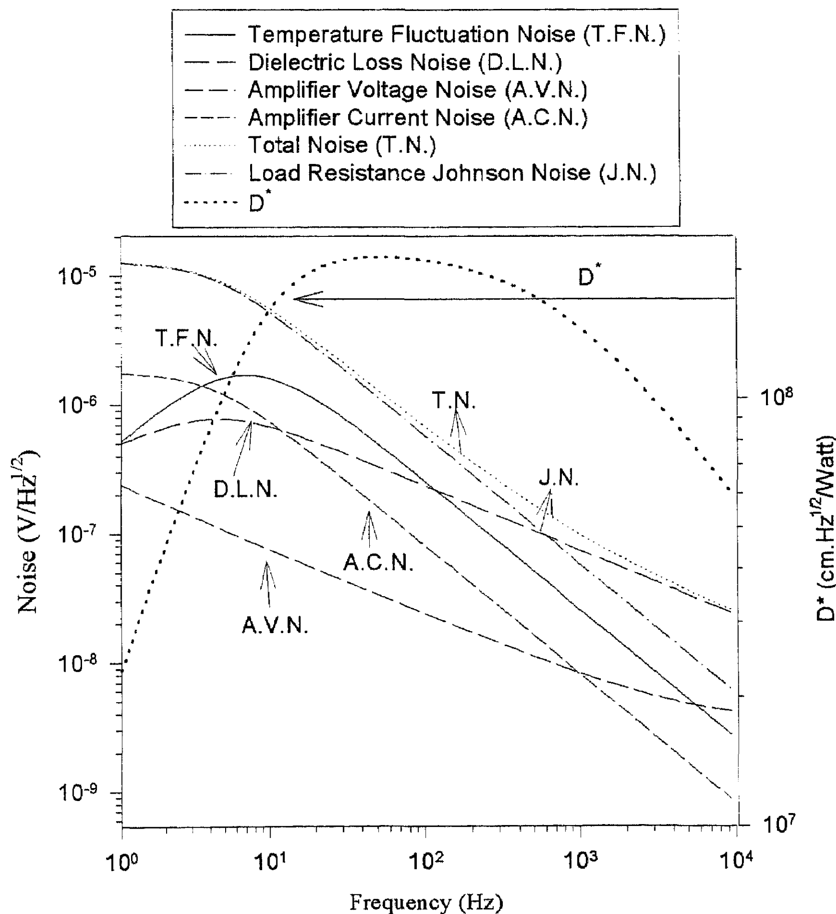

Fig. 4.9 Noise sources for a $(BaSr)TiO_3$ ferroelectric element and their frequency dependence.

Spatial noise levels, because of offset and responsivity variations, are often larger than the signal itself, leading to excessive demands on the digital processing following the array. These noise can be removed using a image difference processing (IDP) which is described as follows.

IDP is used with pyroelectric arrays in which the incident radiation is chopped at the frame rate, ie one field open to the radiation and the next closed. The square-wave chopped radiation on a element from a static scene is shown in Fig. 4.10, which also shows the temperature variation of the element. The field time (τ_f) is smaller than the thermal time constant (τ_{th}), and the temperature rises and falls as the element is alternately exposed and shuttered. The signal from each element is sampled at the end of every open and closed chopper field. The closed field signals are subtracted from the previous open field signals. This is shown in Fig. 4.11. The IDP output has been stripped of the offset voltages which vary from element to element and introduce fixed pattern noise.

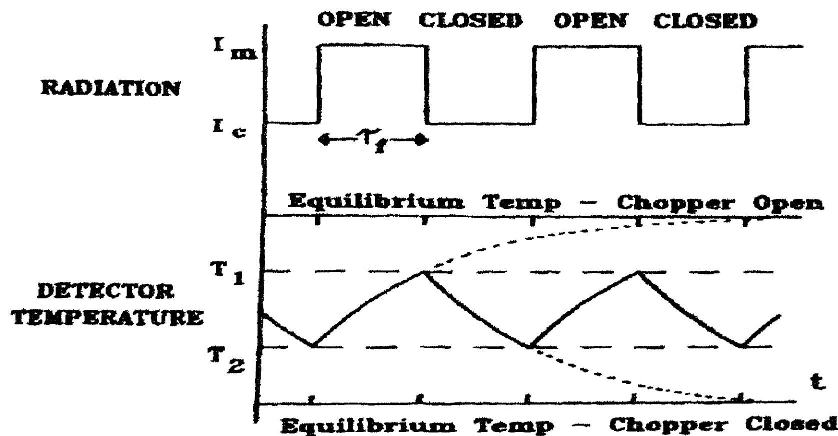

Fig. 4.10 Chopped radiation and detector element temperature. (From [59])

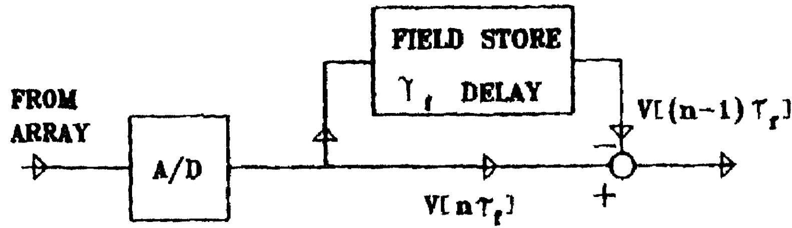

Fig. 4.11 Field image difference processing digital filter. (From [59])

The image difference processing also adds a filter to the signal and noise data path. Let $V_r \sin 2\pi ft$ be a general noise component at frequency f for the element number r, at its interface with the buffer amplifier. Then the result of passing noise samples at chopping frequency f_C through the filter is

$$V(noise) = V_2 - V_1$$

$$= V_r\{\sin[2\pi nf / f_C] - \sin[2\pi(n-1)f / f_C]\}$$

$$= 2V_r \sin[\pi f / f_C]\cos[2\pi(n-\tfrac{1}{2})f / f_C] \qquad (4.33)$$

The filter transfer function is

$$H(f) = 2\sin(\pi f / f_C) \qquad (4.34)$$

The benefits of IDP for the performance of chopped pyroelectric imaging sensors are

1. removal of fixed pattern noise,
2. low frequency noise filtering.

4.4 Pyroelectric Materials[54]

The two modes for infrared detection by the ferroelectric material are described in Fig. 4.12. The typical properties of a second order ferroelectric are plotted here against

temperature. It can be seen that the spontaneous polarization P_0 falls to zero at the transition temperature (Curie temperature) and the relative permittivity rises to a peak in the region of the transition. The conventional pyroelectric mode for IR detection at the left, utilizes the falling spontaneous polarization with increasing temperature. The radiation induced change in the detector temperature results in a change of polarization equivalent to the flow of a surface charge. However a second mode is available which instead utilizes the change of permittivity with temperature in the region of the ferroelectric phase transition. In this mode, the detector operates with an applied bias that charges the element. Heat due to the absorption of incident radiation results in an increment of permittivity and hence a signal voltage. This mode is often described as dielectric bolometer operation. Since the aim is to operate detectors at temperatures close to ambient, an immediate point is that whereas for conventional pyroelectric operation, T_C should be well above ambient, for dielectric operation T_C should be close to or below ambient. Therefore different materials will be required for the two modes.

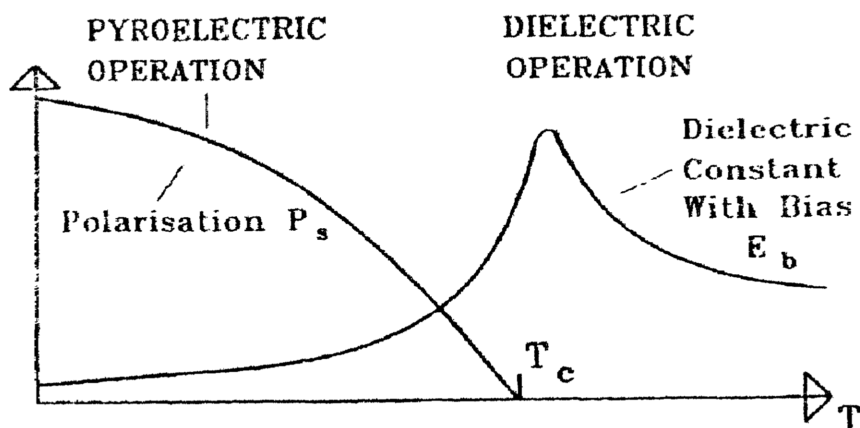

Fig. 4.12 Operating modes for ferroelectric materials as infrared detectors. (From [57])

The generalized pyroelectric coefficient, p', is the temperature differential of the displacement, $p' = dD/dT$. The displacement can be written

$$D = P_0 + \varepsilon_0 \int_0^E \varepsilon_r(E).dE \qquad (4.35)$$

so that

$$p' = \frac{dP_0}{dT} + \varepsilon_0 \int_0^E \left(\frac{\partial \varepsilon_r(E)}{\partial T} \right)_E .dE \qquad (4.36)$$

P_0 is the spontaneous polarization and $p' = dP_0/dT$ is the conventional pyroelectric coefficient in zero applied field below the transition. Above the transition temperature T_C, P_0 is zero and the coefficient is often referred to as the induced pyroelectric coefficient since it falls to zero in the absence of an applied field.

Ignoring any leakage of charge through the element itself and the input load capacitance, the signal voltage would be

$$\Delta V = \frac{\Delta Q}{C_d} = \frac{p' A_d \Delta T}{C_d}$$
$$= \left\{ \left(\frac{d}{\varepsilon_r(E)\varepsilon_0} \right) \cdot \left(\frac{dP_0}{dT} \right) + \frac{1}{\varepsilon_r(E)} \int_0^{V_b} \left(\frac{\partial \varepsilon_r(E)}{dT} \right) .dV \right\} \Delta T \qquad (4.37)$$

where ΔQ is the charge generated and ΔT is the temperature change.

The first term is the conventional pyroelectric voltage with wafer thickness d, and the second term is the dielectric effect under the applied detector bias, V_b. For the dielectric term, it would appear that very high signal voltages are possible by simply increasing the applied voltage. However this is not so; in the non-linear behavior, the dielectric peak and $d\varepsilon_r/dT$ are both depressed with increasing field.

A variety of ferroelectrics have been explored for thermal imaging applications. Some of the most important materials are listed in Table 4.1.

Table 4.1A. Properties and Figure of Merits of Normal materials for Imaging Applications. (From [54])

Material	Bias kV/cm	T_C (^0C)	c' J/cm^3K	p' uC/cm^2K	ε_r	$\tan\delta$	F_V cm^2/C	F_D $(cm^3/J)^{1/2}$	
Single crystals									
TGS	0	49	2.3	0.028	38	0.01	3620	0.066	
DTGS	0	60	2.4	0.055	43	0.02	6020	0.083	*
ATGSAs	0	51	2.5	0.07	32	0.008	9900	0.19	
$LiTaO_3$	0	665	3.2	0.18	43	0.003	1440	0.051	
$LiNbO_3$	0	1210	3.0	0.083	28	0.005	1140	0.025	
SBN 46/54	0	132	2.1	0.043	380	0.003	610	0.065	
PGO:Ba	0	70	2.0	0.032	81	0.001	2200	0.19	*
Ceramics									
PLZT 7/65/35	0	150	2.6	0.13	1900	0.015	300	0.032	
PLZT 8/65/35	0	105	2.6	0.18	4000	0.03	190	0.006	
PZNFTU	0	230	2.7	0.039	290	0.0031	570	0.052	
PSZNFTU	0	170	2.7	0.049	400	0.0028	520	0.058	
PGO	0	178	2.6	0.002	25	0.003	530	0.009	
Polymerics									
PVDF	0	nono	2.4	0.0027	12	0.015	1040	0.009	*
Thin Films									
$PbTiO_3$ sol-gel	0	490	2.9	0.095	200	0.02	8701	0.056	
PLT 90/10 sputtered	0	330	3.2	0.065	200	0.006	1150	0.062	
PCT70/30 sputtered	0	270	3.3	0.052	390	0.015	440	0.021	
PZT 54/46 sol-gel	0	380	3.1	0.07	950	0.016	260	0.019	

*developed by terms of U.K.

Table 4.1B. Acronyms and Chemical Formulas. (From [54])

Acronym	Name	Formula
TGS	Triglycine sulfate	$(NH_2CH_2COOH)_3H_2SO_4$
DTGS	Deuterated TGS	$(ND_2CD_2COOD)_3D_2SO_4$
ATGSAs	Alanine+As-doped TGS	$(NH_2CH_2COOH)_3H_2SO_4$: $NH_2CH_2CH_2COOH; H_3AsO_4$
DTGFB	Deuterated Triglycine fluoberyllate	$(ND_2CD_2COOD)_3D_2BeF_4$
KTN	Potassium tantalate niobate	$KTa_{1-x}Nb_xO_3$
BST	Barium strontium titanate	$Ba_{1-x}Sr_xTiO_3$
BSCT	Barium strontium calcium titanate	$Ba_{1-x-y}Sr_xCa_yTiO_3$
SBN	Strontium barium niobate	$Sr_{0.5}Ba_{0.5}Nb_2O_6$
PT	Lead titanate	$PbTiO_3$
PCT	Lead calcium titanate	$Pb_{1-x}Ca_xTiO_3$
PLT	Lead lanthanum titanate	$Pb_{1-3x/2}La_xTiO_3$
PLZT	Lead lanthanum zirconate titanate	$Pb_{1-x}La_x(Zr_{1-y}Ti_y)_{1-x/4}O_3$
PZT	Lead zirconate titanate	$PbZr_{1-x}Ti_xO_3$
PZFNTU	Modified PZT	$PbZr_{0.58}Fe_{0.2}Nb_{0.2}Ti_{0.02}O_3:U$
PSZFNTU	Sr-doped modified PZT	$Pb_{1-x}Sr_xZr_{0.58}Fe_{0.2}Nb_{0.2}Ti_{0.02}O_3:U$
PScT	Lead scandium tantalate	$PbSc_{1/2}Ta_{1/2}O_3$
PMN	Lead magnesium niobate	$PbMg_{1/3}Nb_{2/3}O_3$
PZN	Lead zinc niobate	$PbZn_{1/3}Nb_{2/3}O_3$
PZNT	PZT-PZN solid solution	$PbZr_{1-x-y}Zn_{x/3}Nb_{2x/3}Ti_yO_3$
PcoW	Lead cobalt tungstate	$PbCo_{1/2}W_{1/2}O_3$
PGO	Lead germanate	$Pb_5Ge_3O_{11}$
PVDF	Polyvinylidence fluoride	$(CH_2-CF_2)_n$

Table 4.1 compares the properties and figure of merits of a variety of conventional pyroelectrics, i.e. poled detectors operating without bias well below the Curie point. In most cases these values represent typical properties reported. Significant variation can be expected as a function of differences in processing. Table 4.2 compares materials that have been studied for application in the phase transition region . Values of F_D appear greatly superior to those for the normal pyroelectric materials in Table 4.1.

Table 4.2. Phase transition Materials $(T \cong T_t)$. (From [54])

Material	Bias kV/cm	T_C (^0C)	c' J/cm^3K	p' uC/cm^2K	ε_r	$\tan\delta$	F_V cm^2/C	F_D $(cm^3/J)^{1/2}$	
Single crystals									
DTGFB	0	74	2.0	1.4	2400	0.02	3300	0.34	
KTN 67/33	2.5	4	3.7	8.0	25000	0.002	100	0.46	
BST 65/35	5	5	2.5	0.3	20000	0.007	1700	0.034	*
Ceramics									
BST 67/33	1	21	3.2	23.0	31000	0.028	2700	0.84	**
BST 67/33	2	22	3.2	6.3	33000	0.021	670	0.25	**
BST 67/33	6	24	3.2	0.70	8800	0.004	280	0.12	**
BST 65/35	40	29	2.5	0.10	1200	0.0013	380	0.11	*
PMN:La	90	40	3.0	0.085	1200	0.0008	800	0.10	*
PScT	53	40	2.7	0.38	2900	0.0027	550	0.17	*
PZT 94/6^	0	50	2.6	0.37	300	0.02	5300	0.019	
PZNT 90/8/2^	0	30	2.6	0.185	290	0.019	2800	0.10	
PCT 70/30: PCoW 96/4	0	106	3.3	3.0	7400	0.037	1380	0.18	
PLZT 8/60/40 (sic)	0	142	3.7	3.2	16200	0.062	600	0.092	
PZN/BT/PT 80/10/10^^	0	12	2.7	5.93	4670	0.01	5310	1.08	
PZN/BT/PT 80/10/10	0	85	2.7	2.9	18300	0.018	660	0.20	
Thin Films									
PScT sputtered	40	40	2.7	0.52	6000	0.012	360	0.076	
PScT sol-gel	--	40	2.7	0.30	7000	0.002	180	0.10	*
PScT MOCVD	20	40	2.7	0.08	1000	0.002	330	0.07	*
KTN metalorganic	30	40	3.7	20.0	1200	0.01	50000	5.0	

^ rhombohedral-rhombohedral phase transition
^^ rhombohedral-tetragonal phase transition
*developed by terms of U.K.
** developed by Texas Instrument

In order to compete with resistive bolometer array, monolithic technology must be developed for high yield and low cost arrays of very large numbers of elements. Therefore, the development of thin film materials has attracted a lot of attention in recent years. Because of the improved thermal isolation possible with the integrated technologies, the detector material response, and therefore merit figures, required in the deposited films for the same level of performance will be lower than in the case of ceramic/hybrid technology.

A number of thin film deposition processes have been studied including sol-gel processing[60-62], rf magnetron sputtering[63-66] and metal-organic chemical vapor deposition (MOCVD)[67]. The deposition to be developed must have adequate control of film chemistry, morphology and electrical performance, and control deleterious reactions of the thin films with silicons using buffer layers. Ultimately, a process that is amenable to volume manufacturing on a consistent basis must be demonstrated.

4.5 Hybrid Ferroelectric Bolometer Arrays Developed by Texas Instruments[15-16, 54, 68-78]

The principal device features of Ferroelectric Bolometer Arrays developed by Texas Instruments are[70]:

- Long-wavelength operation determined by an external optical coat
- Reticulation to increase modulation transfer function (MTF)
- Ceramic BST solid solution compositionally adjusted for a near room temperature ferroelectric phase transition
- 100mm wafer detector processing
- Operation near the phase transition
- Applied electric field to enhance performance
- Bump bonding of detector to ROIC
- Use of a mechanical chopper for field-difference processing.

Texas Instruments uncooled IR technology is based on the induced pyroelectric effect near the phase transition of the ferroelectric ceramic BST. BST is a dielectric mode material, therefore, the TI's FPA needs an external bias voltage. The temperature

dependencies at arbitrary applied voltage of the polarization and relative permittivity are shown in Fig. 4.13. The polarization and permittivity change rapidly near the BST phase transition which makes this the most sensitive operating regime.

Typical dielectric constants and loss tangents for 99% dense BST with Curie point 21^0C are displayed in Fig. 4.14 as a function of bias field and temperature. Samples were polished to approximately 250um thick as provided with fired thick film Ag-Pd electrodes. Good dielectric slope and low loss tangent up to 14kV/cm suggest that useful pyroelectric responsivity might be expected.

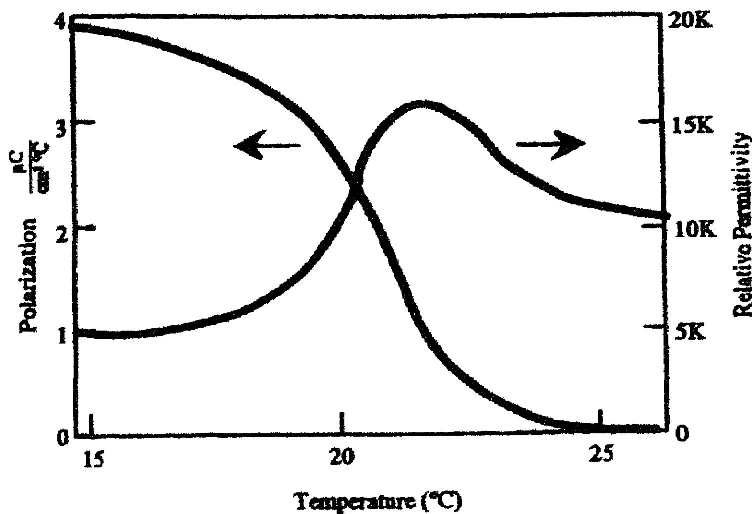

Fig. 4.13 Polarization and permittivity as a function of temperature. (From [71])

Simultaneous pyroelectric current/dielectric property measurements yielded the values of F_V and F_D that are presented in Fig. 4.15. In both cases the figures of merit are dominated by the pyroelectric coefficient. They appear high at low bias and decrease with increasing bias (to around $350\,cm^2 / C$ for F_V), saturating at 4kV/cm or so.

The most promising bulk ferroelectric materials have a large dielectric constant and have operated near a phase transition, a spontaneous dielectric polarization that is a very sensitive function of temperature. The ferroelectric materials were doped with both donors and acceptors to reduce the grain size to values typically between 1-3um and increase the resistivity[68,72].

By varying the barium (Ba) to strontium (Sr) ratio of the BST, one can set the temperature of the phase transition over a wide range. For most applications, this composition is adjusted to allow operation near ambient room temperature and hence to uncooled infrared detectors.

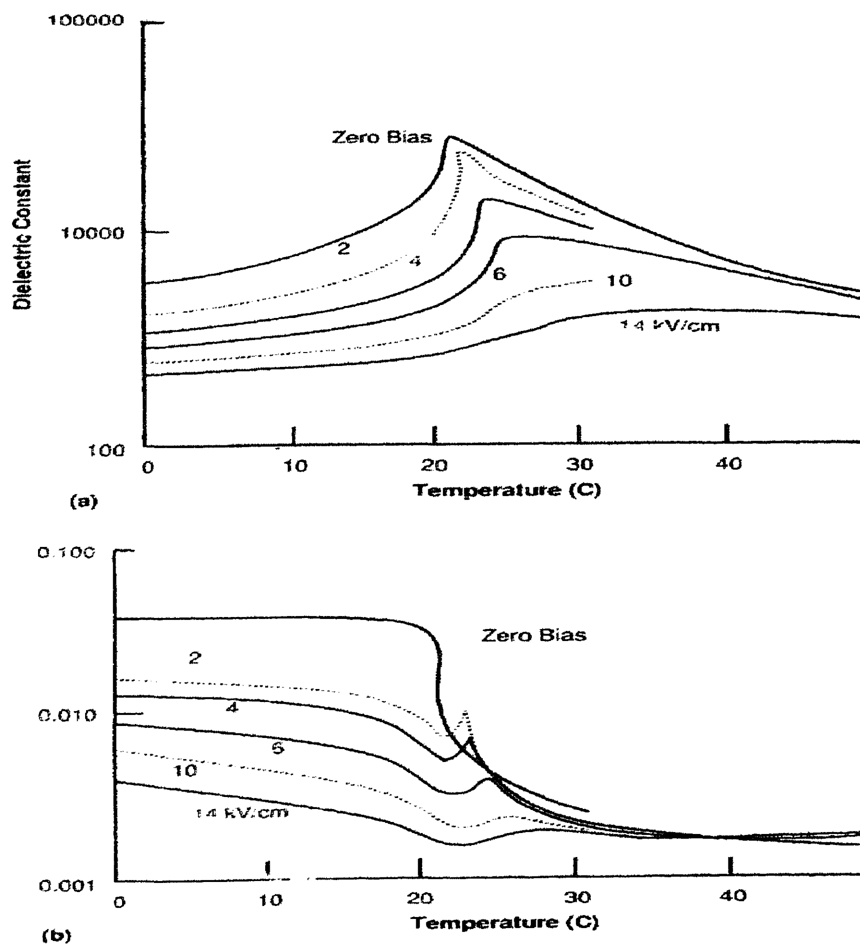

Fig. 4.14 Dielectric constant and Loss tangent for BST. (From [72])

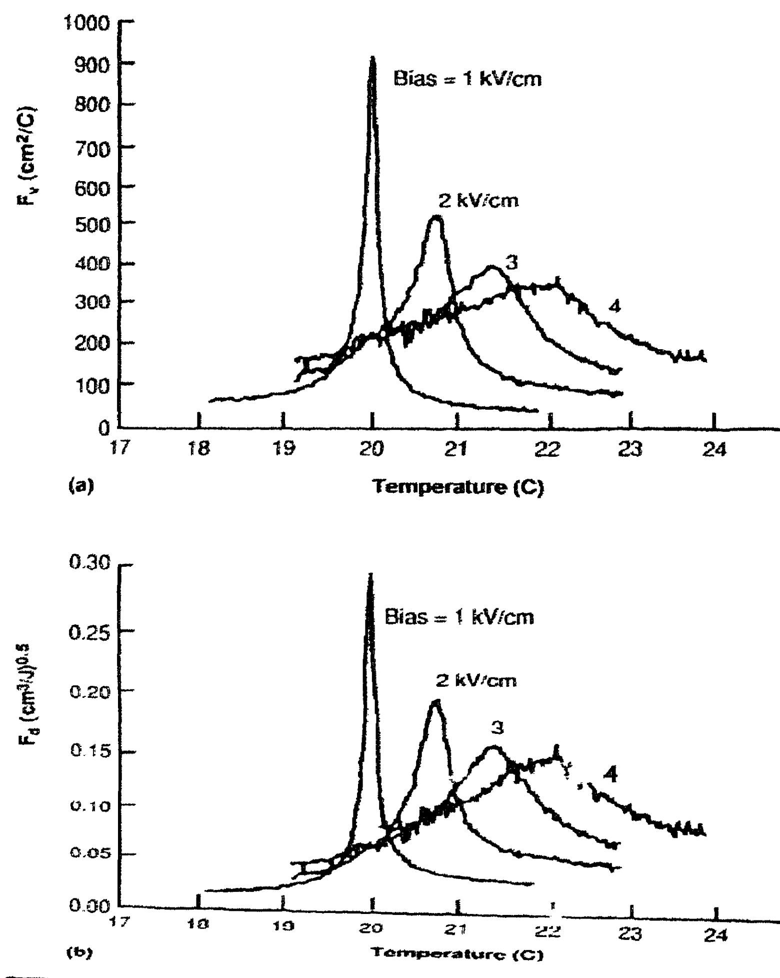

Fig. 4.15 Figure of merits F_V and F_D for BST. (From [72])

The detector array , shown in Figs. 4.16 and 4.17, is reticulated to reduce thermal crosstalk between adjacent pixels. The reticulated pixels are on 48.5um centers, and the kerf is approximately 12um[70]. The backside of each pixel has a metal electrode that serves as one plate of a parallel-plate capacitor. The IR absorber is a three-layer resonant cavity. The final BST thickness is approximately 20um[70]. The TI corporation is still trying to reduce the thickness in order to reduce the thermal capacitance. A finished device with an array of 245*328 pixels has been made.

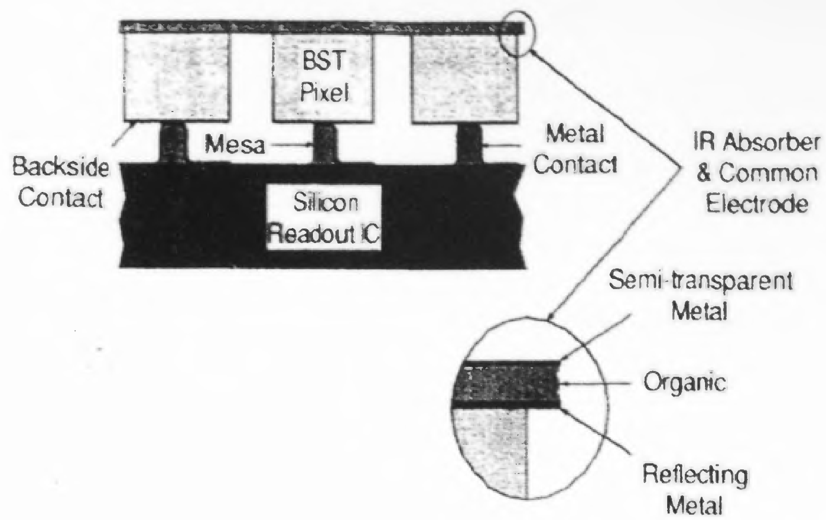

Fig. 4.16 Schematic view of detector pixel structure. (From [76])

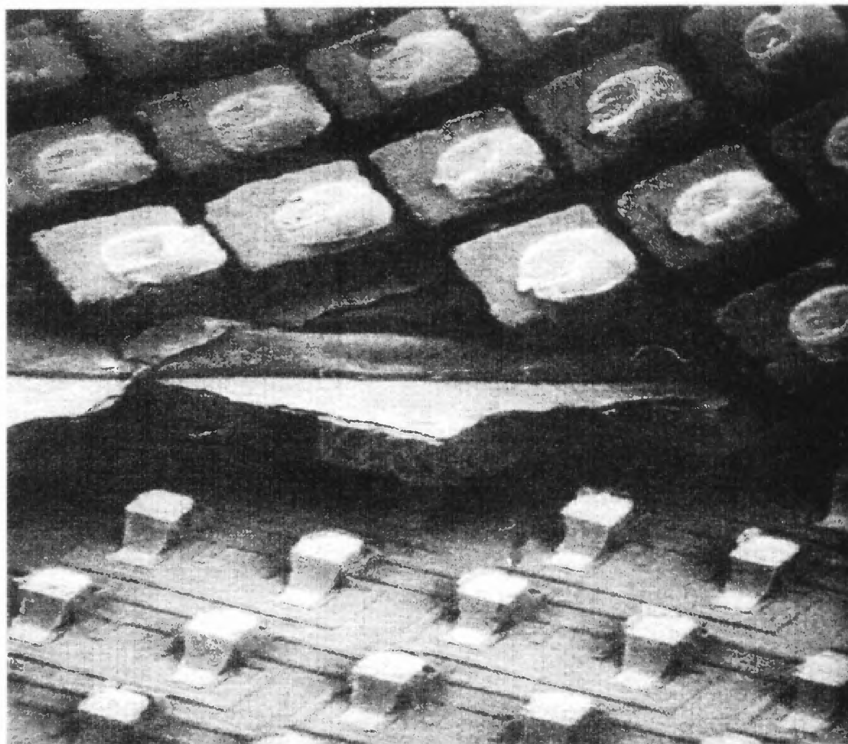

Fig. 4.17 Photograph of uncooled focal plane array, showing the BST peeled back from the ROIC. (From [15])

The ROIC is a CMOS device fabricated using 1.0um design rules[69]. Fig. 4.18[70] shows schematically the unit cell, which contains a high-pass filter, a gain stage, a tunable low-pass filter, a buffer, and an address switch. The feedback resistance is between $10^{11}\Omega$ and $10^{12}\Omega$, which, when attenuated by the Miller effect for a open-loop preamp gain of 200, gives a characteristic frequency of about 10HZ for the high pass filter. The preamplifier is a simple CMOS inverter. The low-pass filter resistance is a diode whose effective impedance is controlled by an in-cell current source. An off-chip voltage determines the current level and hence the resistance, and so the filter is tunable. The high-pass capacitor is actually the gate of NMOS transistor biased to accumulation. The near unity-gain output buffer provides the ability to drive the relatively high capacitance load of the column-address lines and column amplifiers. The array implementation of the unit cells (Fig. 4.19) is standard. A row-address shift register addresses each row sequentially. The addressed row is activated by turning on all the unit-cell switches in that row. This connects the pixel buffer outputs in that row to column-address lines. At the end of the column-address lines are amplifiers, one for each column, having a gain of 1.8. The outputs of the amplifiers feed a multiplexer that provides sequential external access to the outputs. Thus the array output is compatible with standard TV formatting. The array mounts onto a single-stage thermoelectric cooler for stabilization near the ferroelectric phase transition. The ceramic device interface process (DIP) array package is completed by the attachment of an anti-reflection coated germanium window that allows IR transmission in the 7.5 to 13um spectral band.

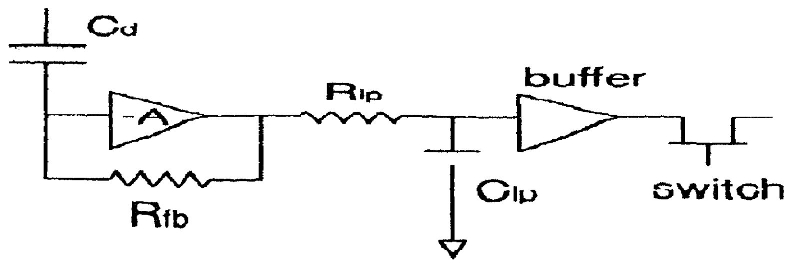

Fig. 4.18 Schematic diagram of the ROIC pixel unit cell. (From [78])

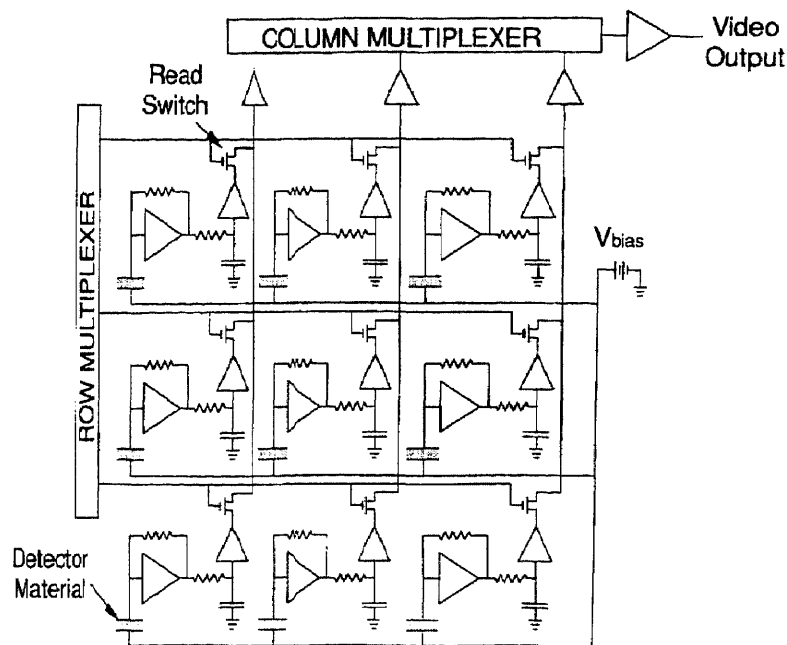

Fig. 4.19 Readout IC array implementation of the unit cells. (From [78])

Operation of TI's uncooled sensor is best described in conjunction with the system block diagram in Fig. 4.20[78]. The IR lens, typically f/1.0 with a focal length of about 100 mm, forms an IR image on the focal plane array. The chopper periodically interrupts the optical beam. The action of the chopper modulations the incident radiation between the field of view of the pixels and the "scene average." The temperature of each pixel rises and falls accordingly and generates a signal by virtue of its pyroelectric response. The

readout IC filters, amplifies, samples and multiplexes the detector signals, one row at a time, and delivers the output at standard RS170 rates. The samples occur immediately prior to closing the chopper in the next field. The output of each pixel is ac coupled, and so, for a static scene, the fields are identical but of opposite polarity. An off-focal-plane high-pass filter at the multiplexer output removes any distracting artifacts that may result from temperature or bias drift. After a gain stage of between 2* and 4*, a 6-bit analog offset correction removes gross offset non-uniformities.

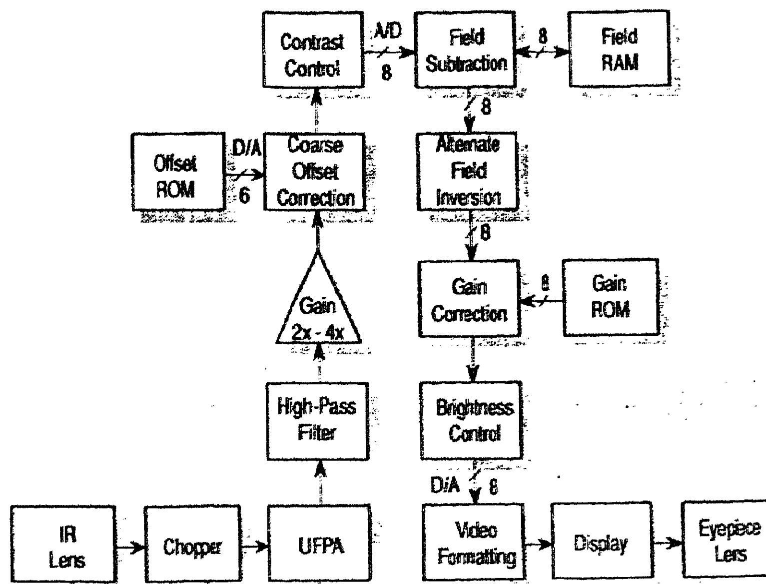

Fig. 4.20 UFPA system functional block diagram. (From [78])

At this point in the processing chain an external contrast setting determines overall gain. As the system converts the video field to 8-bit digital data, the corresponding pixel data stored from the previous field are retrieved, replaced with the present data, and the previous data are subtracted from the present data. Thus, the net output is the difference between samples taken with the chopper open and with the chopper closed. On alternate

fields the system changes the sign of the result to maintain consistent polarity from field to field. This has the added effect of totally removing offset non-uniformities. Prior to analog conversion and RS170 formatting, a gain word multiplies the value of each pixel to compensate for gain non-uniformities, and a digital adder sets overall brightness. The resulting image is uniform to within about 1.5%. The data are then ready for display and viewing on either an internal or external monitor.

A summary of parameters of TI's UFPA is[15]:

	Typical	Planned
Detector Material	(BaSr)TiO3	
Pyroelectric Coefficient	$630 nC / cm^2 / ^\circ C$	
Dielectric Constant	10,000	
Capacitance	3 pF	
Operating temperature	$22 ^\circ C$	
Bias Voltage	15V	
Effective Temp. Coeff.	12%	
Responsivity	85,000 V/W	
Pixel Pitch	48.5um	48.5um * 35um
Pixel Thickness	25um	5um
Thermal isolation	$200{,}000\ ^\circ C / W$	$2{,}000{,}000\ ^\circ C / W$
Thermal Time Const.	15 ms	
Optical Fill Factor	100%	
Absorber Efficiency	95%	
Array Size	245*328	245*454
ROIC	1um CMOS	0.8um CMOS
NETD*	$<0.08 ^\circ C$	$0.03 ^\circ C$
Defects	<100	

*System Level NETD of 0.047K has been demonstrated and devices with NETD less than 0.08K are produced routinely[70].

4.6 Hybrid Pyroelectric Arrays Developed in United Kingdom [56,59,60,63-64,67,70-94]

The uncooled thermal imager technologies developed in United Kingdom are mainly developed by "Defense Research Agency (DRA)" (the former Royal Signals and Radar

Establishment) and "GEC Marconi Materials Technology" (the former Plessarch Research Caswell Ltd.). The reports about their works have provided the author with a good background on the fundamental concepts of thermal structure, readout integrated circuit and material properties.

The hybrid thermal structure developed in UK is described in section 4.2. The detector wafer and ROIC silicon wafer are prepared separately and then bonded together. The structure is shown in Fig. 4.5.

Many materials have been studied by DRA and GEC for their pyroelectric array. They can be seen in Tables 4.1A and 4.2 of section 4.4. The materials marked with * on the last column are developed by DRA or GEC. In order to compete with bolometer FPAs, the pyroelectric or ferroelectric FPAs should be made with a monolithic process for low cost. Therefore, the technologies of deposition of thin films on silicon becomes very important. From Table 4.2 of section 4.4, it can be seen that DRA and GEC have paid much attention to the development of PScT thin film technology.

The ROIC designed by standards for the UK is shown in Fig. 4.21. The pyroelectric detector elements are shown shaded. The schematic shows one line of a two dimensional array. Each pixel contains the detector element, a MOSFET preamplifier and a MOSFET switch which couples to the sense line. Also included within the pixel is a MOSFET switch which allows the detector voltage, at its interface with the buffer amplifier, to be reset. The resistance R_l at the output of the sense line acts as a source follower load to the individual preamplifiers as these are connected in turn to the sense line. C_l is the sense line capacitance. The preamplifier decouples the detector capacitance from the large stray capacitance on the line. The line filter R_b, C_b is placed before the

sample and hold circuit so that high frequency components may be removed before they are aliased. However the line filter must pass the individual pulses from the elements and the filter can operate only at frequencies well above the frame rate. Despite this, the line filter provides a noise reduction in keeping with high performance arrays.

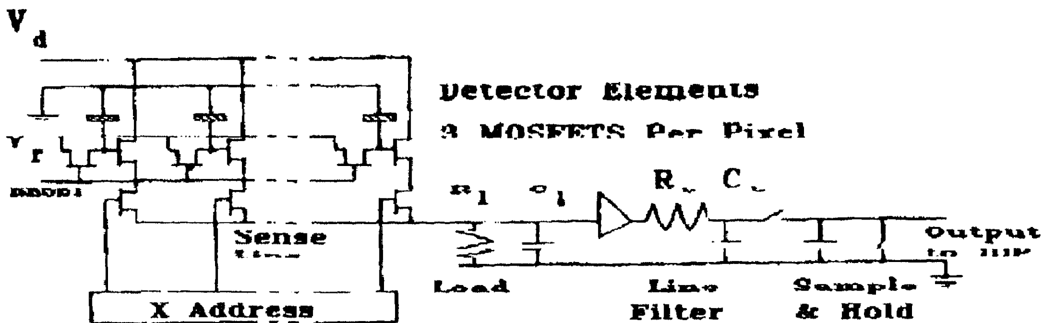

Fig. 4.21 The pixel circuit and line filter designed by the terms in UK. (From [59])

4.7 Monolithic Thin Film Pyroelectric Arrays Developed at University of Minnesota[95-99]

The three-dimensional cross section of a detector element is shown in Fig. 4.22. The pyroelectric thin film is a sol-gel deposited $PbTiO_3$. A silicon nitride microbridge is used to achieve high thermal resistance. An NMOS preamplifier cell is located directly beneath the microbridge element.

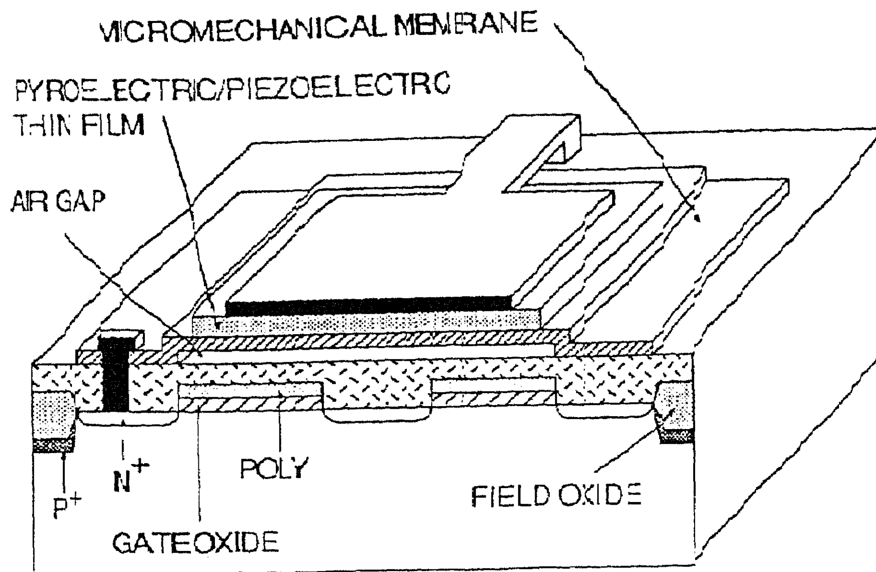

Fig. 4.22 Basic micromachined device structure with thermal isolation bridge, pyroelectric thin film, and preamplifier cell. (From [99])

The basic manufacturing process steps are shown in Fig. 4.23.

a) 3-um NMOS/CMOS signal conditioning electronics (including preamplifier) are made.

b) A LPCVD 1.0um-thick silicon nitride encapsulation layer is deposited over the active circuitry prior to microsensor fabrication. A 1.0um-thick layer of LPCVD PSG (phosphosilicate oxide glass) is deposited to form the sacrificial layer.

c) A low-stress silicon nitride is deposited on the PSG sacrificial layer by LPCVD at 800°C to form a thermally isolated microbridge. Sputtered Ti/Pt is used as the lower electrode. Adhesion difficulties between the silicon nitride and Ti layer sometimes occur. An approximately 1000°A adhesion layer of undoped polysilicon (not shown) has been used to eliminate the problem. Sol-gel $PbTiO_3$ of approximately 3500°A-thickness is then deposited. The upper electrode is next deposited. It is typically Au, FeNi or Ti/Pt.

d) Appropriate Al electrical interconnection lines and bonding pads are patterned. Lateral etching of the PSG sacrificial layer is then carried out to form a free standing silicon nitride microbridge

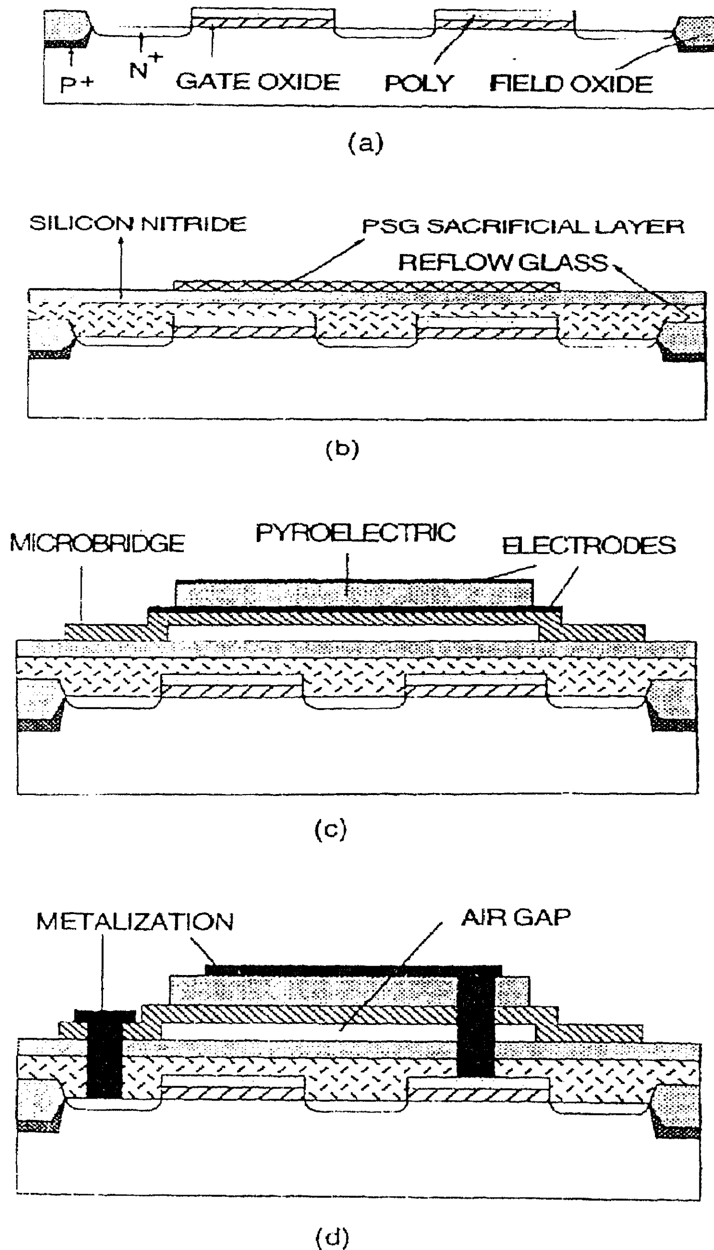

Fig. 4.23 Basic process flow for vertically-integrated pyroelectric detectors. a) Fabrication of on-chip NMOS electronics to the point of contact opening, b) encapsulation patterning of sacrificial PSG layer, c) active film and electrode patterning, and d) final etching of PSG layer. (From [99].)

The $PbTiO_3$ material is selected for the pyroelectric detector because of

1) its high pyroelectric coefficient of 90 $nC/cm^2.K$,
2) its Curie temperature, which is very high (~490°C) leading to a wide operating temperature range ,
3) material figure of merit which is very high compared with the other materials in the PZT-family,
4) low piezoelecric coefficient which reduced the microphonic noise,
5) its silicon-compatible manufacturing process.

Other PZT-type materials are also studied by University of Minnesota. A summary of measured material parameters is given in Table 4.3[99].

Table 4.3. Material parameters of sol-gel thin films prepared at University of Minnesota. (From [99])

	PZT (54/46)	$PbTiO_3$	La-$PbTiO_3$	PLZT(9/54/46)
Pyro. Coeff. * ($nC/cm^2.K$)	50-70	75-96	65	20
Piezo. Coeff. d_{33} (pC/N)	190-220	15-20	--	200
Dielectric Const.	800-1100	80-120	110	110
Dielectric Breakdown (MV/cm)	0.6-1.0	0.5	--	--
Electrical Fatigue (# cycle $\pm$ $10V$)	10^{10}	10^{10}	--	--
Resistivity ($\Omega - cm$)	$10^7 - 10^8$	$10^7 - 10^8$	10^8	10^8
Loss Tangent $(\tan d) * 10^{-3}$	8-20	10-30	4	4-6
Eff. Young's Modulus $E/(1-n) * 10^{11} N/m^2$	4.0-4.6	4.5	--	3.9
Intrinsic Stress $* 10^8 N/m^2$	2.6-6.8	2.1-5.3	--	3.0
*includes primary plus secondary piezoelectric responses				

The pyroelectric integrated detector performance is summarized in Table 4.4[99].

Table 4.4 Smmary of measured pyroelectric integrated detector performance

	$PbTiO_3$-on polysilicon [98]*	$PbTiO_3$-on silicon nitride[99]**
Film thickness	0.36 um	
Relative Dielectric Const.	200	
Pyroelectric coefficient	$90 \pm 5nC / cm^2.K$	
Capacitance	4.4 pF	
Thin Film Resistivity	$>1*10^8\ \Omega - cm$	
Dielectric Loss Tangent at 30Hz	0.020 ± 0.005	
NMOS Integrated Circuit Properties		
Design Rule	3 um	
V_T	-0.8 V	
C_{ox}	138 nF / cm^2	
μ_n	400 $cm^2 / V.\sec$	
Transistor Count	~10000	
Transistor Yield	100%	
Performance Figures of Merit		
Blackbody Voltage Responsivity	$1.2*10^4$ V/W (at 30Hz)	$4.2*10^4$ V/W (at 50 Hz)
Noise-voltage	$0.3 \pm 0.1\ \mu V / Hz^{1/2}$	
Normalized Detectivity (D*)	$2*10^8\ cm.Hz^{1/2} / W$ (at 30 Hz)	$1.2*10^8\ cm.Hz^{1/2} / W$ (at 50 Hz)

* $PbTiO_3$ thin film sensor measures 30*30 um^2 and polysilicon microbridge measures 50*50 um^2 with 75 um pitch.

** The low-stress silicon nitride is used to replace the previous n-type polysilicon microbridge, because n-type polysilicon exhibits an as-deposited compressive stress and need a high temperature annealing (>1000°C).

CHAPTER 5

REVIEW OF THE THEORY AND PERFORMANCE OF THERMOELECTRIC UNCOOLED INFRARED ARRAYS

5.1 Seeback Effect

Consider Fig. 5.1, the two leads of (semi)conductor materials a and b are connected at one end, and the electrical voltage is measured between the two remaining ends. At thermal equilibrium, there will be a zero voltage. But if the temperature at the connection point is raised with respect to the ambient while the two remaining ends are still at ambient, an open-circuit voltage ΔV will be measured. This effect, called the Seeback effect after its discoverer T. J. Seeback (1770-1831), can be mathematically expressed by

$$\Delta V = (\alpha_a - \alpha_b)\Delta T \tag{5.1}$$

where α_a is the Seeback coefficient of material a, α_b is the Seeback coefficient of material b and ΔT is the temperature difference. The unit of Seeback coefficient is VK^{-1}.

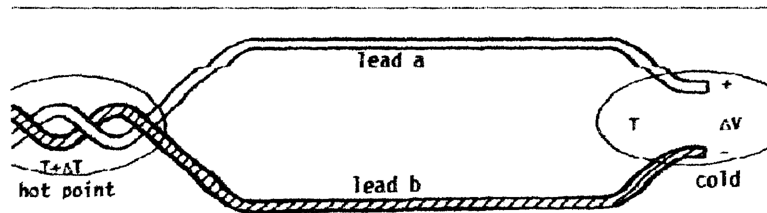

Fig. 5.1 The **Seeback effect: an electrical voltage ΔV due to a temperature difference** ΔT.

A thermocouple which is basically the two wire device shown in Fig. 5.1 can be used to detect infrared radiation which controls ΔT. To increase the output signal, a number of thermocouples can be connected in series to form a thermopile.

Fig. 5.2 shows a schematic of an thermopile sensor with cantilever beam structure. The radiation is absorbed and converted to a temperature increase near the "hot" junctions of the thermopile located on the thin membrane, whereas the "cold" junctions are located on the bulk silicon acting as heat sink. The output signal V_S can be expressed by

$$V_S = N(\alpha_a - \alpha_b)\Delta T \tag{5.2}$$

where N is the number of thermocouple, α_a and α_b are the Seeback coefficients of material a and b respectively and ΔT is the temperature difference between the "hot" and "cold" junctions.

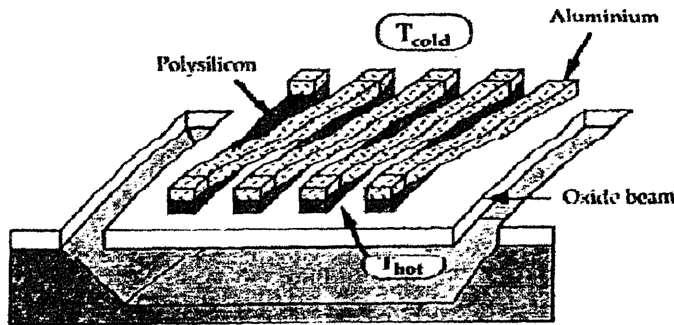

Fig. 5.2 Schematic of a cantilever beam structure thermopile with IR absorber at "hot" area. (From [100])

The temperature difference ΔT can be approximately expressed by

$$\Delta T = \frac{F_A \eta W}{\left(K_{th}^2 + \omega^2 C_{th}^2\right)^{1/2}} \tag{5.3}$$

Therefore,

$$V_S = \frac{F_A \eta N W(\alpha_a - \alpha_b)}{\left(K_{th}^2 + \omega^2 C_{th}^2\right)^{1/2}} \tag{5.4}$$

and

$$R_V = \left(\frac{V_S}{W}\right) = \frac{F_A \eta N(\alpha_a - \alpha_b)}{\left(K_{th}^2 + \omega^2 C_{th}^2\right)^{1/2}} \tag{5.5}$$

with

$$K_{th} = K_{beam} + K_{gas} + K_{rad} + N(K_a + K_b) \tag{5.6}$$

$$F_A = \frac{A_{eff}}{A_{pixel}} \tag{5.7}$$

where

W: incident infrared radiant power,

η: absorbtivity of detector,

K_{th}: total thermal conductance from "hot" junctions to "cold" junction (substrate),

C_{th}: thermal capacitance,

F_A: fill factor,

A_{eff}: sensor area with absorber material,

A_{pixel}: pixel area,

K_{beam}: the conductance due to thermal conductance loss via the cantilever beam,

K_{gas}: the conductance due to the gaseous conductance loss,

K_{rad}: the conductance due to radiation loss,

K_a, K_b: the conductance due to thermal conductance loss via the material a and b.

The dominant Johnson noise voltage is given by

$$V_J = (4k_B TNR_d)^{1/2} \quad (V / Hz^{1/2}) \tag{5.8}$$

where R_d is the resistance of one pair of thermocouple.

The detectivity D^* is given by

$$D^* = \frac{A_{pixel}^{1/2} R_V}{V_J}$$
$$= \frac{A_{pixel}^{1/2} \eta N^{1/2} (\alpha_a - \alpha_b) F_A}{(4k_B T R_d)^{1/2} \left(K_{th}^2 + \omega^2 C_{th}^2\right)^{1/2}} \quad (5.9)$$

Since the best performance of radiation sensors is accompanied by high sensitivity and low noise, Eqs. 5.4-5.9 lead to the requirements of

- high Seeback coefficient $\alpha_a - \alpha_b$,
- low thermal conductance K_{th},
- low resistance R_d,
- high fill-factor F_A.

The design of the thermopile and that of the thermal structure directly influence each other. Very high thermal isolation of the sensitive area require using long, narrow beams which in turn requires a long, narrow thermopile with few strips. However, this design would result in low sensitivity. Increasing the number of strips (N) at a constant cantilever beam area requires narrow thermocouple strips, which causes a higher electrical resistance (R_d). The fill-factor (F_A) is also important. Increasing F_A does not directly mean an increase in the temperature difference (ΔT) because K_{th} also increases. Therefore, optimizing the thermopile sensors by choosing an appropriate thermal structure, material properties and strip structures is necessary. Design example for cantilever beams[100-102] and membrane[101-104] can be found at reference.

Thermopiles have some attractive properties:

- the output signal is without offset and offset drift, because there is no output signal without input power;

- bias is not required;
- readout circuitry can be very simple, because voltage is generated directly;
- chopper and temperature control are not required.

However, the thermopiles also have some disadvantages compared with bolometer and pyroelectric sensors:

- the sensitivity is low (~100V/W);
- the spatial resolution is low, because a large pixel area is necessary for high sensitivity.

The signal voltage is direct proportional to the temperature difference (ΔT) between the "hot" junctions and "cold" junctions which is at substrates and the number of thermocouples (N). Therefore, the pixel area can not be too small.

Recent research on thermopile sensors has focused on the development of a CMOS compatible process technology. A lot of papers can be fount at "Sensors and Actuators A". This reported research is generally to develop low cost, high sensitivity, discrete thermopile[101, 105-112].

5.2 Materials

The Seeback effect is a bulk property which can be expressed as [105]

$$\frac{\Delta E_F}{q} = \alpha_S \Delta T \tag{5.10}$$

where E_F is the Fermi energy. Notice that Eq. 5.10 shows the offsetless character of the Seeback effect. There will be no gradient in the Fermi energy level, and therefore in the electrical potential, unless there is a temperature gradient.

The total Seeback coefficient in non-degenerate n-type silicon can be approximated by [105]

$$\alpha_S = -\frac{k_B}{q}\left[\ln\left[\frac{N_C}{n}\right] + 2.5 + s_n + \varphi_n\right] \tag{5.11}$$

with q as the elementary charge, k_B as the Boltzmann constant, N_C as the conduction-band density of states and n the electron density (fixed by the doping concentration). The factor s_n is the exponent in the exponential relation between the mean-free-time between collisions and the energy, which is typically a value between -1 to 2. The phonon-drag effect is represented by φ_n , and it ranges from 0 for highly-doped silicon to 5 for low-doped silicon at room temperature. For p-type silicon a similar expression is found, except that the coefficient is now positive.

The Seeback coefficient can also be approximated as a function of electrical resistivity

$$\alpha_S = \frac{mk_B}{q}\ln\left(\frac{\rho}{\rho_o}\right) \tag{5.12}$$

with $\rho_o \cong 5*10^{-6}\Omega m$ and $m \cong 2.6$ as constants[105].

The Seeback coefficients as measured for crystal silicon and polysilicon made at different manufacturing processes are shown in Figs. 5. 3 and 5.4.

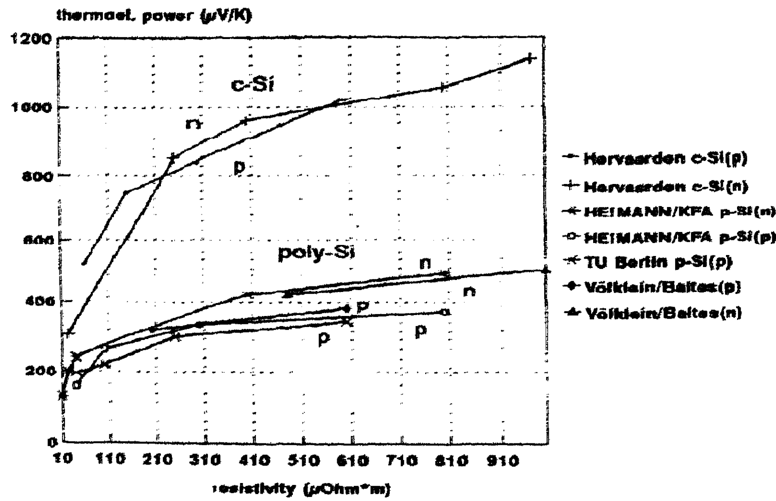

Fig. 5.3 Measured Seeback coefficient vs. volume resistivity at T=300K. (From [113])

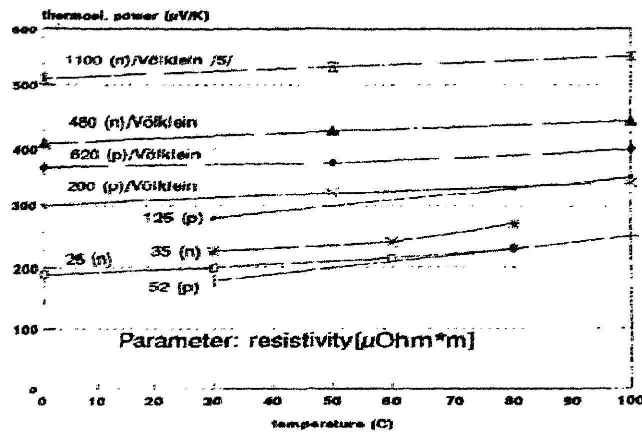

Fig. 5.4 Measured Seeback coefficient vs. temperature for polysilicon. (From [113])

The effects of temperature and dopant concentrations on the Fermi energy of semiconductor material is shown in Fig. 5.5. The Seeback coefficient α_S is directly proportional to the temperature gradient of Fermi energy level. Therefore, the material with low carrier concentrations has high Seeback coefficient than high carrier concentrations.

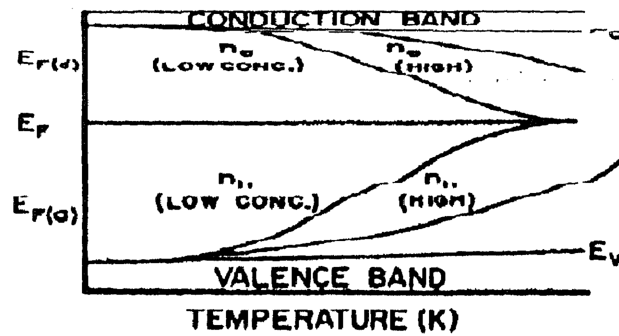

Fig. 5.5 Effects of temperature and dopant concentrations on the Fermi energy of semiconductor material. (From [114])

To compare different thermoelectric materials, it is convenient to use a figure of merit Z for a single material[115]

$$Z = \frac{\alpha_S^2}{\rho k_C} \tag{5.13}$$

where α_S is the Seeback coefficient, ρ is the electrical resistivity and k_C is the thermal conductivity of material.

Measured values for key properties of thermoelectric materials are given in Table 5.1 along with calculated values for Z. The doped $Bi_xSb_yTe_z$ have the best material figure of merits. But they can not be made by a CMOS compatible process; therefore, doped silicon or polysilicon and aluminium are chose for CMOS compatible process. The resistivity and Seeback coefficient can be varied by changing doping concentration. However, the resistivity increases much faster than the square of Seeback coefficient. The doping concentration has to be optimized carefully to obtain a high sensitivity-noise ratio.

Table 5.1 Measured values for selected thermoelectric materials and calaulated figure of merit Z. (From [113])

Element	Symbol	$\alpha_S(uVK^{-1})$	$\rho(u\Omega m)$	$k_C(Wm^{-1}K^{-1})$	$Z(K^{-1})$
p-Si	Si	100-1000	10-500	~150	**
p-Poly-Si	Si	100-500	10-1000	~20-30	**
Antimony	Sb	32	18.5	0.39	$1.42*10^{-4}$
Iron	Fe	13.4	0.086	72.4	$2.88*10^{-5}$
Gold	Au	0.1	0.023	314	$1.38*10^{-9}$
Copper	Cu	0	0.0172	398	0
Silver	Ag	-0.2	0.016	418	$6.0*10^{-9}$
Aluminium	Al	-3.2	0.028	238	$1.54*10^{-6}$
Platinum	Pt	-5.9	0.0981	71	$5*10^{-5}$
Cobalt	Co	-20.1	0.0557	69	$1.05*10^{-4}$
Nickel	Ni	-20.4	0.0614	60.5	$1.12*10^{-4}$
Bismuth	Bi	-72.8	1.1	8.1	$5.94*10^{-4}$
n-Si	Si	-100 to -1000	10-500	~150	**
n-Poly-Si	Si	-100 to -500	10-1000	~20-30	**
$p-Bi_{05.}Sb_{1.5}Te_3$		230	580	1.05	$2.9*10^{-3}$ *
$n-Bi_{087.}Sb_{0.13}$		-100	14.0	3.1	$4.5*10^{-4}$ *

* From [116].
** The figures of merit depend on manufacturing process and dopant concentration.

5.3 Thermopile Arrays

Three reported thermopile arrays are now described below. They were developed respectively by the University of Michigan, Honeywell and Japan Defense Agency.

5.3.1 Thermopile Array Developed by University of Michigan[103,104,117-118]

The latest thermopile pixel structures developed by University of Michigan are shown in Fig. 5.6. The pixel size in both structures is 375um*375um with a light absorbing (active) area of 300um*300um. The pixels consist of 32 and 36 n-p polysilicon thermocouples for front-undercut and back-etched pixel structures respectively. Each pixel is self-testing using an embedded resistor network. The doping level of these polysilicon strips is

$10^{20}cm^{-3}$. The n-type polysilicon with this doping yields a Seeback coefficient of about $-200\mu VK^{-1}$ while the p-type polysilicon produces a Seeback coefficient of about $+200\mu VK^{-1}$ [117]. The unblacken front- and back-etched imagers show responsivities of $12VW^{-1}$ and $15VW^{-1}$ respectively, with a time constant of less than 5ms. When blacken, the device responsivities approximately double due to decreased reflection and increased absorption on the dielectric windows.

The imager was designed for automated process control. It has been used for moniting the wafer temperature distribution during rapid thermal processing for semiconductor manufacturing.

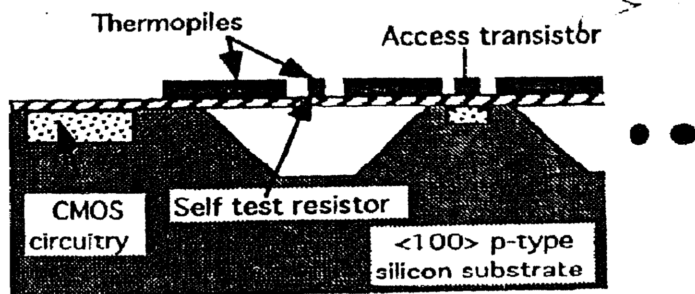

(a) Cross-section of the front-undercut pixel structure

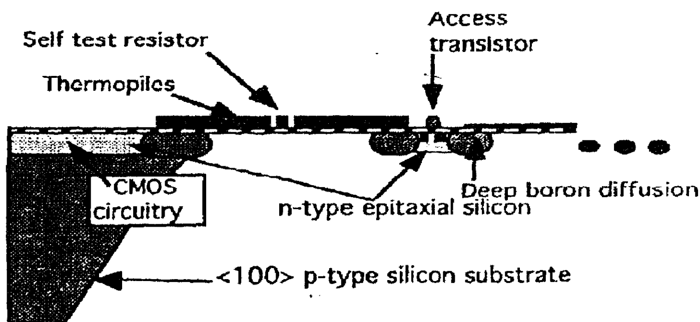

(b) Cross-section of the back-etched pixel structure

Fig. 5.6 (a) Cross-section of the front-undercut pixel structure. (b) Cross-section of the back-etched pixel structure. (From [117])

5.3.2 Thermopile Array Developed by Honeywell[10]

The thermoelectric pixel structure is shown in Fig. 5.7.

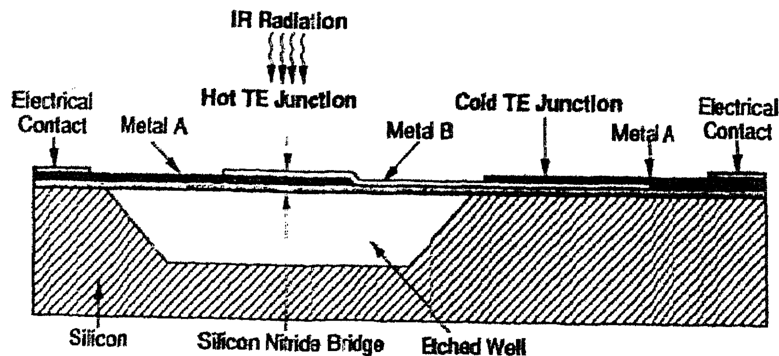

Fig. 5.7 Thermoelectric pixel structure. (From [10])

A 128 element linear thermopile array using this structure was developed for a handheld imaging radiometer. The handheld imaging radiometer uses this 128 element linear thermoelectric array to scan across the focal plane of the germanium lens providing a 120*120 pixel image in 1.44 sec.

5.3.3 Thermopile Array Developed by Japan Defense Agency[119]

This is the only reported thermopile FPA design for night vision applications. The FPA contains 128*128 pixels. The pixel size is 100um*100um. This device has a monolithically integrated structure to increase the fill factor. CCD for signal charge accumulation and signal charge read-out are fabricated on the silicon surface. Over the CCD, silicon dioxide diaphragms for thermal isolation structure are made by using micromaching technology. The diaphragm size is 80*84 μm , and the fill factor is 67%.

The diaphragm is made from a 450nm thick silicon dioxide film. Under the diaphragm, there is a hollow to isolate the diaphragm thermally. The hollow is formed by etching a 1um thick sacrificial polysilicon layer. On each diaphragm, 32 pairs of p-type boron-doped polysilicon and n-type phosphorous-doped polysilicon thermopiles are formed. The polysilicon electrode is 70nm thick and 0.6um wide. Hot junctions are located at the central part of the diaphragm, while cold junctions are located on the outside edge of the diaphragm, where heat conductance is very large. The temperature at the cold junction is always the same as the temperature for the substrate. The hot junctions and cold junctions are backed by aluminium layers to reduce contact resistance.

The IR responsivity for a 32 pair thermopile of a pixel was measured in low chopper frequency region to be $1550VW^{-1}$, and the NETD has found to be 0.5K with f/1.0 lens. The cutoff frequency is 130Hz. The responsivity is much larger than the reported values of the University of Michigan sensor.

CHAPTER 6

THE PERFORMANCE OF BOLOMETER, PYROELECTRIC AND FERROELECTRIC DETECTORS

6.1 The Performance of Bolometer Detector

As discussed in chapter 3, the voltage responsivity (R_V), the temperature fluctuation noise (V_T) and the Johnson noise (V_J) of a bolometer detector, as described in Eqs. 3.20, 3.36 and 3.37, are

$$R_V = \frac{R_L}{(R_L + R_m)^2} * \frac{V_0 \eta \alpha R_m F_A}{[K_{eff}^2 + \omega^2 C_{th}^2]^{1/2}}, \tag{6.1}$$

or

$$R_V = \frac{R_L}{(R_L + R_m)} * \frac{I_b \eta \alpha R_m F_A}{[K_{eff}^2 + \omega^2 C_{th}^2]^{1/2}}, \text{ (since } I_b = \frac{V_0}{R_L + R_m})$$

with

$$K_{eff} = \left[K_{th} - \alpha \frac{V_0^2 R_m}{(R_L + R_m)^2} \frac{R_L - R_m}{R_L + R_m} \right] \quad (K_{eff} = K_{th} \text{ for } R_L = R_m)$$

$$V_T = \left(\frac{2 k_B K_{th} (T_0^2 + T_m^2)}{\eta^2} \right)^{1/2} * R_V \quad (V / Hz^{1/2}), \tag{6.2}$$

and

$$V_J = \left[4 k_B * \frac{R_L R_m}{(R_L + R_m)^2} * (T_0 R_m + T_m R_L) \right]^{1/2} \quad (V / Hz^{1/2}) \tag{6.3}$$

The symbols are defined as below:

K_{th} : Total thermal conductance from the element to substrate

C_{th} : Thermal capacitance of the bolometer element

η : Absorbtivity of detector

V_0 : Bias voltage

I_b : Bias current

R_m : The detector's resistance with no input infrared power

T_m : Detector's temperature with no input infrared power with possible dissipation due to electrical bias.

k_B : Boltzmann's constant

R_L : The series load resistance

A_{pixel} : Pixel area

T_0: Substrate temperature

F_A : Fill factor

α : Temperature coefficient of resistance

If MOSFET preamplifiers are used, the two sources of noise in a MOSFET amplifier, current noise I_n and voltage noise E_n, must be considered also. They are represented by

$$I_n = \left(2qI_{GSS}\right)^{1/2} \quad (A / Hz^{1/2}) \tag{6.4}$$

$$E_n = \left(\frac{8k_B T}{3g_m} + \frac{K_F I_{Dq}^{AF}}{g_m^2 f C_{OX} L_{eff}^2}\right)^{1/2}$$
$$= \left(V_a^2 + \frac{Z_a^2}{f}\right)^{1/2} \quad (V / Hz^{1/2}) \tag{6.5}$$

where q is the electronic charge, I_{GSS} is the gate leakage current of a MOSFET, g_m is the transconductance of a MOSFET, C_{OX} is the gate oxide capacitance, L_{eff} is the

effective channel length, K_F is the flicker noise coefficient, A_F is a constant, I_{DQ} is the quiescent drain current, and f is the frequency of operation.

The 1/f noise and random telegraph switching noise of bolometer materials are not considered in the following discussion because they are strongly dependent on the manufacturing process and in theory can be made insignificant. In actual practice, they would be very important for the present amorphous silicon compounds and polysilicon. As described in section 3.4, 1/f noise and random telegraphy switching noise are dominant at present amorphous silicon compounds and polysilicon at low frequencies (f<100Hz).

Therefore, the total noise of a bolometer detector is

$$V_{tot} = \left(V_T^2 + V_J^2 + E_n^2 + I_n^2 R_P^2\right)^{1/2} \quad (V / Hz^{1/2}) \tag{6.6}$$

where

$$R_P = \frac{R_L R_m}{R_L + R_m}$$

Using the above derived equations, the noise source values and normalized detectivity D^* were calculated using a computer program, Sigmaplot, with the reasonable values in Table 6.1 selected for detector parameters. In the following discussions, these values are used if other values are not specified.

Table 6.1 Detector and material properties for a bolometer detector.

$R_m = R_L = 1M\Omega$	$K_{th} = 2 * 10^{-7} (W/^0K)$
$V_0 = 5(V)$	$C_{th} = 2 * 10^{-9} (J/^0K)$
$\eta = 0.8$	$I_n = 1.8 * 10^{-16} (A / Hz^{1/2})$
$T_0 = 300(^0K)$	$V_a = 3.4 * 10^{-9} (V / Hz^{1/2})$
$A_{pixel} = 50 * 50(um^2)$	$Z_a = 2.4 * 10^{-7} (V)$
$F_A = 0.5$	$TCR = 2\%$

The computer calculated noise voltages and D^* are shown in Fig. 6.1. The data show that above 10Hz, Johnson noise is dominant. Therefore, according to Eq. 3.43, D^* can be expressed approximately by

$$D^* = \left(\frac{\alpha}{R_m^{1/2}}\right)\left(\frac{A_{pixel}R_L}{4k_B\left(K_{eff}^2+\omega^2C_{th}^2\right)\left(1+\frac{R_L}{R_m}\right)(R_LT_m+R_mT_0)}\right)^{1/2} F_A\eta V_0$$

$$= \left(\frac{\alpha}{R_m^{1/2}}\right)\left(\frac{A_{pixel}}{8k_B\left(K_{th}^2+\omega^2C_{th}^2\right)(T_m+T_0)}\right)^{1/2} F_A\eta V_0 \quad \text{for } R_m = R_L \tag{6.7}$$

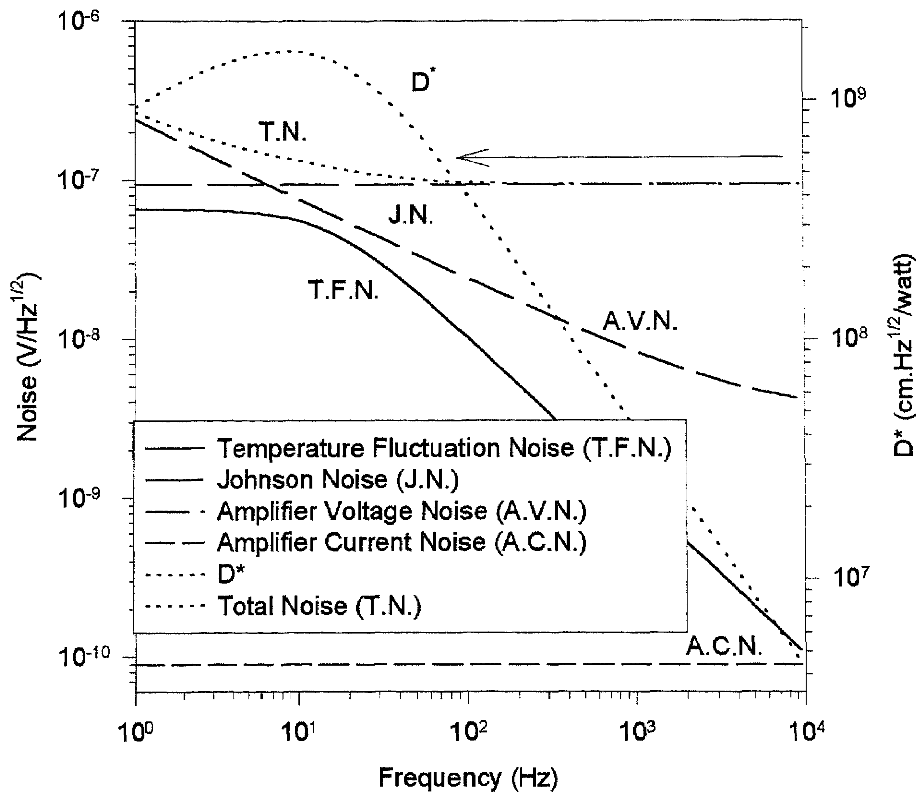

Fig. 6.1 Calculated noise voltage and D^*, $R_m = R_L = 1M\Omega$.

It can be seen from Eq. 6.7 that the total thermal conductance and capacitance of a bolometer, K_{th} and C_{th}, significantly effect its performance. The time constant, C_{th} / K_{th}, essentially controls the frequency response of the detector if the total noise is independent of ω. Below the corner frequency, $\omega_c \equiv K_{th} / C_{th}$, D^* can be approximately represented by

$$D^* \approx \left(\frac{\alpha}{R_m^{1/2}}\right)\left(\frac{A_{pixel}}{8k_B K_{th}^2 (T_m + T_0)}\right)^{1/2} F_A \eta V_0 \tag{6.8}$$

In this region, D^* improves linearly with decreasing thermal conductance.

However, at high frequencies, $\omega >> K_{th} / C_{th}$, D^* can be approximately represented by

$$D^* \approx \left(\frac{\alpha}{R_m^{1/2}}\right)\left(\frac{A_{pixel}}{8k_B \omega^2 C_{th}^2 (T_m + T_0)}\right)^{1/2} F_A \eta V_0 \tag{6.9}$$

Note that D^* is then proportional to C_{th}^{-1}, independent of K_{th}.

The dependence of the various noise voltages and D^* on the thermal conductance of a bolometer, K_{th}, are shown in Figs. 6.2, 6.3 and on ω in Fig. 6.4. Fig. 6.2 shows that as the thermal conductance is decreasing that there is no significant improving in D^* for K_{th} below $2 * 10^{-7}$ W/K, corresponding to at ω_C=100Hz. This is because the chopping frequency 60Hz is less than ω_C. However for thermal conductance values greater than $2 * 10^{-7}$ W/K, D^* deteriorates with increasing thermal conductance. As shown in Fig. 6.3, higher chopping frequency made D^* less dependent on K_{th}; however, if detectors with low conductance can be made, D^* can be increased by decreasing the chopping frequency.

Figs. 6.2 and 6.4 show that all of the noise sources are independent of thermal conductance, K_{th}, except temperature fluctuation noise, V_T, which is generally much

smaller than Johnson noise. Therefore, the total noise voltage is almost independent of thermal conductance, and D^* is almost linearly proportional to the responsivity, R_V.

The temperature fluctuation noise, V_T, Eq. 6.2 is proportional to $\left\{K_{th}\left(1+\left(\frac{\omega}{\omega_C}\right)^2\right)\right\}^{-1/2}$. Therefore, V_T vs. K_{th} is first increasing and then decreasing with thermal conductance as shown in Fig. 6.2.

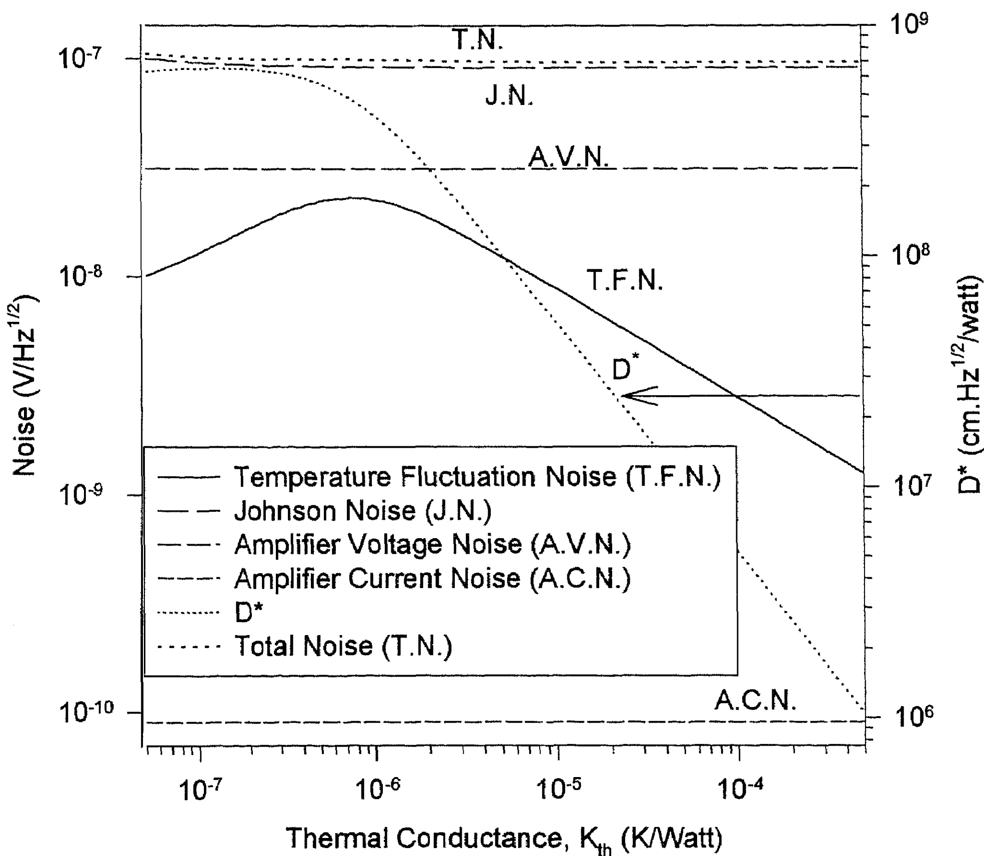

Fig. 6.2 The noise voltages and D^* vs. thermal conductance at a chopping frequency of 60 Hz with $R_m = R_L = 1M\Omega$ and $C_{th} = 2 * 10^{-9} (J/^0K)$.

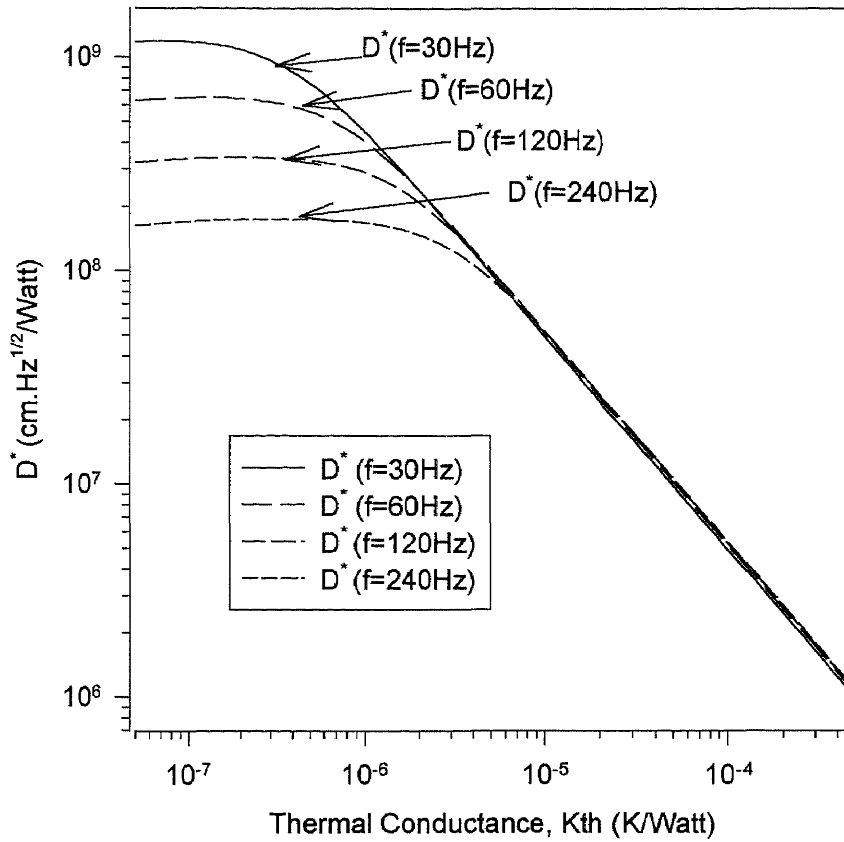

Fig. 6.3 D^* vs. thermal conductance at chopping frequencies of 30, 60, 120 and 240Hz, with $R_m = R_L = 1M\Omega$ and $C_{th} = 2*10^{-9}(J/^0K)$.

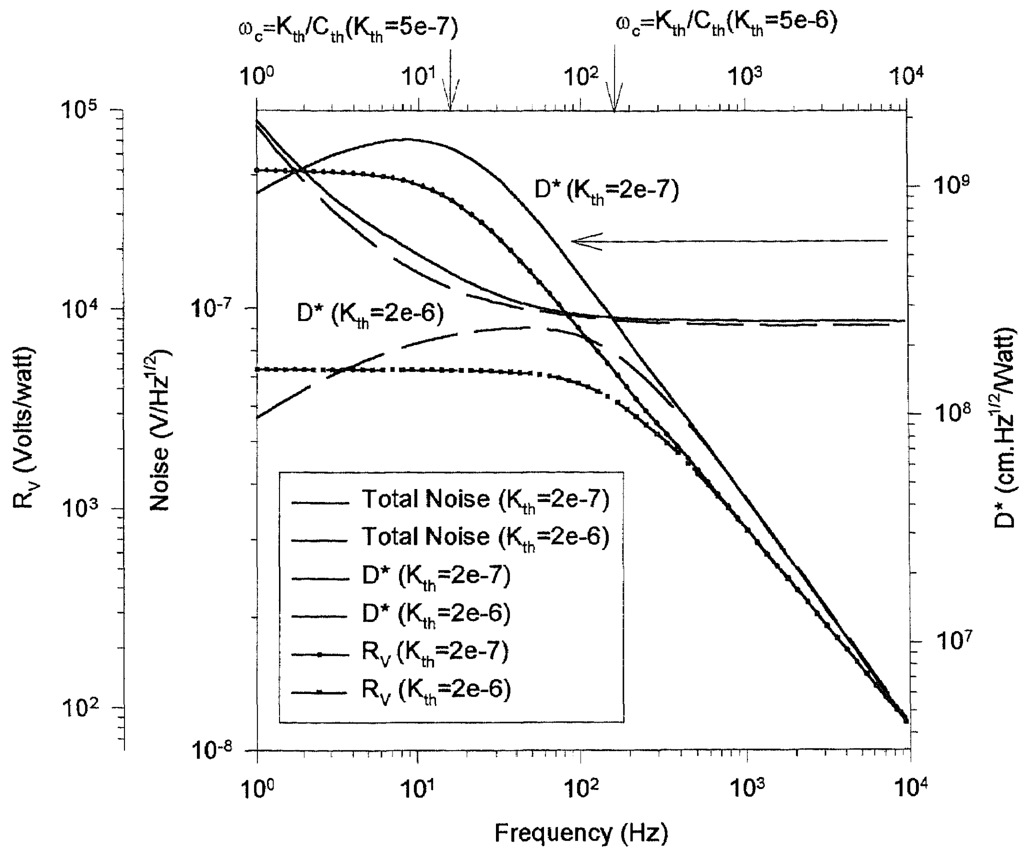

Fig. 6.4 Total noise voltage and D^* for $K_{th} = 2*10^{-7}$ W/K and $K_{th} = 2*10^{-6}$W/K, with $C_{th} = 2*10^{-9}(J/^0K)$ and $R_m = R_L = 1M\Omega$.

From chapter 3, we know that if $R_m = R_L = 10K\Omega$, the detector temperature would be unreasonably high if dc bias was used. Therefore, there is an important incentive to using pulse biasing. If the detector is biased by a voltage pulse with a width of 5us, the thermal time constant $\tau_{th} = \frac{C_{th}}{K_{th}}$, 10ms, would be much longer than the pulse width. Therefore, the detector temperature T_m would not rise significantly as shown by Eq. 3.53:

$$T_m = T_0 + \frac{1}{K_{th}} * \left(\frac{V_0}{R_L + R_m}\right)^2 * R_m * \frac{5us}{\tau_{th}} \tag{6.10}$$

For example. With $V_0 = 2(V)$, $R_m = R_L = 10K\Omega$, the rise in temperature, $T_m - T_0$, would be only 2.5^0K. This approach is based on assuming that the rise in temperature is totally due to the power dissipated of the pulse bias current at the resistance of detector, i.e. $\Delta T = P / K_{th}$; this is reasonable since the pulses are of short duration.

The calculated noise voltages and D^* with a pulse bias and $R_m = R_L = 10K\Omega$ are shown in Fig. 6.5.

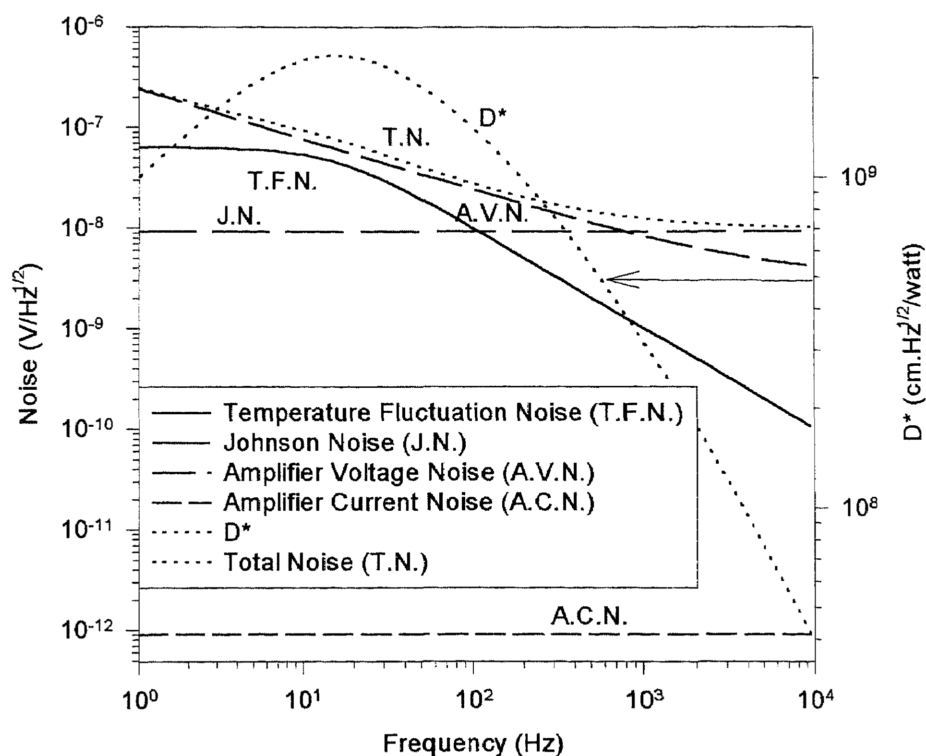

Fig. 6.5 Calculated noise voltages and D^* when pulse bias was used and $R_m = R_L = 10K\Omega$.

The data show that with pulse bias, Johnson noise is no longer dominant, and amplifier voltage noise becomes the major limiting mechanism for frequency below 700 Hz. Therefore, there is a significant advantage to using bipolar preamplifiers because of their lower voltage noise characteristic as described in chapter 3. The noise source values of BJT are strongly dependent on collector currents as shown in Fig. 6.6. It is difficult to estimate the noise values without considering a particular circuit design. From Eq. 6.1, the responsivity, R_V, is linearly proportional to bias current. Therefore, the R_V can be increased by using a larger bias current. However, a larger bias current results in a larger amplifier noise and a rise in the detector's temperature. Therefore, readout integrated circuitry is critical for low noise and high performance bolometer detectors.

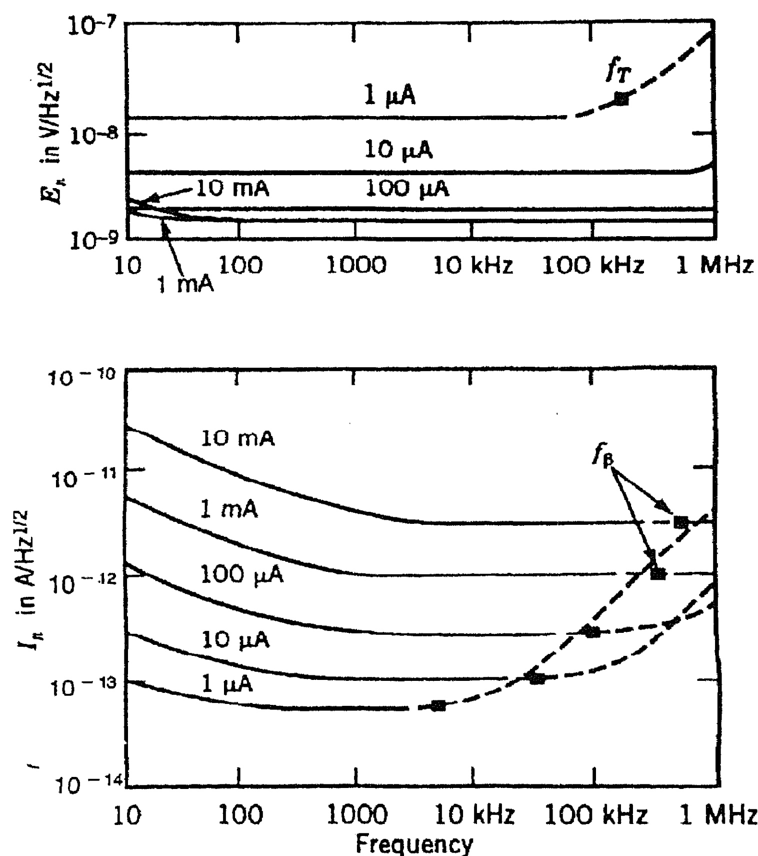

Fig. 6.6 E_n and I_n of a 2N4250 transistor with different collector currents. (From [20])

From the above discussion, the requirements for high performance bolometer detectors are:

- Good thermal isolation structure with low thermal conductance, K_{th}
- Low noise BJT or BiMOS preamplifier
- Material with high TCR and low resistivity

6.2 The Performance of Pyroelectric and Ferroelectric Detectors

As discussed in chapter 4, the voltage responsivity (R_V), the temperature fluctuation noise (V_T), the Johnson noise of load resistance (V_{JL}) and dielectric loss noise (V_{Jd}) of both pyroelectric and ferroelectric detectors, as described in Eqs. 4.11, 4.21, 4.25 and 4.24, are

$$R_V = \frac{C_d}{(C_d + C_p)} \frac{\eta\omega p' A_{pixel}}{K_{th} G_E (1+\omega^2\tau_{th}^2)^{1/2} (1+\omega^2\tau_E^2)^{1/2}}$$
$$= \frac{C_d}{(C_d + C_p)} \frac{\eta\omega p' A_{pixel} R_L}{K_{th}(1+\omega^2\tau_{th}^2)^{1/2}\left[(1+\omega R_L C_d \tan\delta)^2 + \omega^2 R_L^2 (C_d + C_p)^2\right]^{1/2}}, \quad (6.11)$$

$$V_T = \left(\frac{R_V}{\eta}\right)(4k_B T^2 K_{th})^{1/2} \quad (V / Hz^{1/2}), \quad (6.12)$$

$$V_{JL} = \left(\frac{4k_B T R_E^2}{R_L(1+\omega^2\tau_E^2)}\right)^{1/2}$$
$$= \frac{(4k_B T R_L)^{1/2}}{\left((1+\omega R_L C_d \tan\delta)^2 + (R_L\omega(C_d + C_L))^2\right)^{1/2}}, \quad (6.13)$$

$$V_{Jd} = \left(\frac{4k_B T\omega C_d \tan\delta}{(G_E^2 + \omega^2 C_E^2)}\right)^{1/2}$$
$$= \frac{(4k_B T\omega C_d R_L^2)^{1/2}}{\left((1+\omega R_L C_d \tan\delta)^2 + (R_L\omega(C_d + C_L))^2\right)^{1/2}}, \quad (6.14)$$

$$V_J = (V_{JL}^2 + V_{Jd}^2)^{1/2} = \left(\frac{4k_B T R_E}{1+\omega^2 \tau_E^2}\right)^{1/2}$$

$$= \frac{\left(4k_B T R_L\right)^{1/2} * \left(1+\omega R_L C_d \tan\delta\right)^{1/2}}{\left[\left(1+\omega R_L C_d \tan\delta\right)^2 + \omega^2 R_L^2 (C_d + C_p)^2\right]^{1/2}} \quad (V / Hz^{1/2}) \tag{6.15}$$

where $R_E = G_E^{-1} = \dfrac{R_L}{1+\omega R_L C_d \tan\delta}$, $\tau_{th} = C_{th}/K_{th}$ and $\tau_E = (C_d + C_p) R_E$.

The responsivity contains an attenuation factor of $C_d / (C_d + C_p)$ to include the parasitic capacitance, C_p, in circuit elements.

MOSFETs should be used in the preamplifiers design because their high input impedance can be matched to the high impedance of pyroelectric and ferroelectric detectors. The equivalent noise sources I_n and E_n for MOSFET devices given in Eqs. 6.4 and 6.5 are used to write the equation for the total noise of a pyroelectric or ferroelectric detector as

$$V_{tot} = \left(V_T^2 + V_J^2 + E_n^2 + I_n^2 |Z|^2\right)^{1/2} \quad (V / Hz^{1/2}) \tag{6.16}$$

where

$$Z = R_E + \frac{1}{j\omega (C_d + C_p)}$$

Using the above derived equations, the noise values and D^* were calculated using the best typical published values in Table 6.2 for pyroelectric and ferroelectric detectors. These values are used in the following discussions if particular values are not mentioned.

Table 6.2. Detector and Material properties for pyroelectric and ferroelectric detectors.

	Pyroelectric Detector [1]	Ferroelectric Detector [2]
Thermal conductance, K_{th}, $(W/^0K)$	$5*10^{-7}$	$5*10^{-7}$
Thermal capacitance, C_{th}, $(J/^0K)$ [3]	$6.3*10^{-9}$	$6.12*10^{-9}$
Absorber efficiency, η	0.8	0.8
Pixel area, A_{pixel}, (um^2)	$50*50$	$50*50$
Substrate temperature, T, (^0K)	300	300
Pixel thickness, d, (um)	0.36	0.36
Bias resistance, R_L, (Ω)	10^{10}	10^{10}
Amplifier current noise, I_n, $(A/Hz^{1/2})$	$1.8*10^{-16}$	$1.8*10^{-16}$
V_a, $(V/Hz^{1/2})$	$3.4*10^{-9}$	$3.4*10^{-9}$
Z_a, (V)	$2.4*10^{-7}$	$2.4*10^{-7}$
Parasitic capacitance, C_p, (pF) [4]	1	1
Detector capacitance, C_d, (pF)	12.3	430.2
$\tan\delta$	$2*10^{-2}$	$2*10^{-3}$
Pyroelectric coefficient, p', (nC/cm^2K)	95	300
Dielectric constant, ε_r	200	7000

[1] The material was sol-gel $PbTiO_3$, selected from D. L. Polla [123].

[2] The material was sol-gel PScT, selected from R. Watton[63].

[3] Assuming,

- The thickness of SiN is 0.5um with specific heat 1330J/Kg.K and density $2.22g/cm^3$ [124].
- The heat capacitance per cm^3 for $PbTiO_3$ is $2.9J/cm^3K$ [123], and is $2.7J/cm^3K$ for PScT[63].

[4] The $C_{gs} \approx 0.173pF$ for a MOSFET with gate area of $10*10\,\mu m^2$ and oxide thickness of $200^0 A$.

The dependence of the performance parameters R_V and D^* on frequency, for three different values of load resistance, R_L, are shown in Fig. 6.7 for a pyroelectric detector (p.d.). For purposes of comparison, similar curves for a ferroelectric detector (f.d.) are shown in Fig. 6.9. Also shown in both figures are curves for the total noise, which controls the dependence of D^* on responsivity. The insert shows how the detector

dielectric capacitance with the effective output resistance of the detector, $[\omega C_d \tan\delta]^{-1}$, in parallel with the preamplifier input impedance, R_L, forms a low pass filter which controls the D^* frequency response, along with the noise spectrum.

From Fig. 6.8, it can be seen that increasing the load resistance can increase the responsivity for frequency below 20Hz; however, the effect tends to saturate at higher load resistance. From Eq. 6.11, it can be seen that if the last term in the bracketed expression in the denominator dominates, R_V will be independent of R_L.

Thus, the condition for saturation, $\omega R_L(C_d + C_p) >> 1$, is normally satisfied until ω is less than $\omega_L = [R_L(C_d + C_p)]^{-1}$. From the curve in Fig. 6.7, this occurs only for chopping frequencies less than 30Hz.

The total noise, which is the sum of Eqs. 6.12 through 6.15, is seen in Fig. 6.7 to decrease with frequency and increasing R_L, showing a saturation effect with R_L at about $10^{10}\Omega$ for the detector values from Table 6.2. Therefore, D^* can be maximized by increasing the chopping frequency up to a value of about 100Hz, at which the frequency dependence of responsivity, due to the low pass filter, drives D^* down.

Comparing the curves for the f.d. in Fig. 6.8 with the p.d. curves, it can be seen that R_V has a similar corner frequency of about 10Hz, except for the $R_L = 10^9\Omega$ curve of the p.d.; However, the R_V response is independent of R_L. The D^* curves do, however, depend on R_L values as does the total noise which begins to saturate at a similar R_L load as for the p.d. The dependence of R_V on R_L is basically due to the much larger detector capacitance and the lower loss tangent for ferroelectrics. Table 6.2 shows that the dielectric constant is typically 35 times bigger and the loss tangent ten times smaller. Thus

the condition for saturation is easily satisfied for all ω and R_V can not be improved by increasing the impedance of the preamplifier. However, because the total noise is dependent on R_L, as shown in the Fig. 6.8, the D^* can be significantly improved at low frequencies up to the frequency for maximum D^*. For f.d., R_V is nearly inversely proportional to C_d as shown by the following equation easily obtained from Eq. 6.11.

$$R_V \cong \frac{C_d}{(C_d + C_p)^2} \frac{\eta p' A_{pixel}}{K_{th}(1+\omega^2\tau_{th}^2)^{1/2}} \tag{6.17}$$

To compare the various noise components and their dependence on R_L, Figs. 6.9 and 6.10 were prepared for p.d. and f.d. respectively. It can be observed that the dielectric loss noise, V_{Jd} , Johnson noise V_{JL} of the R_L and the total noise can be decreased by increasing the load resistance. This can also be seen from the Eqs. 6.18a and 6.18b below,

$$V_{Jd} = \left[\frac{4k_B T}{R_d}\right]^{1/2} \frac{R_E}{(1+\omega^2\tau_E^2)^{1/2}} \tag{6.18a}$$

$$V_{Jd} = \left[\frac{4k_B T}{R_L}\right]^{1/2} \frac{R_E}{(1+\omega^2\tau_E^2)^{1/2}} \tag{6.18b}$$

where $$R_E = \frac{R_d R_L}{R_d + R_L} = \frac{1}{\dfrac{1}{R_L} + \dfrac{1}{R_d}} = \frac{1}{\dfrac{1}{R_L} + \omega C_d \tan\delta} = \frac{R_L}{1 + \dfrac{\omega}{\omega_l}}$$

with $$\omega_l \equiv \frac{1}{R_L C_d \tan\delta}$$

Since $\dfrac{V_{JL}}{V_{Jd}} = \left(\dfrac{R_d}{R_L}\right)^{1/2}$, $V_{JL} > V_{Jd}$ if $R_d < R_L$ and $V_{Jd} > V_{JL}$ if $R_L < R_d$. For small ω, R_d tends to be greater than R_L and V_{JL} greater than V_{Jd}, as observed in Fig. 6.9 for

the p.d. For $R_L = 10^{11}$, the dielectric loss noise dominates for practical chopping frequencies.

In the case of ferroelectric detectors, the larger values for C_d results in much lower values for R_d and thus R_E, V_{Jd}, and V_{JL}. Thus amplifier noise dominates for $f > 50Hz$ for an R_L value of 10^9 and for much lower f for the larger load resistors. Thus, selecting high input impedance preamplifier can significantly improve the performance of f.d., while being of less importance for p.d. It should also be noted that the dielectric loss noise is not a function of R_L for f.d. because of the relatively large value for τ_E due to the large value for C_d. Thus the equation for V_{Jd} can be written as in Eq. 6.19, with the parasitic capacitance C_p added to C_d.

$$V_{Jd} = \left[\frac{4k_B T}{R_d}\right]^{1/2} \frac{1}{\omega(C_d + C_p)}; \quad R_d = \frac{1}{\omega C_d \tan\delta} \tag{6.19}$$

Since for f.d., the parasitic capacitance should be relatively small verses C_d, V_{Jd} can be written as in Eq. 6.20a and similarly for V_{JL} in Eq. 6.20b.

$$V_{Jd} \approx \left(\frac{4k_B T \tan\delta}{\omega C_d}\right)^{1/2} \tag{6.20a}$$

$$V_{Jd} \approx \left(\frac{4k_B T}{R_L}\right)^{1/2} \frac{1}{\omega(C_d + C_p)} \approx \left(\frac{4k_B T}{R_L}\right)^{1/2} \frac{1}{\omega C_d} \tag{6.20b}$$

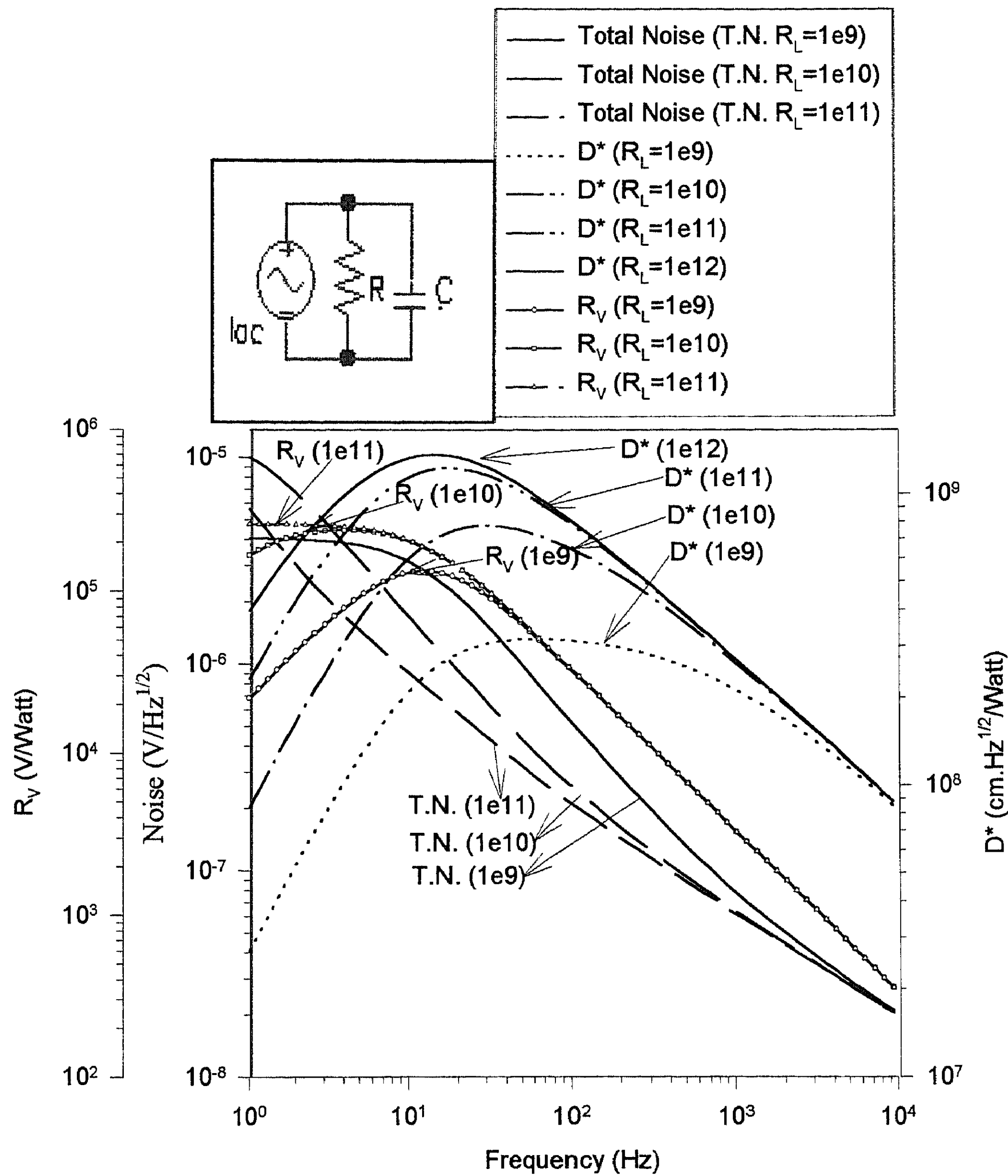

Fig. 6.7 Total noise voltage, R_V and D^* of a pyroelectric detector with bias resistance $R_L = 10^9\,\Omega$, $10^{10}\,\Omega$ and $10^{11}\,\Omega$. The D^* for $R_L = 10^{12}\,\Omega$ is shown. Equivalent circuit of a detector is also shown.

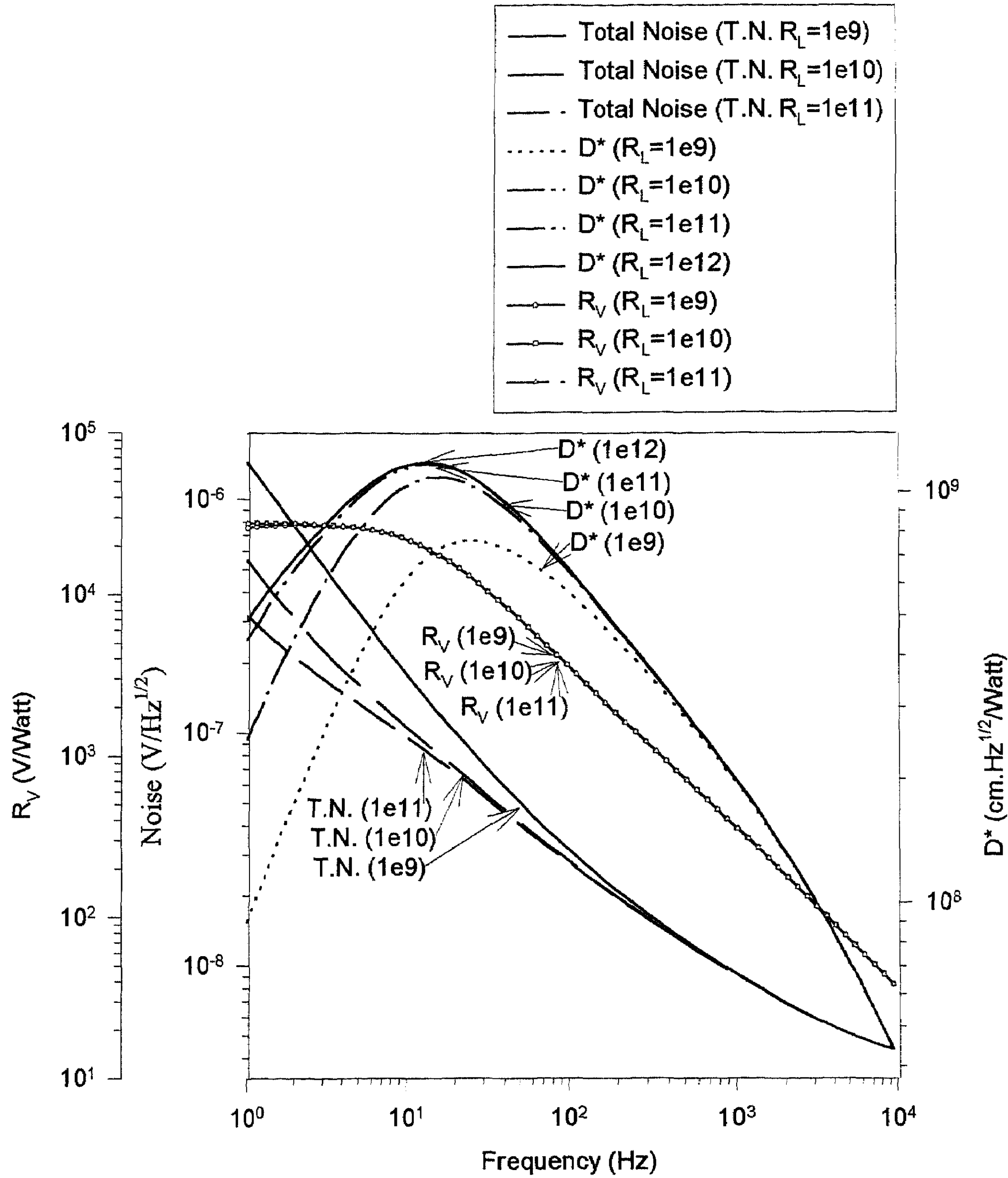

Fig. 6.8 Total noise voltage, R_V and D^* for a ferroelectric detector with bias resistance $R_L = 10^9\,\Omega$, $10^{10}\Omega$ and $10^{11}\Omega$. The D^* for $R_L = 10^{12}\Omega$ is shown. The responsivities are superimposed in this figure.

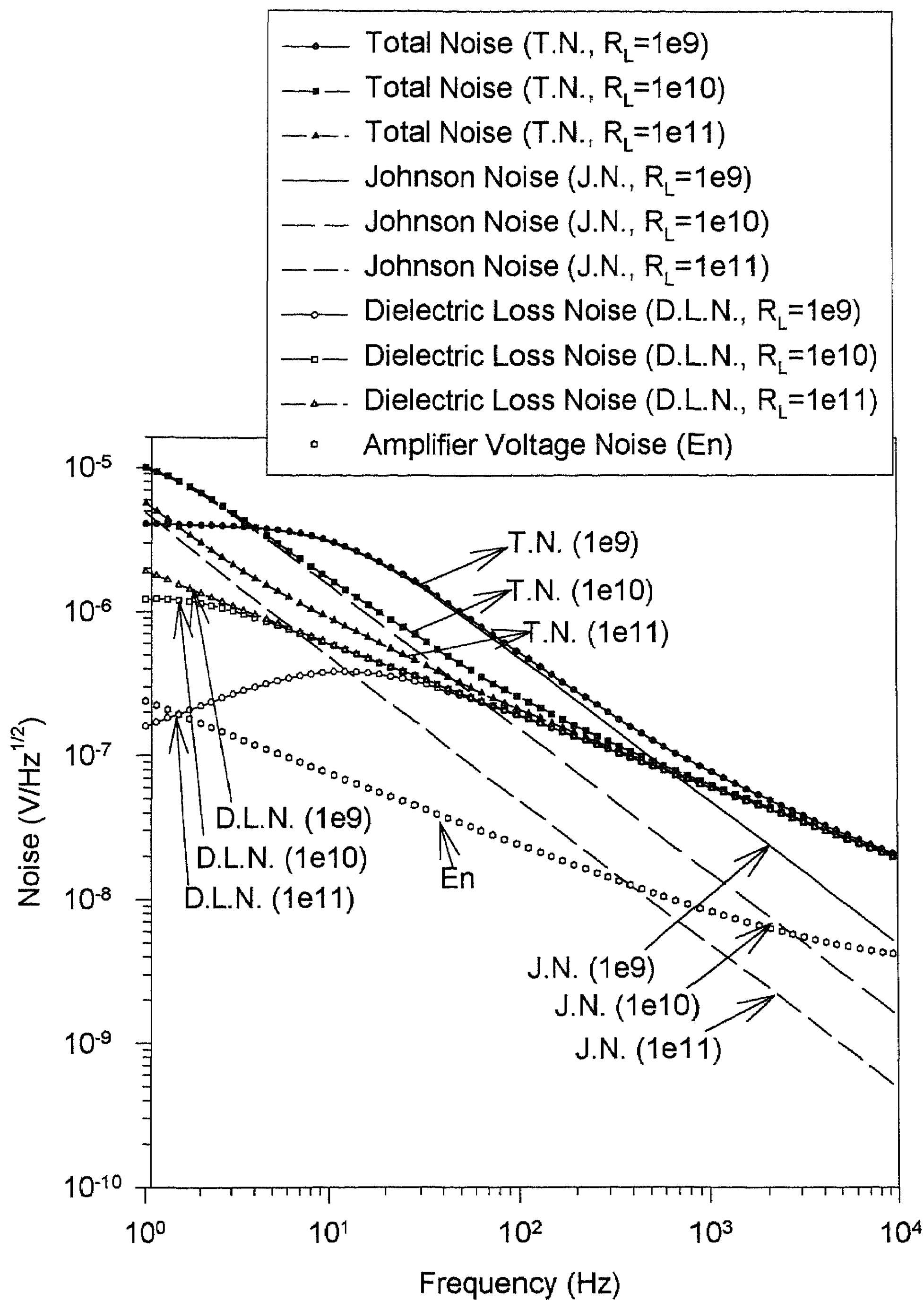

Fig. 6.9 Total noise voltage, Johnson noise and dielectric loss noise for a pyroelectric detector with bias resistance $R_L = 10^9\Omega$, $10^{10}\Omega$ and $10^{11}\Omega$.

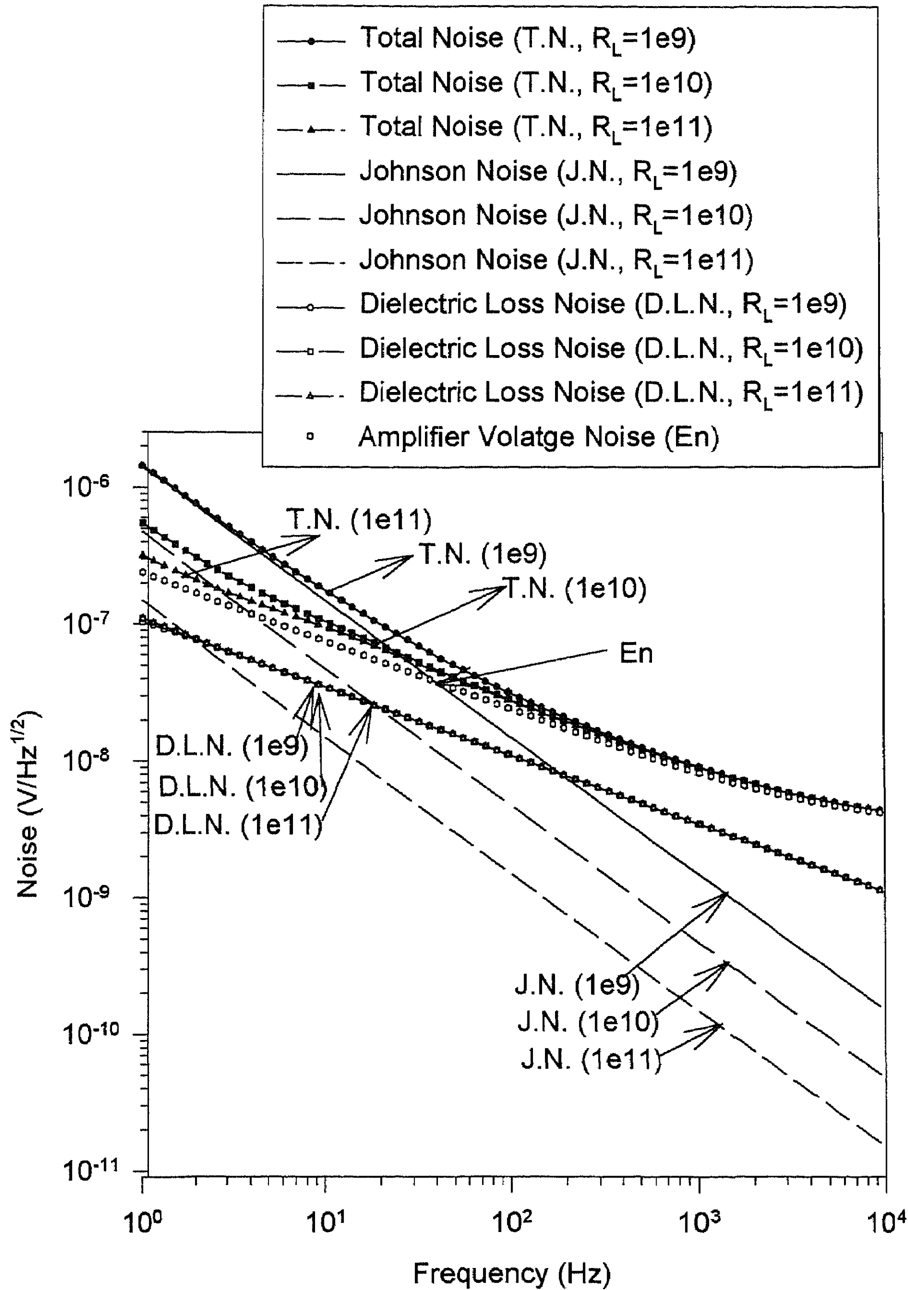

Fig. 6.10 Total noise voltage, Johnson noise and dielectric loss noise for a ferroelectric detector with bias resistance $R_L = 10^9\Omega$, $10^{10}\Omega$ and $10^{11}\Omega$.

In Figs. 6.11 and 6.12 are shown the dependence of the various noise sources and the total noise on frequency for a pyroelectric and a ferroelectric detector respectively. The load resistance chosen for these figures was $10^{11}\Omega$, a value at which D^* does not improve much with further increasing in load resistance. For the pyroelectric detector, the dielectric loss noise, D.L.N., dominates over the other noise sources except for frequencies less than 10Hz, where the Johnson noise of the load resistance becomes larger. For practical frequencies greater than about 60Hz, the total noise is almost entirely due to D.L.N. and even for the frequency at which D^* is maximum, 20Hz, D.L.N. plays the major role in determining detector performance. This is no longer the case, if materials with smaller loss tangent are used as shown in Fig. 6.13 for a $\tan\delta$ value one tenth the value used in Fig. 6.11. For such a pyroelectric material, the thermal fluctuation noise, T.F.N., is larger than the D.L.N. for frequencies less than 100Hz. The maximum value for D^* is seen to increase by about two times when compared with the D^* curve from Fig. 6.11. The full potential of the detector is realized when the total noise is due to T.F.N. with the other noise sources suppressed. Note that typical value for the amplifier voltage and current noise sources are not influential in determining the performance of pyroelectric detectors. This is not the case for ferroelectric detector as shown in Fig. 6.12. Note that for all frequencies, the total noise is nearly identical to the amplifier voltage noise, A.V.N., and that the T.F.N. maximum value of $5*10^{-8}(V/Hz^{1/2})$ is much less than for pyroelectric detectors, $5*10^{-7}(V/Hz^{1/2})$, for the same R_L. Thus, there is the possibility of improving the D^* of ferroelectric detectors by utilizing advances in amplifier technology while this is not the case for pyroelectric detectors. Such an improvement is

illustrated by the curves in Fig. 6.14 where the A.V.N. due to the amplifier flicker noise is reduced from a value of $2.4*10^{-7}(V)$ to a value of $7.59*10^{-8}(V)$, and $\tan\delta$ is also reduced from $2*10^{-3}$ to $1*10^{-3}$. This results in T.F.N. dominating over A.V.N. for frequencies less than about 70Hz. Note that the maximum value of D^* rises by about 40 percent and at 100Hz is $1*10^9$ versus $7*10^8$ for the poorer amplifier.

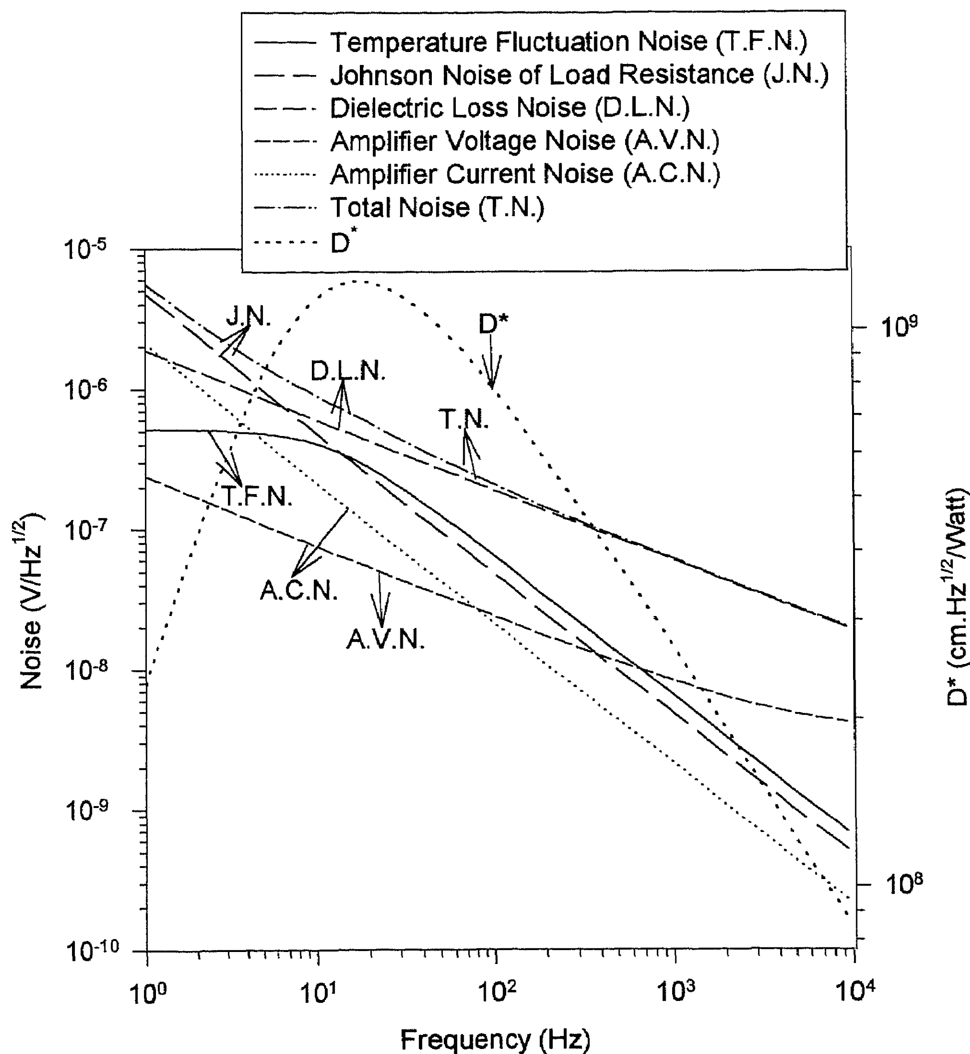

Fig. 6.11 Calculated noise voltages and D^* for a pyroelectric detector with $R_L = 10^{11}\Omega$ and $\tan\delta = 2*10^{-2}$.

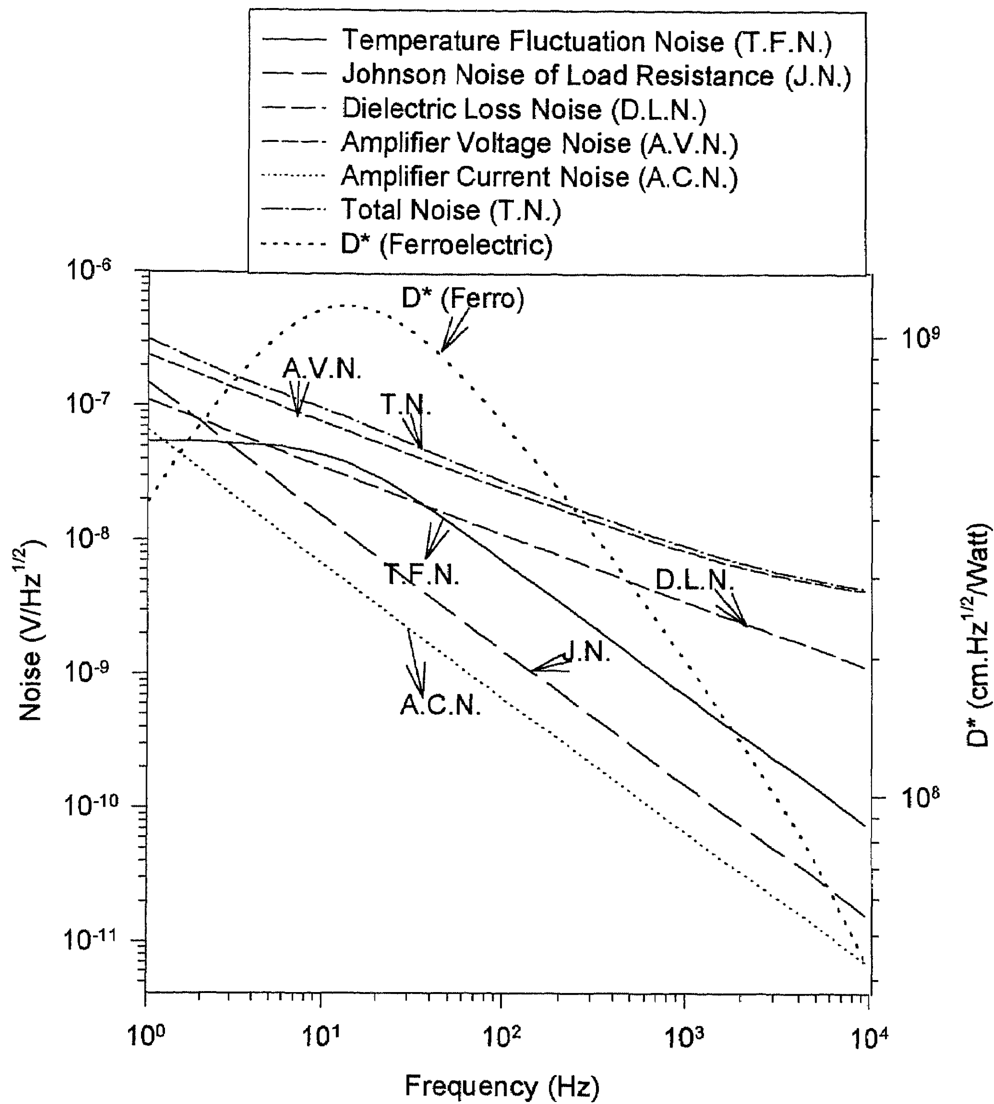

Fig. 6.12 Calculated noise voltages and D^* for a ferroelectric detector with $R_L = 10^{11}\Omega$ and $\tan\delta = 2*10^{-3}$.

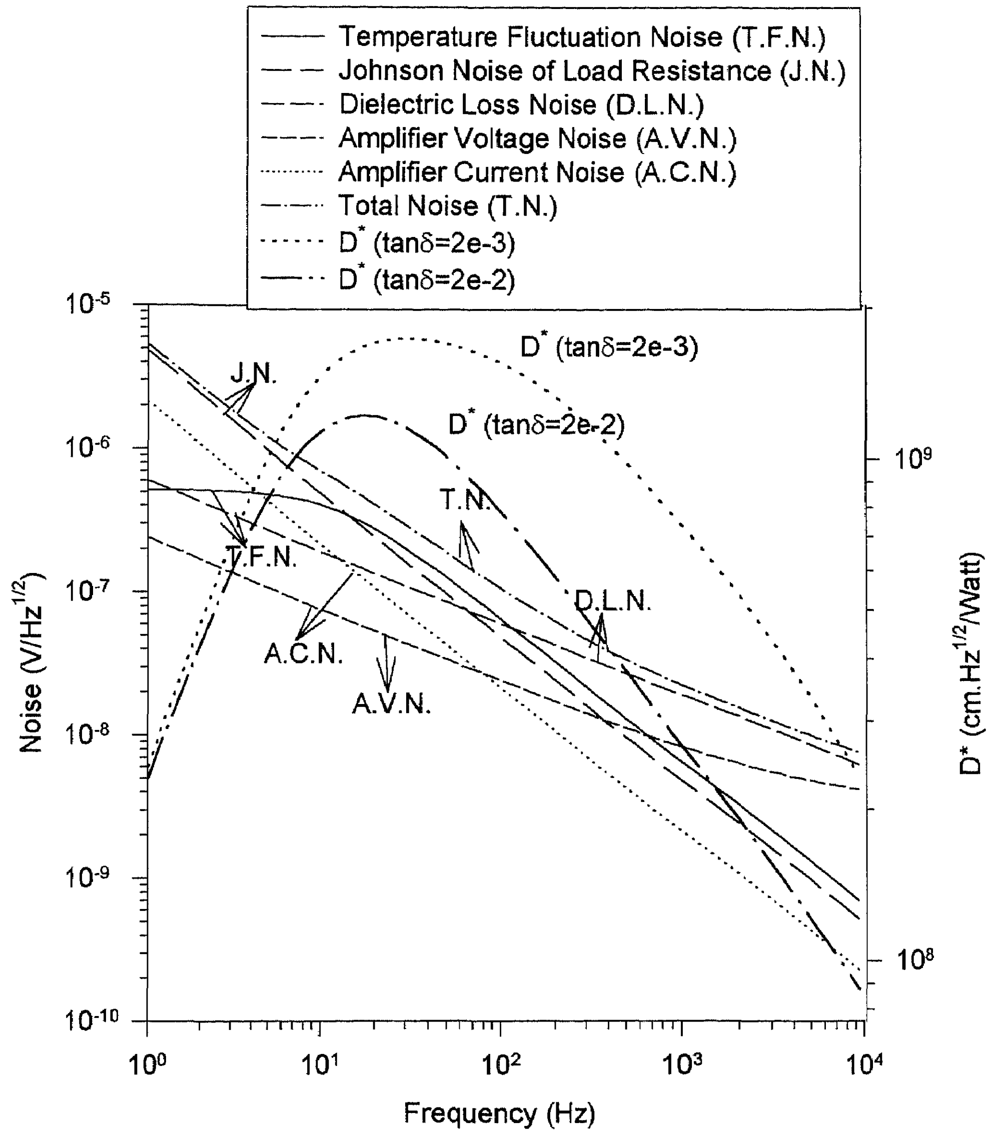

Fig. 6.13 Calculated noise voltages and D^* for a pyroelectric detector with $R_L = 10^{11}\Omega$ and $\tan\delta = 2*10^{-3}$.

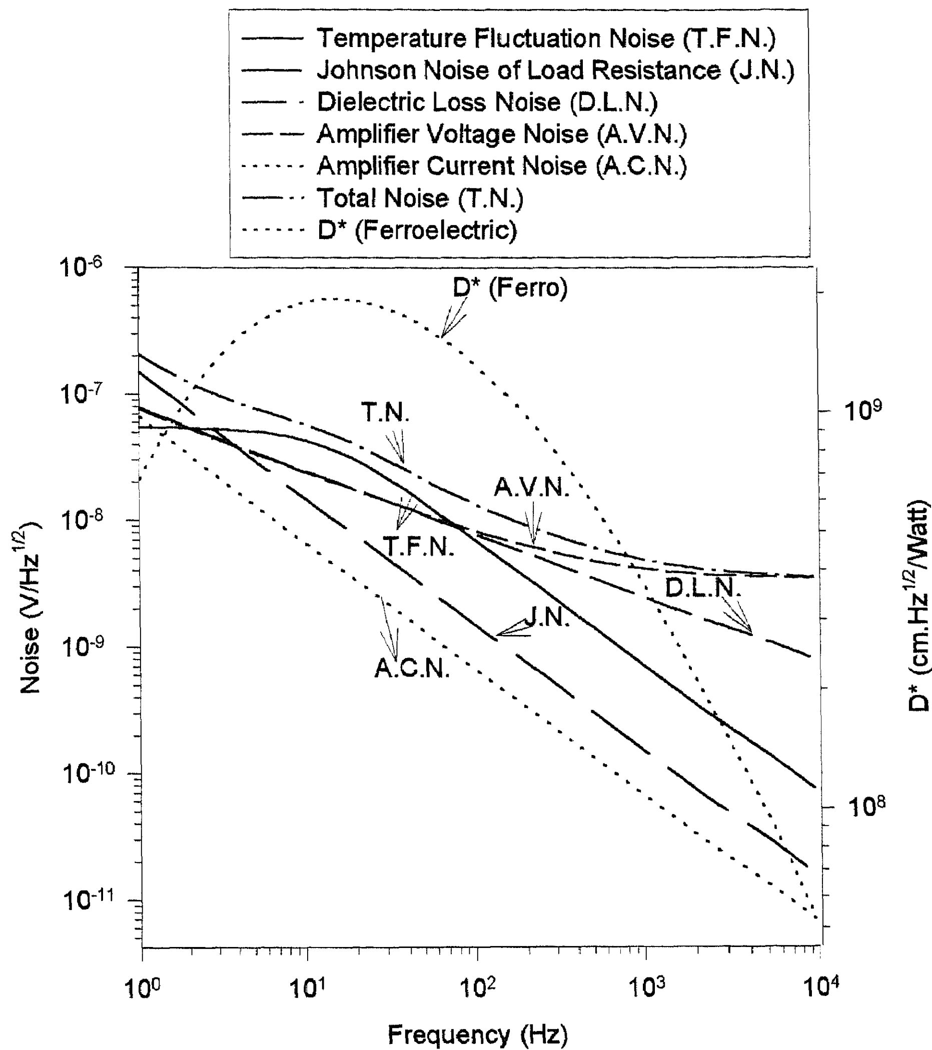

Fig. 6.14 Calculated noise voltages and D^* for a ferroelectric detector with $R_L = 10^{11}\Omega$, $Z_a = 7.59 * 10^{-8}(V)$ and $\tan\delta = 1 * 10^{-3}$.

When the detector becomes limited by thermal fluctuation noise, the only method to improve its performance is to decrease its total conductance as shown in Figs. 6.15 and 6.16 for pyroelectric and ferroelectric detectors respectively. It can be seen that the values used for the previous figures, $5 * 10^{-7}(W/K)$ were nearly optimum because D^* tends to

saturate for K_{th} less than about $4*10^{-7}(W/K)$. Understanding the dependence of D^* on K_{th} can be obtained by examining the equations for D^* and the T.F.N., V_T, when the T.F.N. dominates as occurs in Figs. 6.15 and 6.16 when K_{th} is greater than $4*10^{-7}(W/K)$.

$$D^* = \left(\frac{\eta^2}{4k_B T^2 K_{th}}\right)^{1/2} \tag{6.21}$$

$$V_T = \left(\frac{R_V}{\eta}\right)(4k_B T^2 K_{th})^{1/2} \quad (V/Hz^{1/2}) \tag{6.22}$$

and

$$V_T \propto \frac{1}{\left(K_{th} + \omega^2 \frac{C_{th}^2}{K_{th}}\right)^{1/2}} \tag{6.23}$$

Equation 6.23 explains the rise and fall of the T.F.N. with increasing K_{th} in Figs. 6.15 and 6.16. Note that only the T.F.N. depends on K_{th} and thus the shape of the total noise is the same as for the T.F.N., Thus, total noise can be reduced by decreasing K_{th} only to a value of about $4*10^{-7}W/K$ unless Johnson noise, and dielectric loss noise can be reduced. Fig. 6.17 compares the dependence of D^* on K_{th} for both types of detectors when chopping frequency is taken as a variable. It can be seen that in the lower K_{th} region (K_{th}< 1 to $2*10^{-6}W/K$) decreasing the chopping frequencies improves the performance of both detectors and that the ferroelectric detectors improve more rapidly and surpass the D^* of the pyroelectric detectors at a value less than about 50Hz, the exact value depending on several factors.

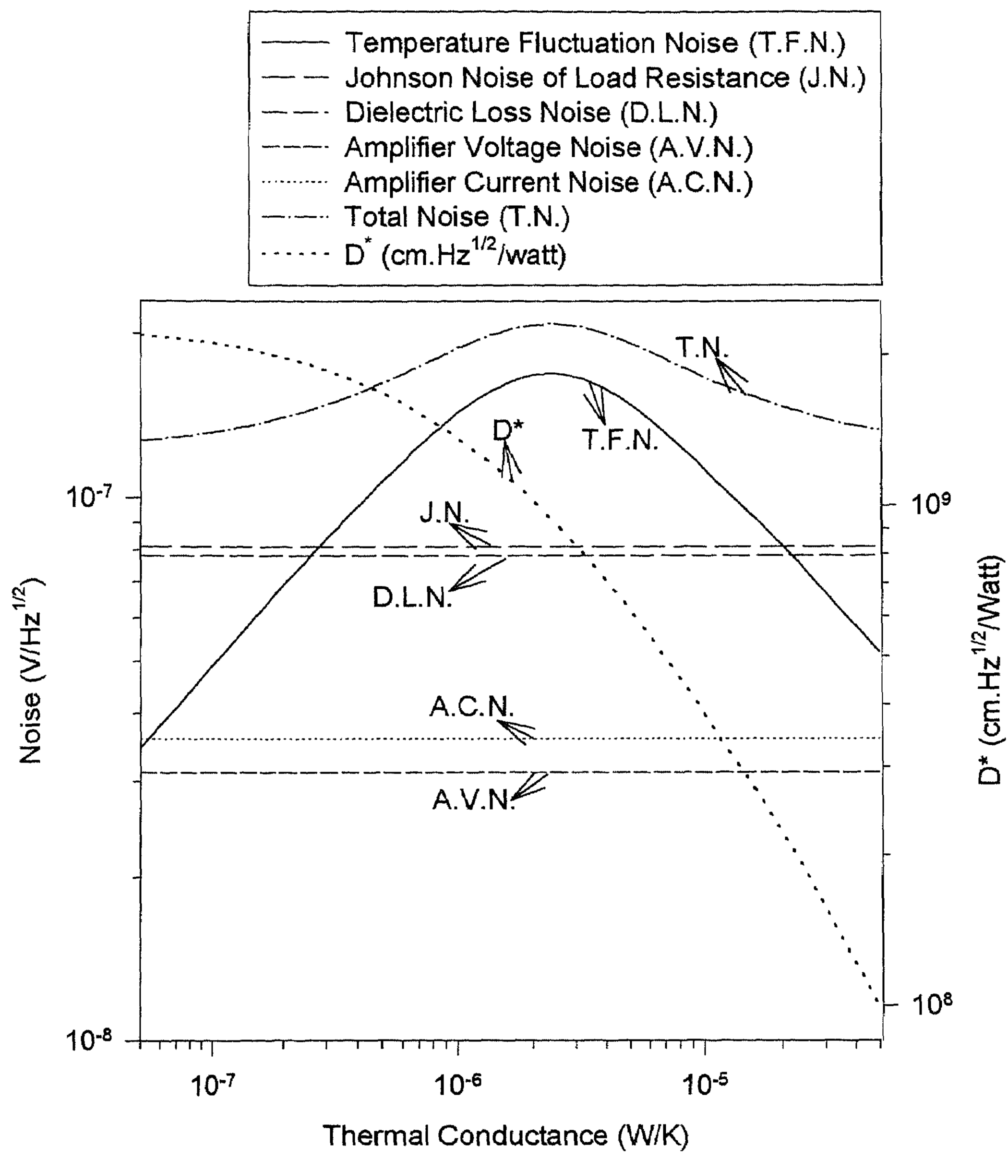

Fig. 6.15 The total noise and D^* vs. thermal conductance for a pyroelectric detector at a frequency of 60Hz with $R_L = 10^{11}\Omega$ and $\tan\delta = 2*10^{-3}$.

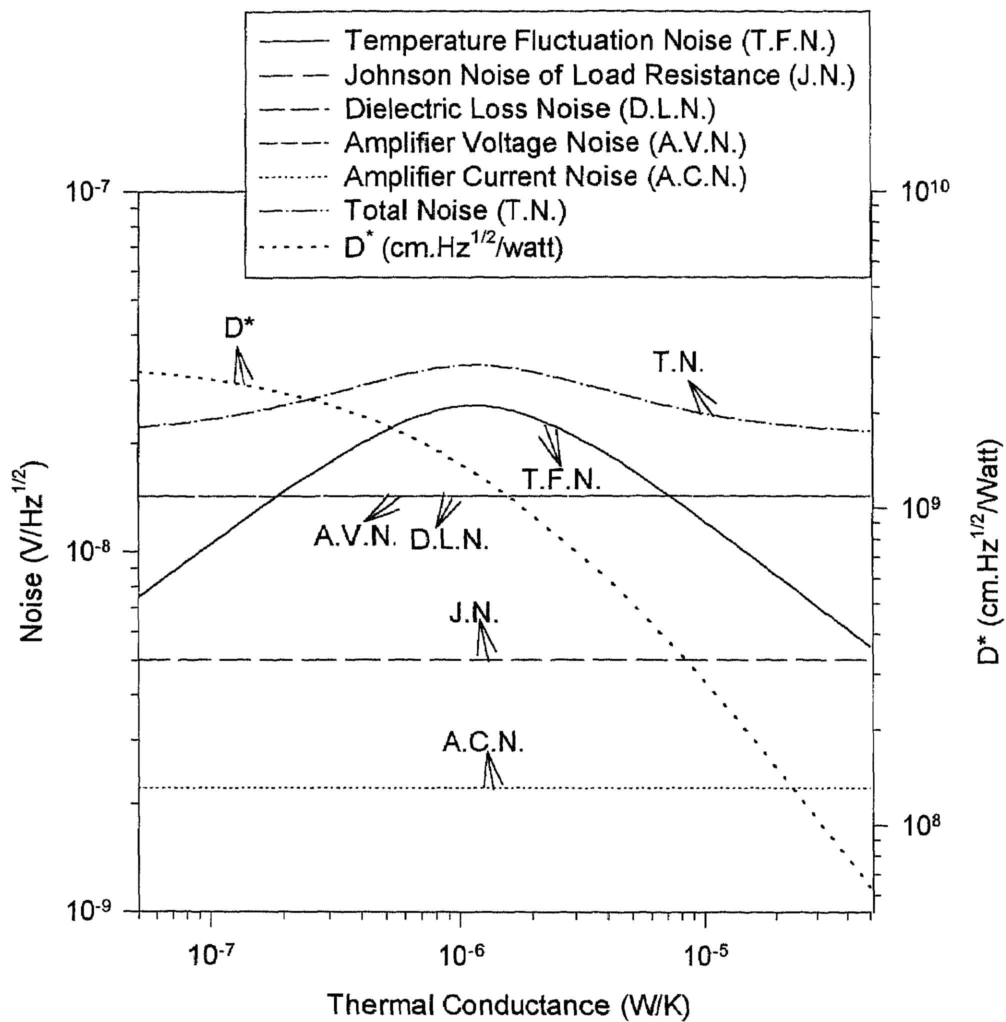

Fig. 6.16 Total noise voltage and D^* vs. thermal conductance for a ferroelectric detector at a frequency of 60Hz with $R_L = 10^{11}\Omega$, $Z_a = 7.59 * 10^{-8}(V)$ and $\tan\delta = 1 * 10^{-3}$.

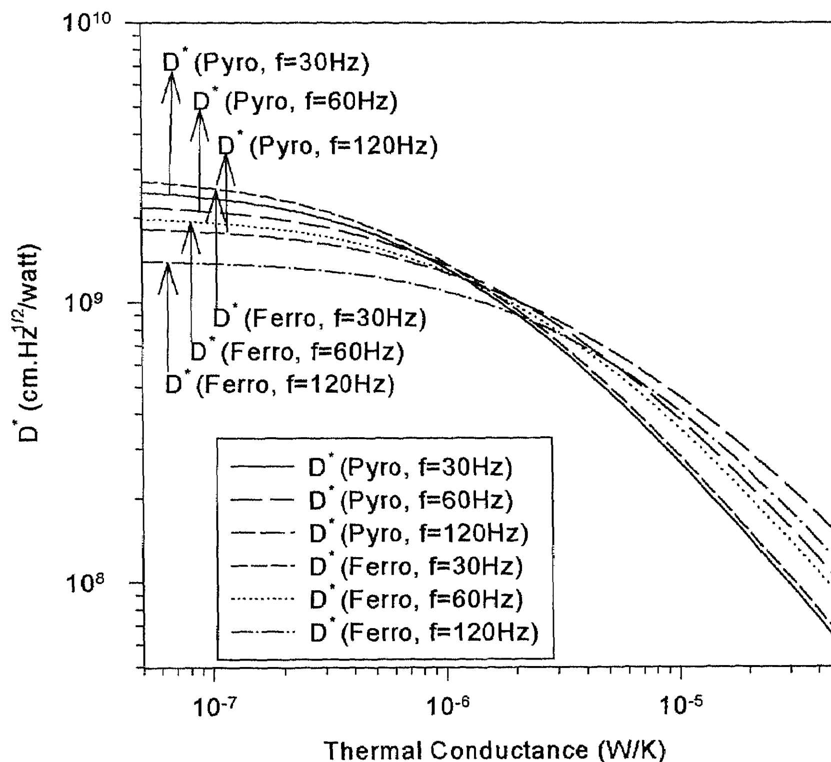

Fig. 6.17 The D^* vs. thermal conductance for both detectors at frequencies 30, 60 and 120Hz with $R_L = 10^{11}\Omega$. $\tan\delta = 2*10^{-3}$ for a pyroelectric detector; $Z_a = 7.59*10^{-8}(V)$ and $\tan\delta = 1*10^{-3}$ for a ferroelectric detector.

A key parameter for improving the D^*, particular for ferroelectric detectors, is the thickness of the detector. Low cost detectors must be mass fabricated using thin film technology. Control of film thickness is dependent on advances in thin film processing technology. Although it is not certain that anticipated desired improvements can be obtained, it is interesting to study the benefits that can be obtained by controlling C_d, which depends inversely on detector thickness, as illustrated by the D^* versus film thickness data in Fig. 6.18. Since R_L effects the dependence, three difference values of

10^9, 10^{10}, and $10^{11}\Omega$ were used and the reasonable values of $\tan\delta = 2*10^{-3}$ and $1*10^{-3}$ for the p.d. and f.d. were selected respectively. To recall the low pass filter effect of C_d, the equivalent circuit is shown in the insert, where R is to include the output resistance of the detectors in parallel with R_L. In the case of the pyroelectric detectors, Johnson noise is dominant for $R_L = 10^{-9}\Omega$, as shown in Fig. 6.9. Therefore, D^* can be expressed approximately by equation 6.24, which shows that D^* is inversely proportional to the thermal capacitance C_{th} for frequencies greater than the thermal time constant $R_{th}C_{th}$.

$$D^* \approx \frac{R_V A_{pixel}^{1/2}}{V_J} = \frac{C_d}{(C_d + C_p)} \frac{\eta\omega p' A_{pixel}^{3/2} (R_L)^{1/2}}{K_{th}(1+\omega^2\tau_{th}^2)^{1/2}(4k_B T)^{1/2}(1+\omega R_L C_d \tan\delta)^{1/2}}$$

$$\approx \frac{C_d}{(C_d + C_p)} \frac{\eta\omega p' A_{pixel}^{3/2} (R_L)^{1/2}}{K_{th}(1+\omega^2\tau_{th}^2)^{1/2}(4k_B T)^{1/2}}, \text{ at a chopping frequency 60Hz} \qquad (6.24)$$

The thermal capacitance which rises with film thickness, as shown for both detectors in Fig. 6.18, thus drives D^* of the pyroelectric detector down as the film thickness increases. The major improvement in D^* is obtained by increasing R_L. At high R_L, the temperature fluctuation noise is dominant, and D^* can be improved only by decreasing K_{th}. Thus, D^* is less dependent on film thickness at the higher values of R_L ($10^{11}\Omega$). In contrast to the pyroelectric detector, the D^* of ferroelectric detectors can be noticeable improved by increasing the film thickness for load resistance larger than about $5*10^9\Omega$, if the film thickness is less than 0.5um. This is because the amplifier noise dominated over the other noise sources which are shunted by C_d. Further increases in D^* with detector thickness above 0.5um does not occur because in this region T.F.N. dominates and this noise source is independent of C_d and thus film thickness.

In general, D^* is seen to be dependent on detector thickness for both pyroelectric and ferroelectric detectors. Thus for 2-D detector arrays, a tight tolerance on the thin film manufacturing processing must be maintained to avoid introducing additional noise, fixed pattern noise, due to the variation in thickness of the detectors in the array.

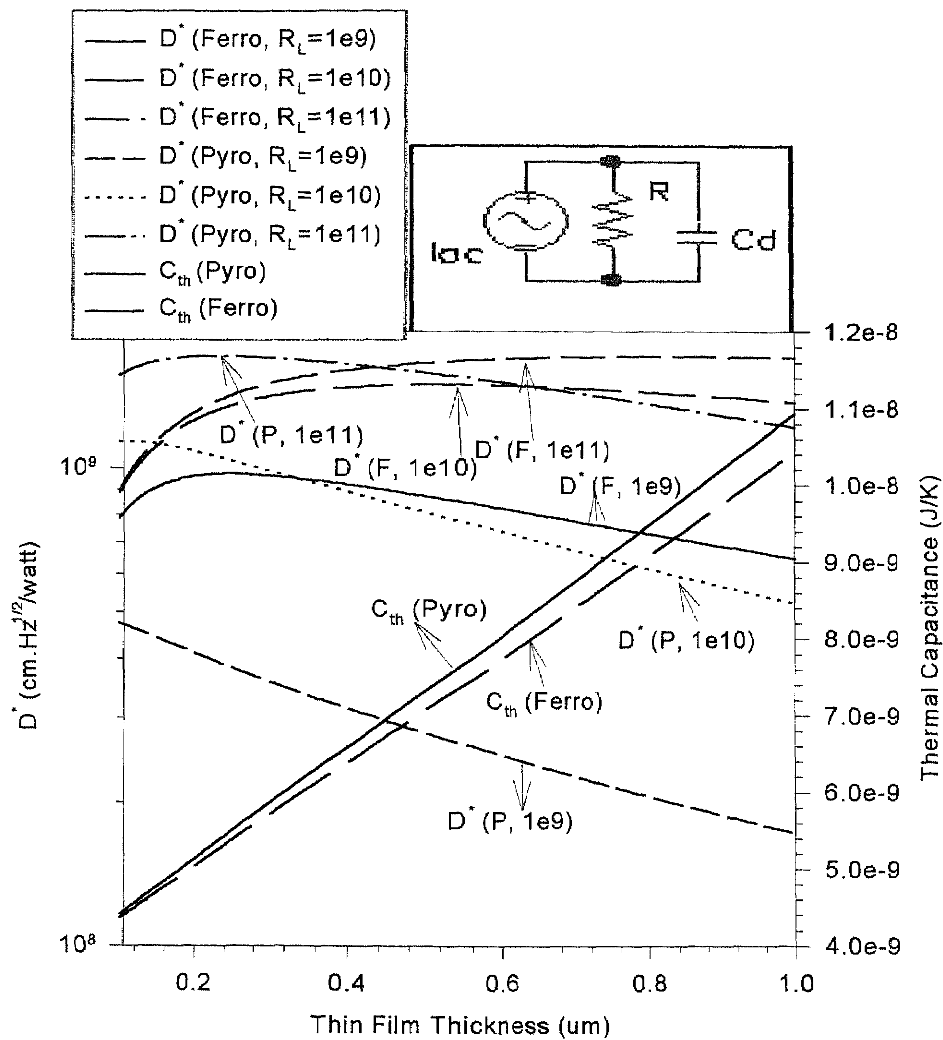

Fig. 6.18 D^* vs. thin film thickness for a pyroelectric and ferroelecric detectors at a chopping frequency 60 Hz with $R_L = 10^9\Omega$, $10^{10}\Omega$ and $10^{11}\Omega$. $\tan\delta = 2*10^{-3}$ for a pyroelectric detector; $Z_a = 7.59*10^{-8}(V)$ and $\tan\delta = 1*10^{-3}$ for a ferroelectric detector.

It is interesting to study the possible effect that dielectric constant changes would have on D^* for both p.d. and f.d.. Fig. 6.19 plots calculated D^* values versus dielectric constant for a chopping frequency of 60Hz and the same R_L values of 10^9, 10^{10}, and $10^{11}\Omega$. Note that only the pyroelectric detectors improve with increasing dielectric constant and this is only for the R_L values of 10^9 and 10^{10}, which yield inferior D^*. For the ferroelectric detectors, D^* actually deteriorates slightly with increasing dielectric constant. This is because in the chopping frequency region where D^* is maximum, e.g. 60Hz, the T.F.N. is dominant. As discussed previously to achieve maximum D^*, the detector should be designed so that the total noise is controlled by the thermal fluctuation noise, which is independent of C_d. D^* decreases only slightly when Johnson noise is dominant because the decrease in R_V with increasing C_d is balanced by a decrease in the Johnson noise with increasing C_d. Improvements in D^* with increases in the pyroelectric coefficient (P.C.) might be expected and thus the dependence of the noise voltage values and D^* on values for P.C. were studied using computer calculations plotted in Figs. 6.20 and 6.21 for p.d. and f.d. respectively. It is easily seen that when T.F.N. is not dominant, D^* increases with P.C., actually linearly for both detectors. However, when T.F.N. becomes more dominant, at higher values of P.C., the improvement D^* actually saturates. This is particularly true for the f.d., which has somewhat larger D^* values under the conditions chosen. Since it has been shown that maximum values for D^* should be achieved in regions where T.F.N. dominates and since T.F.N. becomes more dominant with increasing P.C., it would seem that a material research effort wined at increasing the

P.C. would yield detectors with higher D^*. The curves in Figs. 6.20 and 6.21 show that D^* continues to increase with increasing P.C. because responsivity depends more strongly on P.C. than the T.F.N., although increases in P.C. above 90 and 600 ($nC/cm^2.K$) for the p.d. and f.d. respectively do not result in significant increases in D^* to be worth the effort. Referring to the values presented in Table 6.2, it is seen that while present-day pyroelectric materials have a value of 95 $nC/cm^2.K$, the best reported values for the P.C. of ferroelectric materials is 300 and thus an improvement in D^* of about 4 to 5 is achievable with improvement in ferroelectric material.

In summary, to realize high D^* performance for pyroelectric and ferroelectric detectors, the following are reasonable goals:

- Good thermal isolation structure with low thermal conductance, K_{th}
- Material with high pyroelectric coefficient, p', low loss $\tan\delta$ and appropriate dielectric constant
- Thicker thin film (>0.5um) for ferroelectric detectors

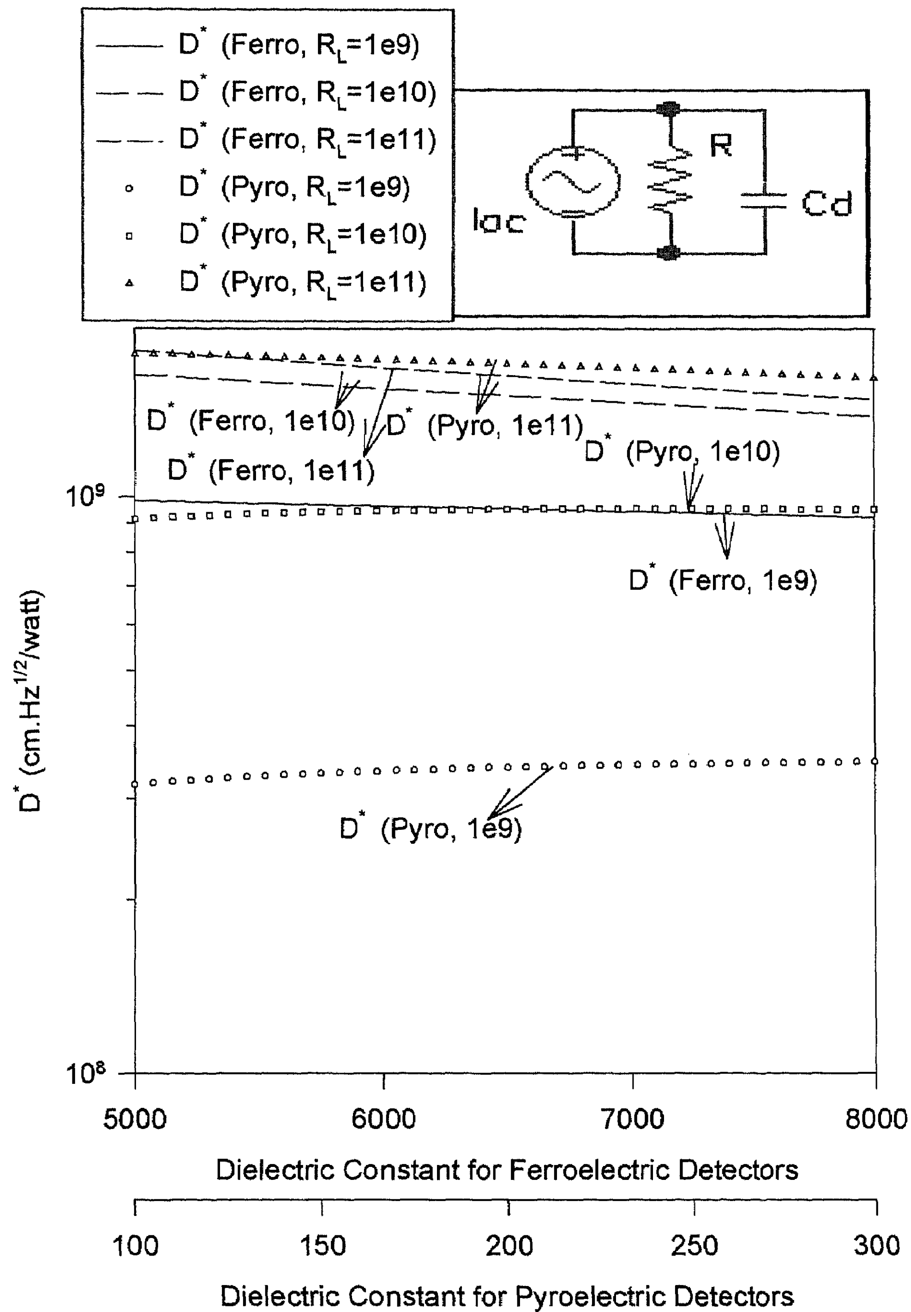

Fig. 6.19 D^* vs. dielectric constant for a pyroelectric and ferroelecric detectors at a chopping frequency 60 Hz. $R_L = 10^{11}\Omega$ and $\tan\delta = 2*10^{-3}$ for the pyroelectric detector. $R_L = 10^{11}\Omega$, $Z_a = 7.59*10^{-8}(V)$ and $\tan\delta = 1*10^{-3}$ for the ferroelectric detector. Equivalent circuit of a detector is also shown.

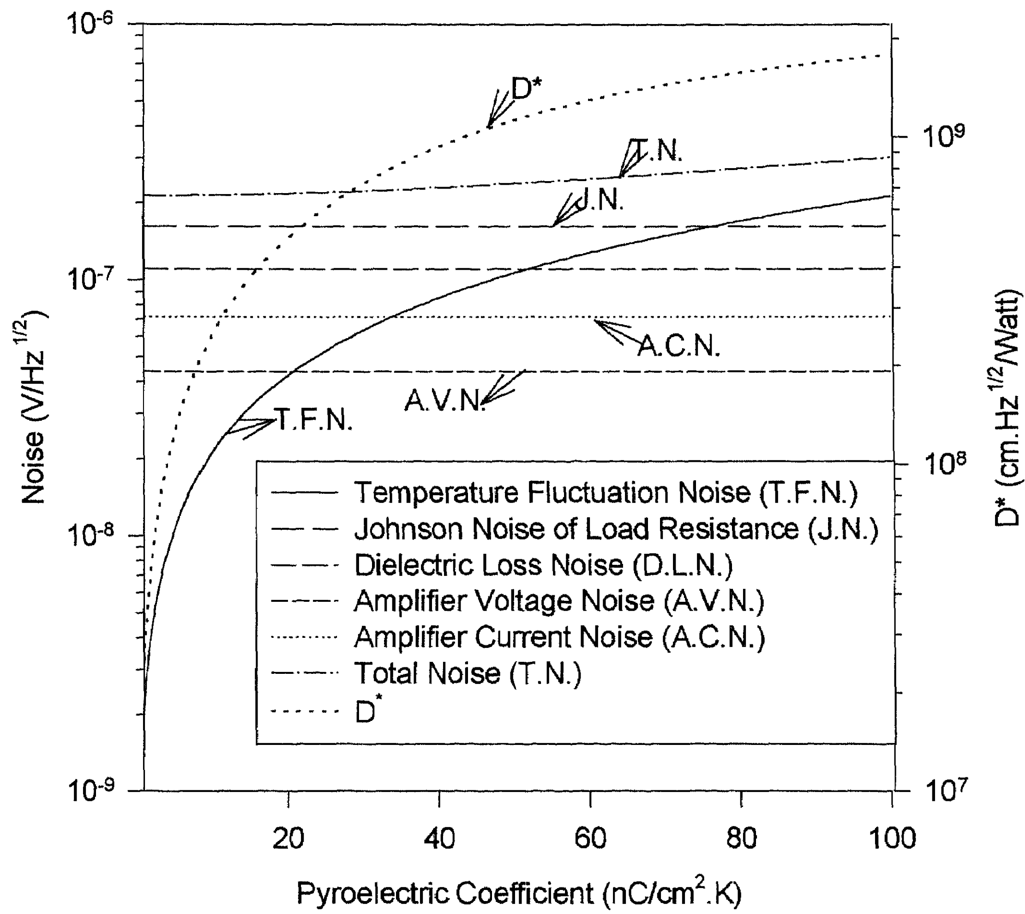

Fig. 6.20 The noise voltages and D^* vs. pyroelectric coefficient for a pyroelectric detector at a chopping frequency 60 Hz with $R_L = 10^{11}\Omega$ and $\tan\delta = 2*10^{-3}$.

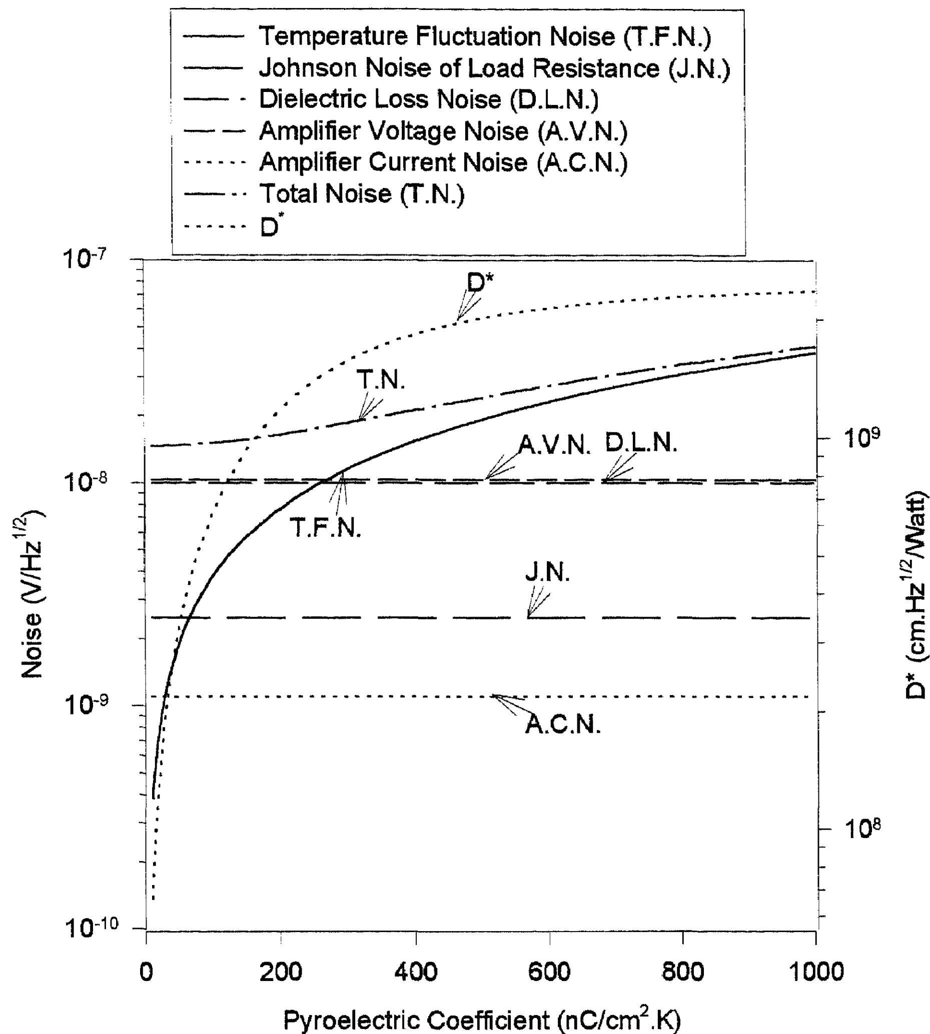

Fig. 6.21 The noise voltages and D^* vs. pyroelectric coefficient for a ferroelectric detector at a chopping frequency 60 Hz with $R_L = 10^{11}\Omega$, $Z_a = 7.59 * 10^{-8}(V)$ and $\tan\delta = 1 * 10^{-3}$.

6.3 Comparison of the Future Performance of Bolometer, Pyroelectric and Ferroelectric Detectors

The calculated performances of bolometer, pyroelectric and ferroelectric detectors are shown in Fig. 6.22. The calculated total noise voltage and D^* of bolometer detector are based on Fig. 6.5 which assumes $R_L = R_a = 10K\Omega$. These are considered to be the best

values that can be made with present-day materials according to results reported in the reference[122]. The calculated total noise voltage and D^* of pyroelectric and ferroelectric detectors are based on Figs. 6.13 and 6.14, where the material properties have been optimized so that the temperature fluctuation noise is dominant in both types of detectors. It was shown that this results in optimum values for D^* and with corresponding response times of about 1.2 seconds for a pyroelectric detector and much greater for a ferroelectric detector. The D^* and total noise voltages of pyroelectric and ferroelectric detectors with present-day (reported) material properties are also plotted for comparison.

It can be seen from the figure that the bolometer detector has higher D^* than that of pyroelectric and ferroelectric detectors at the chopping frequency 60Hz, and also to frequency up to about 90Hz. However, the ferroelectric detector has fundamentally smaller total noise than that of either the bolometer or yroelectric detector because of its high device capacitance. For a 2-D array, the performance is also dependent on the bandwidth of the readout circuit, as described in section 3.3. The calculated D^* of bolometer detectors in this thesis may be overestimated because the best reported D^* is about $5*10^8 cm.Hz^{1/2} / watt$ [122] at a chopping frequency of 60Hz with pixel area 50*50 μm^2. The overestimation could be related to the neglect of the amplifier noise that would be associated with the pulse bias network required for bolometers.

The best estimate of the D^* capability for resistive, pyroelectric and ferroelectric detectors are about $1.72*10^9 cm.Hz^{1/2} / watt$, $1.54*10^9 cm.Hz^{1/2} / watt$ and $1.66*10^9 cm.Hz^{1/2} / watt$ respectively at a chopping frequency of 60Hz. The figure shows that D^* for the both pyroelectric and ferroelectric detectors could be improved by a factor

of about two, based on reasonable estimated possible improvements in material properties as described in previous section.

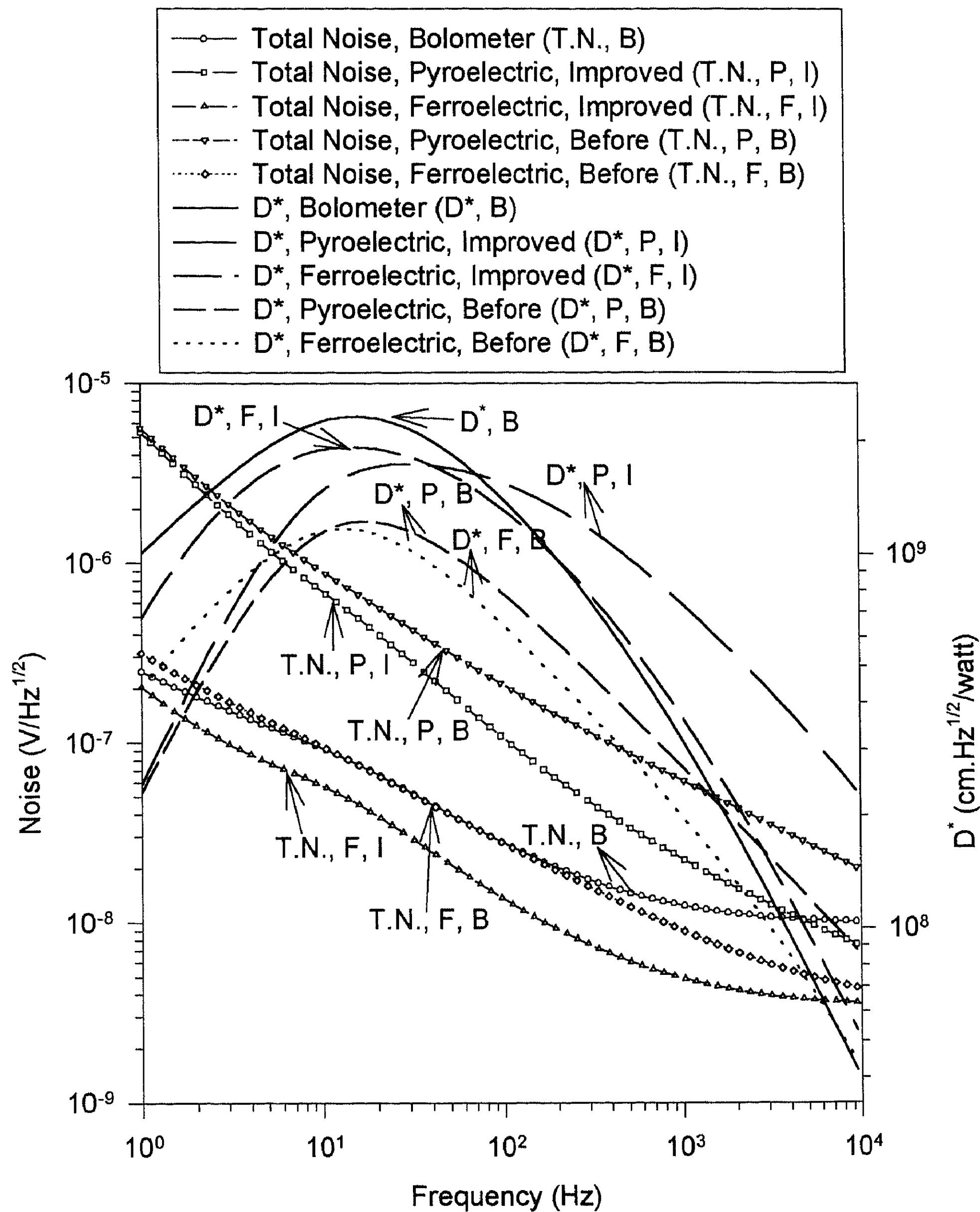

Fig. 6.22 Comparison of the D^* and total noise voltages for bolometer, pyroelectric and ferroelectric detectors. Bolometer detector is based on Fig. 6.5. Pyroelectric and ferroelectric detectors are based on Figs. 6.13 and 6.14. The D^* and total noise voltages of pyroelectric and ferroelectric detectors with improving the material properties are also plotted for comparison.

6.4 Future Directions

- Improving the pyroelectric coefficient may be an effective direction for materials research when the Johnson noise of load resistance is dominant, i.e. when the load resistance is about $10^8\Omega$. This is because the responsivity is linearly proportional to the pyroelectric coefficient, and the Johnson noise is independent of pyroelectric coefficient. The electrical time constant is about 1.2ms for a pyroelectric detector with $R_L = 10^8\Omega$ while the electrical time constant is much greater for a ferroelectric detector with $R_L = 10^8\Omega$. These values are required for 2-D staring arrays which are the needed for transportation, military and contactless temperature measurement applications. Therefore, it is important to analyze potential performance when $R_L = 10^8\Omega$ or smaller.

- When the pixel area is reduced, the NETD and D* decrease because they are proportional to pixel area (input infrared power). The modulation transfer function also improves. This means that means the spatial resolution increases while the array cost decreases for constant performance. Therefore, it may be interesting and important to understand the benefits of future material improvements and/or the requirements on the material properties for resistive, pyroelectric and ferroelectric detectors.

APPENDIX A

TEMPERATURE FLUCTUATION NOISE

The main work of this appendix is to transfer the mean-square energy fluctuation in a system to the equivalent mean-square temperature fluctuation and equivalent mean-square power fluctuation. For infrared sensors, we concern the input infrared power, not the input infrared energy. Therefore, the mean-square energy fluctuation should be transferred to mean-square power fluctuation.

The following derivation for temperature noise is adapted from Refs. 21-23. Maxwell-Boltzmann indicated that the average energy in a closed system in a thermal equilibrium at a given temperature T is

$$\overline{E} = \frac{\sum_i E_i p(E_i)}{\sum_i p(E_i)} = \frac{\sum_i E_i e^{-E_i/k_B T}}{\sum_i e^{-E_i/k_B T}} \tag{A.1}$$

where E_i is the energy of the individual state, and $p(E_i)$ is the Boltzmann probability distribution expressed by

$$p(E_i) = Ae^{-E_i/k_B T} \text{ with } \sum_i Ae^{-E_i/k_B T} = 1 \tag{A.2}$$

Using this definition, the heat capacitance C_{th} is

$$\begin{aligned}\frac{d\overline{E}}{dT} = C_{th} &= \frac{1}{k_B T^2}\left[\frac{\sum_i E_i^2 e^{-E_i/k_B T}}{\sum_i e^{-E_i/k_B T}} - \left(\frac{\sum_i E_i e^{-E_i/k_B T}}{\sum_i e^{-E_i/k_B T}}\right)^2\right] \\ &= \frac{1}{k_B T^2}\left[\overline{E^2} - \overline{E}^2\right] \\ &= \frac{1}{k_B T^2}\overline{\Delta E^2}\end{aligned} \tag{A.3}$$

where $\overline{E^2}$ is the mean-square energy, $\overline{E}^2$ is the square of the mean energy and $\overline{\Delta E^2}$ is the mean-square energy fluctuation. Because $d\overline{E}/dT = C_{th}$, the mean-square energy fluctuation or energy variance, $\overline{\Delta E^2}$, can be expressed by

$$\overline{\Delta E^2} = C_{th}^2 \overline{\Delta T^2} \tag{A.4}$$

where $\overline{\Delta T^2}$ is the mean-square temperature fluctuation due to the energy fluctuations described in Eq. A.3. Substituting Eq. A.3 into Eq. A.4 yields

$$\overline{\Delta T^2} = \frac{k_B T^2}{C_{th}} \tag{A.5}$$

Next consider the spectral content of the fluctuations.

The heat transfer equation is

$$\frac{d(\Delta E)}{dt} = K_{th} \Delta T \tag{A.6}$$

Where $d\Delta E / dT$ is the rate of heat flow and K_{th} is the thermal conductivity. The heat transfer equation can be expressed as

$$\frac{d\Delta E}{dt} = C_{th} \frac{d\Delta T}{dt} \tag{A.7}$$

Using Eqs. A.6 and A.7, one can derive a differential equation describing the heat transfer

$$-C_{th} \frac{d\Delta T}{dt} = K_{th} \Delta T \tag{A.8}$$

The solution of this equation is

$$\Delta T = \Delta T_0 \exp(-t K_{th} / C_{th}) \tag{A.9}$$

If heat flows into the material from an external source, for example a radiating background, the differential equation becomes

$$C_{th}\frac{d\Delta T}{dt}+K_{th}\Delta T=W(t) \tag{A.10}$$

where $W(t)$ is the power fluctuation in time from the external source. $W(t)$ has the form of

$$W(t)=W_f\exp[j2\pi ft] \tag{A.11}$$

Here, the mean square of W_f is assumed to be white noise, independent of frequency, and can be written as

$$\overline{W_f^2}=W_0\Delta f \tag{A.12}$$

where W_0 is a constant. Solving the differential Eq. A.10 yields

$$\Delta T(f)=\Delta T_0\exp(-K_{th}t/C_{th})+\frac{W_f e^{j2\pi ft}}{K_{th}+j\omega C_{th}} \tag{A.13}$$

and therefore

$$\overline{\Delta T(f)^2}=\frac{\overline{W_f^2}}{K_{th}^2+4\pi^2 f^2 C_{th}^2}=\frac{W_0\Delta f}{K_{th}^2+4\pi^2 f^2 C_{th}^2} \tag{A.14}$$

The value $\overline{\Delta T(f)^2}$ represents the frequency dependence of the mean square temperature fluctuations. Integrating it over all frequency will yield the mean square value for temperature fluctuations over all frequencies, assuming K_{th} and C_{th} are frequency independent.

$$\overline{\Delta T^2}=W_0\int_0^\infty\frac{df}{K_{th}^2+4\pi^2 f^2 C_{th}^2}=\frac{W_0}{4K_{th}C_{th}} \tag{A.15}$$

Eqs. A.5 and A.15 yield

$$\frac{k_B T^2}{C_{th}} = \frac{W_0}{4K_{th}C_{th}} \tag{A.16}$$

and

$$W_0 = 4k_B K_{th} T^2 \tag{A.17}$$

Substituting this value into Eq. A.14, we find the expression for the spectrum of the mean square temperature fluctuations.

$$\overline{\Delta T(f)^2} = \frac{4k_B K_{th} T^2 \Delta f}{K_{th}^2 + (2\pi f C_{th})^2} \tag{A.18}$$

The mean square power fluctuations, the quantity $\overline{W(t)^2}$, is determined from Eqs. A.12 and A.17 to be

$$\overline{W(t)^2} = 4k_B K_{th} T^2 \Delta f \tag{A.19}$$

The thermal capacity C_{th} does not enter into the expression for the power fluctuations. This is of fundamental importance since it indicates that the background and temperature noise limited performance of a thermal detector are independent of detector material and volume.

APPENDIX B

NETD FOR TEMPERATURE FLUCTUATION NOISE AND BACKGROUND FLUCTUATION NOISE LIMITED

The noise equivalent temperature difference (*NETD*) for temperature fluctuation noise and background fluctuation noise are derived as follows.

The noise equivalent power (*NEP*) is defined as the signal power needed to achieve a signal-to-noise ratio of one; therefore, according to Eq. A.19

$$\eta NEP = \overline{W(t)^2}^{1/2} = (4k_B K_{th} T^2 \Delta f)^{1/2} \qquad \text{(B.1)}$$

where η is the absorptivity of the detector. Also, since

$$D^*(T,f) = \frac{(A_{pixel}\Delta f)^{1/2}}{NEP} \qquad \text{(B.2)}$$

then D^* for a temperature fluctuation noise limited thermal detector is

$$D^*(T,f) = \left[\frac{\eta^2 A_{pixel}}{4k_B T^2 K_{th}}\right]^{1/2} \qquad \text{(B.3)}$$

Therefore,

$$NETD = \frac{8TF^2(k_B \Delta f K_{th})^{1/2}}{\eta A_{pixel}\tau_0(\Delta P / \Delta T)_{\lambda 1-\lambda 2}} \qquad \text{(B.4)}$$

The derivation of D^* for true background (radiation) limited performance from a thermal detector assumes that the detector satisfies certain conditions. First, the detector is assumed to be in a vacuum and to have no leads coming from it that could promote thermal conductance. These first assumptions simply state that the detector must be

perfectly isolated from the environment. Theoretically, this is a good idea. In reality, however, it would cause problems in extracting information from the detector. A second condition is that the detector absorptivity is independent of wavelength. Finally, the background temperature is assumed to be uniform and fills the entire 2π steradian field of view of the detector.

According to the Stefan-Boltzmann law, the radiation absorbed by the detector is

$$W(T) = A_{pixel}\eta\sigma T_B^4 \tag{B.5}$$

where η is the emissivity of the detector surface, and σ is Stefan-Boltzmann's constant, $5.67*10^{-12} watts/cm^2K^4$. T_D is the temperature of the detector and T_B is the temperature of the background scene. In this case, $T_B = T_D = T$, because the detector is considered to be at room temperature. As the temperature of the background changes, the flux incident on the detector will change in a way described by differentiation of Eq. B.5

$$dW(T) = 4A_{pixel}\eta\sigma T^3 dT \tag{B.6}$$

Since the change in flux with respect to temperature is the thermal conductance, K_{th}, then

$$K_{th} = 4A_{pixel}\eta\sigma T^3 \tag{B.7}$$

Substituting the expression for K_{th} into Eq. A.19 yields

$$\overline{W(t)^2} = 16A_{pixel}k_B\eta\sigma\Delta f T^5 \tag{B.8}$$

And,

$$\eta NEP = \overline{W(t)^2}^{1/2} \tag{B.9}$$

Substituting Eq. B.8 for $\overline{W(t)^2}^{1/2}$ and rearranging, one can see that

$$NEP = (16A_{pixel}k_B\eta\sigma\Delta f T^5)^{1/2}/\eta \tag{B.10}$$

In a less idealized situation where T_D is not necessarily equal to T_B, the NEP expression becomes[27]

$$NEP = [8 A_{pixel} k_B \sigma \Delta f (T_D^5 + T_B^5) / \eta]^{1/2} \tag{B.11}$$

Since

$$D^*(T,f) = \frac{(A_{pixel}\Delta f)^{1/2}}{NEP} \tag{B.12}$$

then D^* for a background-noise limited thermal detector is

$$D^* = [\eta / 8 k_B \sigma (T_D^5 + T_B^5)]^{1/2} \tag{B.13}$$

Therefore the noise equivalent temperature difference is given by

$$NETD = \frac{4F^2}{\tau_0 (\Delta P / \Delta T)_{\lambda 1 - \lambda 2}} \left[\frac{8 k_B \sigma \Delta f (T_D^5 + T_B^5)}{\eta A_{pixel}} \right]^{1/2} \tag{B.14}$$

This is the theoretical minimum $NETD$ when the background radiation noise is the dominant noise.

REFERENCES

1. R. Andrew Wood and Norman A. Foss, "Micromachined Bolometer Arrays Achieve Lost-Cost Imaging", Laser Focus World, pp. 101-106, June 1993.

2. Antoni Rogalski, "New Trends in Infrared Detector Technology", Infrared Phys. Technl. Vol. 35, No. 1, pp. 1-21, 1994.

3. Stephen B. Campana, *Passive Electro-Optical Systems, The Infrared and Electro-Optical Systems Handbook*, Vol. 5, Infrared Information Analysis Center and SPIE, Bellingham, WA, 1993.

4. Louis J. Denes, Richard Grace, etc., "Assessment of Driver Vision Enhancement Technologies", SPIE, Vol. 2592, pp. 17-27, 1995.

5. Wassim G. Najm, "Comparison of Alternative Crash Avoidance Sensor Technologies", SPIE, Vol. 2344, pp. 62-72, 1994.

6. Satoru Fujii, Takeshi Kamada, etc., "Pyroelectric Linear Array Infrared Sensors Made of La-modified $PbTiO_3$ Thin Films and their Applications", SPIE, Vol. 2552, pp. 612-621, 1995.

7. Kuang C. Wei and Gary A. Dage, "An Intelligent Automotive Climate Control System", 1995 IEEE International Conference on Systems, Man and Cybernetics. Intelligent Systems for 21st Century, Vol. 4, pp. 2977-2982, 1995.

8. Günter Hofmann, Volkmar Norkus, etc., "Uncooled Pyroelectric Arrays for Contactless Temperature Measurements", SPIE, Vol. 2474, pp. 98-109, 1995.

9. J. Leconte, R. Barbier, H. Fillon and J. L. Coutures, "Pyroelectric Mid-resolution Camera TH74KB41A", SPIE, Vol. 2552, pp. 865-871, 1995.

10. R. A. Wood, etc., "IR *SnapShot*™ Camera", SPIE, Vol. 2552, pp. 654-660, 1995.

11. Robert J. S. Kyle and Douglas Van Dover, "Uncooled Infrared Thermal Imaging Systems for Law Enforcement", SPIE, Vol. 2497, pp. 98-104, 1995.

12. Henry W. Neal and Robert J. S. Kyle, "Texas Instruments Uncooled Infrared Systems", TI Technical Journal, pp. 11-18, September-October, 1994.

13. Charles M. Hanson, Kevin N. Sweester and Steven N. Frank, "Uncooled Thermal Imaging", TI Technical Journal, pp. 2-10, September-October, 1994.

14. Charles Hanson and Howard Beratan, "Uncooled Pyroelectric Thermal Imaging", ISAF'94. Proceedings of the Ninth IEEE International Symposium on Applications of Ferroelectrics, pp. 657-661, 1994.

15. S. Horn and R. Buser, "Uncooled Sensor Technology", SPIE, Vol. 2020, pp. 304-321, 1993.

16. Robert E. Flannery and James E. Miller, "Status of Uncooled Infrared Images", SPIE, Vol. 1689, pp. 379-395, 1992.

17. M. A. Gallo, D. S. Willits, R. A. Lubke and E. C. Thiede, "Low Cost Uncooled IR Sensor for Battlefield Surveillance", SPIE, Vol. 2020, pp. 351-362, 1993.

18. E. L. Dereniak and D. G. Crowe, *Optical Radiation Detector*, John Wiley & Sons, New York, 1984.

19. Gerald C. Holst, *Electro-Optical Imaging System Performance*, JCD Publishing, Bellingham, WA, 1995.

20. C. D. Motchenbacher, J. A. Connelly, *Low-Noise Electronic System Design*, John Wiley & Sons, New York, 1993.

21. P. L. Marasco and E. L. Dereniak, "Uncooled Infrared Sensor Performance", SPIE, Vol. 2020, pp. 363-378, 1993.

22. R. H. Kingston, *Detection of Optical and Infrared Radiation*, Springer-Verlag, New York, Chapter 7, 1978.

23. P. W. Kruse, L. D. Mcglauchlin and R. B. McQuistan, *Elements of Infrared Technology*, John Wiley and Sons, New York, 1962.

24. Jan Baars and Max Schulz, "Performance Characteristics, Measurement Procedures, and Figures of Merit for Infrared Plane Arrays", SPIE, Vol. 2470, pp. 141-155, 1995.

25. J. M. Lioyd, *Thermal Imaging System*, Plenum Press, New York, Chapter 5, 1975.

26. Michael C. Dudzik, *Electro-Optical Systems Design, Analysis, and Testing, The Infrared and Electro-Optical Systems Handbook*, Vol. 4, Environmental Research Institute of Michigan and SPIE Press, Bellingham, WA, 1993.

27. Richard D. Hudson, *Infrared System Engineering*, John Wiley & Sons, New York, 1969.

28. R. A. Wood, C. J. Han, and P. W. Kruse, "Integrated Uncooled Infrared Detector Imaging Arrays", Proc. IEEE Solid State Sensor and Actuator Workshop, Hilton Head Island, pp. 132-135, 1992.

29. W. L. Wolfe and G. J. Zissis, *The Infrared HandBook*, Office of Naval Research, Washington, DC, Second edition (1985).

30. L. J. Hornbeck, "Infrared Detector", U.S. Patent: 5,021,663, 1991.

31. P. W. Kruse, "SPIE's Short Course Notes on Uncooled IR Focal Plane Arrays", SPIE, 9-14 July, 1995.

32. B. Cole, R. Horning, etc., "High Performance Infrared Detector Arrays Using Thin Film Microstructures", ISAF'94, Proc. of the 9th IEEE Int. Symp. On Application of Ferroelectrics, pp. 653-656,1994.

33. P. W. Kruse, "Uncooled Infrared Focal Plane Arrays", Proc. IEEE Ninth International Symposium on the Applications of Ferroelectrics, August 7-10, 1994.

34. R. A. Wood, "Uncooled Thermal Imaging with Monolithic Silicon Focal Planes", SPIE, Vol. 2020, pp. 322-329, 1993.

35. R. A. Wood, B. E. Cole, etc., "HIDAD-A Monolithic, Silicon, Uncooled Infrared Imaging Focal Plane Array", Proc. GOMAC 1991, pp. 579-581.

36. N. Butler, R. Blackwell, etc., "Low Cost Uncooled Microbolometer Imaging System for Dual Use", SPIE, Vol. 2552, pp. 583-591, 1995.

37. P. W. Kruse, "Uncooled IR Focal Plane Arrays", SPIE, Vol. 2552, pp. 556-563, 1995.

38. P. Umadevi, C. L. Nagendra, etc., "A New Thermistor Material for Thermistor Bolometer: Material Preparation and Characterization", SPIE, Vol. 1485, pp. 195-205, 1991.

39. H. Jerominek, F. Picard and D. Vincent, "Vanadium Oxide Films for Optical Switching and Detection", Optical Engineering, Vol. 32, No. 9, pp. 2092-2099, Sept. 1993.

40. K. C. Liddiard, "Thin-Film Resistance Bolometer IR Detectors", Infrared Phys. Vol. 24, No. 1, pp. 57-64, 1984.

41. K. C. Liddiard, "Thin-Film Resistance Bolometer IR Detectors-II", Infrared Phys. Vol. 26, No. 1, pp. 43-49, 1986.

42. K. C. Liddiard, “Application of Interferometric Enhancement to Self-absorbing Thin Film Thermal IR Detectors”, Infrared Phys. Vol. 34, No. 4, pp. 379-387, 1993.

43. K. C. Liddiard, “Thin Film Monolithic Detectors Arrays for Uncooled Thermal Imaging”, SPIE, Vol. 1969, pp. 206-216, 1993.

44. K. C. Liddiard, M. H. Unewisse and O. Reinhold, “Design and Fabrication of Thin Film Monolithic Uncooled Infrared Detector Arrays”, SPIE, Vol. 2225, pp. 62-71, 1994.

45. M. H. Unewisse, S. J. Passmore, K. C. Liddiard and R. J. Watson, “Performance of Uncooled Semiconductor Film Bolometer Infrared Detectors”, SPIE, Vol. 2269, pp. 43-52, 1994.

46. Christer Jansson, Ulf Ringh and Kevin Liddiard, “On-chip Analog-to-Digital Conversion Suitable for Uncooled Focal Plane Detector Arrays Employed in Smart IR Sensors”, SPIE, Vol. 2474, pp. 72-87, 1995.

47. Ulf Ringh, Christer Jansson, Christer Svensson and Kevin Liddiard, “CMOS Analog to Digital Conversion for Uncooled Bolometer Infrared Detector Arrays”, SPIE, Vol. 2474, pp. 88-97, 1995.

48. C. Jansson , Ulf Ringh, K. Liddiard, ”Theoretical Analysis of Pulse Bias Heating of Resistance Bolometer Infrared Detectors and Effectiveness of Bias Compensation”, SPIE, Vol. 2552, pp. 644-652, 1995.

49. M. H. Unewisse, K. C. Liddiard, etc., “Semiconductor Film Bolometer Technology for Uncooled IR Sensors”, SPIE, Vol. 2552, pp. 77-87, 1995.

50. K. C. Liddiard, Ulf Ringh, C. Jansson, “Starting Focal Plane Arrays for Advanced Ambient Temperature Infrared Sensors”, SPIE, Vol. 2552, pp. 564-572, 1995.

51. M. H. Unewisse, B. J. Craig, etc., “The Growth and Properties of Semiconductor Bolometers for Infrared Detection”, SPIE, Vol. 2554, pp. 43-54, 1995.

52. C. C. H. Hale, J. S. Orr, etc., “Deposition and Characterization of Sputtered Vanadium Dioxide Films”, SPIE, Vol. 1270, pp. 222-236, 1990.

53. William D. Rogatto, *Electro-Optical Components, The Infrared and Electro-Optical Systems Handbook*, Vol. 3, Infrared Information Analysis Center and SPIE, Belingham, WA, 1993.

54. Kulwicki, etc, "Pyroelectric Imaging", Proc. 8th Int. Symp. Appl. Ferroelectrics , 1992.

55. Whatmore, "Pyroelectric Devices and Materials", Rep. Prog. Phys. 49, pp.1335-1386, 1986.

56. Watton, etc., "IR Bolometer Arrays: the Route to Uncooled, Affordable Thermal Imaging", SPIE. Vol. 2020, pp. 379-390, 1993.

57. Watton, "Ferroelectric Materials and Devices in Infrared Detection and Imaging", Ferroelectrics, Vol. 91, pp. 87-108, 1989.

58. D. K. Cheng, *Field and Wave Electromagnetics*, Addison-Wesley, Redwood, CA, 1983.

59. Watton and P. A. Manning, "The Design of Low-Noise Arrays of MOSFETs for Pyroelectric Array Readout, (LAMPAR)", SPIE. Vol. 807, pp. 98-105, 1987.

60. Patel, etc., "Ferroelectric Ceramics and Thin Films for Uncooled Thermal Imaging Arrays", ISAF'94, 9th IEEE Int. Symp. on Applications of Ferroelectrics, pp. 647-652, 1995.

61. Guanghua Yi, Zheng Wu and Michael Sayer, "Preparation of $Pb(Zr,Ti)O_3$ Thin Films by Sol Gel Processing: Electrical, Optical, and Electro-optic Properties", J. Appl. Phys. Vol. 64, Iss. 5 , pp. 2717-2724, 1 Sept. 1988.

62. K. Deb, etc., "Pyroelectric Characteristic of a Thin PZT(40/60) Film on a Platinum Film for Infrared Sensors", Integrated Ferroelectrics, Vol. 6, pp. 253-264, 1995.

63. Watton and M. A. Todd, "Induced Pyroelectricity in Sputtered Lead Scandium Tantalate Films and Their Merit for IR Detector Arrays", Ferroelectrics, Vol. 118, pp. 279-295, 1991.

64. Watton, "Ferroelectric Materials and IR Bolometer Array: From Hybrid Arrays Towards Integration", Integrated Ferroelectrics, Vol. 4, pp. 175-186, 1994.

65. Eiso Yamaka, etc., "Structural, Ferroelectric and Pyroelectric Properties of Highly c-axis Oriented $Pb_{1-X}Cd_XTiO_3$ Thin Film Grown by Radio-Frequency Magnetron Sputtering", J. Vac. Sol. Technol, A, Vol. 6, No. 5, pp. 2921-2928, Sept/Oct. 1988.

66. Kenji Iijima and Ichiro Ueda, "Pyroelectric Properties and Application to Infrared Sensors of $PbTiO_3$, $PbLaTiO_3$ and $PbZrTiO_3$ Ferroelectric Thin Films", Ferroelectrics, Vol. 118, pp. 325-342, 1991.

67. W. Ainger, C. J. Brierley, etc., "Ferroelectric Thin Films by Metal Organic Chemical Vapour Deposition", Mat. Res. Soc. Symp. Proc. Vol. 200, pp. 37-47, 1990.

68. Kulwicki, "Fine-Grain Pyroelectric Detector Material and Method", U.S. Patent: 5,314,651, 1994.

69. Hanson and H. Beratan, "Uncooled Pyroelectric Thermal Imaging", ISAF'94. Proceedings of the Ninth IEEE International Symposium on Applications of Ferroelectrics, pp. 657-661, 1994.

70. Beratan, C. Hanson and E. G. Meissner, "Low-Cost Uncooled Ferroelectric Detector", SPIE, Vol. 2274, pp. 147-156, 1994.

71. Owen, Jeff Belcher, H. Beratan and S. Frank, "Producibility Advances in Hybrid Uncooled Infrared Devices", SPIE., Vol. 2225, pp. 79-86, 1994.

72. Witter, H. Beratan, etc, "Pyroelectric Materials for Uncooled IR Detectors", Texas Instruments Technical Journal, Sept.-Oct., pp. 19-26, 1994.

73. Hanson, etc, "Uncooled Thermal Imaging", Texas Instruments Technical Journal, Sept.-Oct., pp. 2-10, 1994.

74. Belcher and R. A. Owen, "Uncooled Infrared Detector Processing", Texas Instruments Technical Journal, Sept.-Oct., pp. 27-35, 1994.

75. Neal and Robert J.S. Kyle, "Texas Instruments Uncooled Infrared Systems", Texas Instruments Technical Journal, Sept.-Oct., pp. 11-18, 1994.

76. Hanson, "Uncooled Thermal Imaging at Texas Instruments", SPIE, Vol. 2020, pp. 330-339, 1993.

77. Owen, S. Frank and C. Daz, "Producibility of Uncooled IRFPA Detectors", SPIE, Vol. 1683, pp. 74-80, 1992.

78. Hanson, H. Beratan, etc, "Uncooled Thermal Imaging at Texas Instruments", SPIE, Vol. 1735, pp. 17-26, 1992.

79. E. Burgess, P. A. Manning and R. Watton, "The Theoretical and Experimental Performance of a Pyroelectric Array Imager", SPIE. Vol. 572, pp. 2-6, 1985.

80. A. Manning, D. E. Burgess and R. Watton, "A Linear Pyroelectric Array IR Sensor", SPIE. Vol. 590, pp. 2-10, 1985.

81. Watton, "Ferroelectric for Infrared Detection and Imaging", Proc 6th IEEE Int. Symp. Applications of Ferroelectrics, pp. 172-181, 1986.

82. Watton and M. V. Mansi, " Performance of a Thermal Imager Employing a Hybrid Pyroelectric Detector Array with MOSFET Readout", SPIE. Vol. 865, pp. 78-85, 1987.

83. V. Mansi, T. J. Liddicoat and L. J. Richards, " Thermal Imaging with Uncooled Pyroelectric Infrared Detectors", SPIE. Vol. 807, pp. 48-56, 1987.

84. E. Burgess, "Pyroelectrics in a Harsh Enviroment", SPIE. Vol. 930, pp. 139-150, 1988.

85. Watton, "Ferroelectric Materials and Devices in Infrared Detection and Imaging", Ferroelectrics, Vol. 91, pp. 87-108, 1989.

86. Shorrock, etc., "Uncooled Infrared Thermal Detector Arrays", SPIE. Vol. 1320, pp. 88-94, 1990.

87. Watton, M. A. Todd and T. P. Gillham, " Materials and Technology Research in Uncooled Ferroelectric IR Detector Arrays", 4th Int. Conf. On Advanced IR Detectors and Systems, pp. 69-77, 1990.

88. W. Whatmore, etc., "Ferroelectric Materials for Thermal IR Sensors State-of-Art and Perspectives", Ferroelectrics, Vol. 104, pp. 269-283, 1990.

89. W. Shorrocks, etc., "Lead Scandium Tantalate for Thermal Detector Applications", Ferroelectrics, Vol. 106, pp. 387-392, 1990.

90. W. Whatmore, "Pyroelectric Ceramics and Devices for Thermal Infra-Red Detection and Imaging", Ferroelectrics, Vol. 118, pp. 241-259, 1991.

91. Watton, "IR Bolometers and Thermal Imaging: the Role of Ferroelectric Materials", Ferroelectrics, Vol. 133, pp. 5-10, 1992.

92. W. Whatmore, etc., "Ferroelectric Materials for Uncooled Thermal Imaging", SPIE. Vol. 2020, pp. 391-402, 1993.

93. G. Porter, R. Watton and R. K. McEwen, "Ferroelectric Arrays: The Route to Low Cost Uncooled Infrared Imaging", SPIE. Vol. 2552, pp. 573-582, 1995.

94. Putley, "A Method for Evaluating the Performance of Pyroelectric Detectors", Infrared Physics, Vol. 20, pp. 139-147, 1980.

95. L. Polld, Chian-ping Ye, and Takashi Tamagawa, "Surface-micromachined $PbTiO_3$ Pyroelectric Detectors", Applied Physics Letter, Vol. 59, pp. 3539-3541, 1991.

96. Chian-ping Ye, Takashi Tamagawa, and D. L. Polla, "Experimental Studies on Primary and Secondary Pyroelectric Effects in $Pb(Zr_xTi_{1-x})O_3$, $PbTiO_3$, and ZnO Thin Films", J. Appl. Phys. Vol. 70, No. 10, pp. 5538-5543, November, 1991.

97. Ye, T. Tamagawa, P. Schiller and D. L.Polla,"Pyroelectric $PbTiO_3$ Thin Films for Microsensor Applications", Sensors and Actuators A, Vol. 35, pp. 77-83, 1992.

98. Pham, W. Tjhen, C. Ye, and D. L. Polla, "Surface-Micromachined Pyroelectric Infrared Imaging Array with Vertically Integrated Signal Processing Circuitry", IEEE Transactions on Ultrasonics, Ferroelectrics, and Frequency Control, Vol. 41, No. 4, pp. 552-555, July 1994.

99. Polla, etc., "Micromachined Infrared Detectors Based on Pyroelectric Thin Films", SPIE, Vol. 2552, pp. 602-611, 1995.

100. T Elbel, R. Lenggenhager and H. Baltes, "Model of Thermoelectric Radiation Sensors Made by CMOS and Micromachining", Sensors and Actuators A, 35, pp. 101-106, 1992.

101. G. C. M. Meijer and A. W. van Herwaarden, *Thermal Sensors*, Adam Hilger, Bristol, 1994.

102. A. W. van Herwaarden and P. M. Sarro, "Thermal Sensors Based on the Seeback Effect", Sensors and Actuators, Vol. 10, pp. 321-346, 1986.

103. G. R. Lahij and Kensall D. Wise, "A Batch-Fabricated Silicon Thermopile Infrared Detector", IEEE Transactions on Electron Devices, Vol. ED-29, No. 1, pp. 14-22, 1982.

104. Il Hyun Choi and Kensall D. Wise, "A Silicon-Thermopile-Base Infrared Sensing Array for Use in Automated Manufacturing", IEEE Transactions on Electron Devices, Vol. ED-33, No. 1 pp. 72-79, 1986.

105. A. W. van Herwaarden, etc., "Integrated Thermopile Sensors", Sensors and Actuators, A21-A23, pp. 621-630, 1989.

106. S. M. Sze, *Semiconductor Sensors*, John Wiley & Sons, New York, 1994.

107. Rene Lenggenhager, H. Baltes, etc., "Thermoelectric Infrared Sensors by CMOS Technology", IEEE Electron Device Letters, Vol. 13, No. 9, pp. 454-456, Sept. 1992.

108. N. Schneeberger, O. Paul and H. Baltes, "Optimized Structured Absorbers for CMOS Infrared Detectors", The 8th International Conference on Solid-State Sensors and Actuators, and Eurosensors IX, pp. 648-651, 1995.

109. M. Müller, etc., "A Thermoelectric Infrared Radiation Sensor with Monolithically Integrated Amplifier Stage and Temperature Sensor", The 8th International Conference on Solid-State Sensors and Actuators, and Eurosensors IX, pp. 640-643, 1995.

110. M. Müller, etc., "A Fully CMOS-compatible Infrared Sensor Fabricated on SIMOX Substrates", Sensors and Actuators A, 41-42, pp. 538-541, 1994.

111. H. Baltes, " CMOS as Sensor Technology", Sensors and Actuators A, 37-38, pp. 51-56, 1993.

112. F. Völklein and A. Wiegand, "High Sensitivity and Detectivity Radiation Thermopiles Made by Multi-layer Technology", Sensors and Actuators A, 24, pp. 1-4, 1990.

113. J. Schieferdecker, R. Quad, E. Holzenkämpfer, M. Schulze, "Infrared Thermopile Sensors with High Sensitivity and Very Low Temperature Coefficient", Sensors and Actuators A, 46-47, pp. 422-427, 1995.

114. Daniel D. Pollock, *Thermo-couples, Theory and Properties*, CRC Press, Boca Raton, FL, 1991.

115. U. Birkholz, R. Fetting and J. Rosenzweig, "Fast Semiconductor Thermoelectric Devices", Sensors and Actuators, Vol. 12, pp. 179-184, 1987.

116. F. Völkein, A. Wiegand and V. Baier, "High-sensitivity Radiation Thermopiles Made of Bi-Sb-Te Films", Sensors and Actuators A, Vol. 29, pp. 87-91, 1991.

117. Andrew D. Oliver, Wayne G. Baer and Kensall D. Wise, "A Bulk-Micromachined 1024-element Uncooled Infrared Imager", The 8th International Conference on Solid-State Sensors and Actuators, and Eurosensors IX, pp. 636-639, 1995.

118. Wayne G. Baer, etc., "A Multiplexed Silicon Infrared Thermal Imager", 1991 International Conference on Solid-State Sensors and Actuators, pp. 631-634, 1991.

119. R. Lenggenhager, H. Baltes and T. Elbel, "Thermoelectric Infrared Sensors in CMOS Technology", Sensors and Actuators A, 37-38, pp. 210-220, 1993.

120. F. Völkein and H. Baltes, "Thermoelectric Properties of Polysilicon Films Dopant with Phosphorous and Boron", Sensors and Materials, No. 3, pp. 325-334, 1992.

121. E. Obermeier and P. Kopystynski, "Polysilicon as a Material for Microsensor Applications", Sensors and Actuators A, 30, pp. 149-155, 1992.

122. W. Radford, D. Murphy, M. Ray, S. Propst, etc., "320*240 Microbolometer Focal Plane Array for Uncooled Applications", SPIE, Vol. 2685, pp. 80-90, 1996.

123. C. Ye, T. Tamagawa and D. L. Polla, "Experimental Studies on Primary and Secondary Pyroelectric Effects in $Pb_{1-X}Zr_{X}TiO_{3}$, $PbTiO_{3}$ and ZnO Thin Films", Journal of Applied Physics, Vol. 70, pp. 5538-5543, 1991.

124. Pontus Eriksson, Jan Y. Andersson, and Göran Stemme, "Thermal Characterization of Surface-Micromachined Silicon Nitride Membranes for Thermal Infrared Detectors", Journal of Microelectromechanical Systems, Vol. 6, No. 1, March 1997.